UNIVERSITÄT POTSDAM

FERDINAND-BRAUN-INSTITUT

MATHEMATISCH-NATUR-WISSENSCHAFTLICHE FAKULTÄT

LEIBNIZ-INSTITUT FÜR HÖCHSTFREQUENZTECHNIK

Investigations of the Impact of Deeply Implanted Buried Current Apertures on the Electro-Optical Properties of Broad-Area Diode Lasers Emitting in the Near-Infrared

Masterarbeit
im Studiengang Physik

Autor
Christian Goerke

Erstgutachter
Dr. Karl Häusler

Ort, Datum
Potsdam, 20. Mai 2020

Zweitgutachter
Prof. Dr. Markus Gühr

Universität Potsdam

Leibniz
Ferdinand
Braun
Institut

Selbstständigkeitserklärung

Ich versichere, dass ich die von mir vorgelegte Arbeit selbstständig verfasst habe, die verwendeten Quellen, Internet-Quellen und Hilfsmittel vollständig angegeben habe und alle Stellen der Arbeit – einschließlich Tabellen und Abbildungen –, die anderen Werken oder dem Internet im Wortlaut oder dem Sinn nach entnommen sind, in jedem Fall unter Angabe der Quelle als Entlehnung kenntlich gemacht habe. Die Arbeit wurde bisher im Rahmen keiner anderen Prüfung vorgelegt.

Potsdam, den 20. Mai 2020

....

Christian Goerke

Danksagung

An erster Stelle möchte ich mich bei Prof. Dr. G. Tränkle, dem Direktor des Ferdinand-Braun-Instituts, Leibniz-Institut für Höchstfrequenztechnik, sowie Dr. A. Knigge, der Leiterin der optoelektronischen Messtechnikabteilung, bedanken, dass ich meine Masterarbeit am FBH als Teil der Messtechnik-Arbeitsgruppe anfertigen durfte. Mein weiterer Dank gilt Prof. Dr. M. Gühr von der Universität Potsdam, der sich freundlicherweise bereit erklärte die Arbeit zu begutachten.

Besonderer Dank gebührt meinem Betreuer, Dr. Karl Häusler. Du hast mich gelehrt alles zu hinterfragen; dass ein Experiment für eine korrekte Interpretation stets ein zugehöriges physikalisches Modell benötigt, und dass nicht immer alles so ist, wie es auf den ersten Blick scheint. Kurz: Du hast mich gelehrt ein besserer Physiker zu sein. Dafür danke ich Dir!

Diese Arbeit wäre ohne die Mitwirkung zahlreicher Kolleginnen und Kollegen am FBH nicht möglich gewesen. Herrn Dr. H. Wenzel danke ich für die Aufklärung tiefgehender physikalischer Verständnisfragen sowie Dr. D. Martin für Einblicke in die Epitaxie und Prozessierung. Anissa Zeghuzi hat sämtliche Simulationen dieser Arbeit erstellt und mich intensiv bei der Fehlerbehebung und Evaluation der Ergebnisse betreut - großen Dank! Mein Dank gebührt ebenfalls den Messplatzbetreuern Ralf Staske, Christof Henze, Martin Wilkens und Christof Zink für ihre Einweisungen und Kooperation bei messtechnischen Problemen aller Art. Des Weiteren haben diverse Doktoranden und Arbeitskollegen nicht nur gemeinsame Mensagänge bereichert, sondern zu verschiedensten Themen mit hilfreichem Rat und Tat zur Seite gestanden.

Zu guter Letzt möchte ich meiner Familie, meinen Freunden und meiner Partnerin für ihre Entbehrungen und vielfältigen Unterstützungen während dieser Zeit von ganzem Herzen danken.

Deutschsprachige Zusammenfassung

In dieser Masterarbeit werden die elektrooptischen Eigenschaften von gewinnge-führten, breitstreifigen Single-Quantum-Well-Diodenlasern mit tief vergrabenen Stromblenden (engl. *buried current aperture*, BCA) untersucht. Die Technik basiert auf einem zweistufigen Epitaxieprozess. Nach der ersten Epitaxie werden Siliziumio-nen in die p-dotierten Mantelschichten der Laserdiode implantiert. Die Implantation definiert die Stromblende und begrenzt den lateralen Stromfluss in der Nähe des Quantum Wells, wodurch die Stromspreizung reduziert wird. Dies ermöglicht die Abscheidung einer dicken Subkontaktschicht zur Verringerung mechanischer Verspannungen auf die Diode. Es werden vier Designs untersucht: BCA-Dioden mit 700 nm (BCA700) und 2900 nm (BCA2900) dicken Subkontaktschichten, sowie verwandte Referenzdesigns ohne BCA (ref700, ref2900). Alle Messungen werden mit elektrooptischen und thermischen Simulationen verglichen.

Es zeigt sich, dass die Schwellenstromstärke der BCA2900-Dioden im Vergleich zu ihren Referenzen signifikant um 20 % abnimmt, wodurch diese auf dem Niveau der Schwellenströme beider 700 nm-Designs liegt. Dies ist auf eine von der Simulation berechneten Abschwächung der Spreizstromstärke I_{spr} um 74 % zurückzuführen. Obwohl für BCA700 I_{spr} ebenfalls um 37 % reduziert wird, ist kein Schwellen-rückgang wie bei BCA2900 zu messen. Des Weiteren ist kein Zusammenhang zwischen verminderter Stromspreizung und dem Serienwiderstand des Bauteils zu finden. Darüber hinaus sind im Rahmen der Messgenauigkeit keine signifikanten Verbesserungen der elektrooptischen Parameter Steilheit, Maximalleistung und Serienwiderstand bis 12 A durch die BCA-Implantation festzustellen.

Alle vermessenen Nahfeldverteilungen weiten sich prinzipiell mit zunehmendem Strom, aber verengen sich im Bereich von 5-10 A. Dies wird durch die Bildung eines thermischen Wellenleiters bei der designspezifischen, kritischen Stromstärke I_{crit} in-duziert, der in Longitudinalrichtung etwa doppelt so stark ist wie in Lateralrichtung. Mit Ausnahme von ref2900 pendeln sich alle Nahfelder bei $I \geq 10\,\mathrm{A}$ auf eine Weite von 82 µm ein, was 18 % niedriger ist als die angestrebte Nahfeldweite von 100 µm für die Einkopplung in optische Fasern. Mit steigender Stromstärke sammeln sich in allen Designs zunehmend Ladungsträger an den Rändern der aktiven Zone an (engl. *lateral carrier accumulation*, LCA). Diese Ansammlungen bewirken einen lokalen Abfall des Brechungsindexes und erzeugen einen Wellenleiter, der dem thermischen Wellenleiter entgegenwirkt. Gleichzeitig verstärken Ladungsträger-ansammlungen in den Randgebieten höhere TE-Moden. Bei den Nahfeldern ist dies in Form wachsender Randintensitäten erkennbar, was zu der beobachteten Stabilisierung der Nahfeldweiten führt. Für Fernfelder sind die Ansammlungen hingegen der Hauptgrund für die gemessene Verbreiterung bei hohen Strömen. LCA

ist wesentlich ausgeprägter bei 2900 nm- als bei 700 nm-Designs, und in geringem Maß mehr bei BCA- als bei Referenzdioden. Zwischen allen Designs existiert kein signifikanter Unterschied in der Strahlqualität, obwohl ref700-Dioden zu einer geringeren Qualitätsabnahme pro Stromstärke und pro Temperaturanstieg der aktiven Zone *tendieren*.

Generell streuen die Strahlkaustikmesswerte von 2900 nm und ref700-Designs weniger stark als die von 700 nm bzw. BCA700; was im Experiment ebenso für die Temperaturen der aktiven Zone von 2900 nm-Strukturen im Vergleich zu 700 nm gilt. Dies impliziert eine Instabilität der 700 nm- und BCA-Diodendesigns, die sich z.B. in einer Anfälligkeit für zufällige Variationen der Herstellungsparameter während der Zweischrittepitaxie äußert. Dennoch kann der Einsatz einer 2900 nm dicken Subkontaktschicht der Wertestreuung relativ gut entgegenwirken. Außerdem reduziert diese die Gesamtmenge gemessener TM-Strahlung um etwa 50 %, die durch den *zusätzlichen* Einsatz einer Stromblende noch weiter abnimmt. Jedoch ist kein nennenswerter Einfluss von *lokalen* Verspannungen festzustellen, obwohl die Stromblende sowohl TE- als auch TM-polarisierte Nahfelder homogenisiert.

Zuletzt konnten diverse Messungen aus Platzgründen nicht in die Arbeit aufgenommen werden, sodass deren Ergebnisse im Folgenden kurz skizziert werden. Erstens hat eine erhöhte Wärmesenkentemperatur von 50 °C einen unsignifikanten, weniger negativen Einfluss auf die PUI-Parameter von BCA-Designs als auf die der Referenzen. Weiterhin liegen für die Wärmesenkentemperaturen 25 °C und 50 °C die meisten Parameterwerte (R_s, w_{NF}, Θ, BPP_{lat}) näher beieinander für 2900 nm- als für 700 nm-Dioden. Dies bestätigt den Eindruck einer höheren Temperaturstabilität von 2900 nm-Strukturen. Zwei exemplarische PUI-Messungen je einer mechanisch montierten ref700- und ref2900-Diode im QCW-Betrieb (2 % Tastverhältnis) führen zu einer katastrophalen Facettenschädigung (engl. *catastrophic optical mirror damage*, COMD) der ref700-Diode bei 16.5 A; während die ref2900-Diode sogar bei 20 A überlebte, was auf höhere COMD-Grenzwerte aufgrund der dickeren Subkontaktschicht hindeutet. Beschleunigte Stufenalterungstests (engl. *step-stress test*, +1 A pro Woche) von 700 nm-Dioden zeigen, dass drei von drei sauerstoffimplantierten BCA-Proben bis zu 15 % (770 h) früher ausfallen als eine einzelne Referenzprobe (910 h). Identische Tests der Si-implantierten Dioden dieser Arbeit bestätigen diese Ergebnisse. Hier degradiert die beste von drei BCA700-Dioden noch immer 11 % früher als ein einzelnes ref700-Exemplar (1060 h, 10 A), das sogar die am längsten überlebende Diode dieser Arbeit darstellt; während die beste BCA2900-Diode das Ende ihrer Lebensdauer nur 2 % früher erreicht als die beste ref2900-Diode (1010 h, 9-10 A). Tatsächlich fallen die meisten 700 nm-Designs vor den 2900 nm-Strukturen aus. Kathodolumineszenzuntersuchungen ergaben katastrophale Facettenschädigungen als Grund für sämtliche Ausfälle.

Contents

1. Aim and Motivation of the Thesis

According to current forecasts, the global market for laser material processing will grow by an average of 9.7 % annually from US\$ 3.36 billion in 2017 to US\$ 5.88 billion in 2023 [1]. With US\$ 760 million in 2015, fiber lasers have a large share in this. In fact, they continuously displace Nd:Yag solid-state lasers, which are pumped at 808 nm and CO_2 gas lasers [2]. This is due to their superior beam quality at lower costs [4]. Primarily, fiber lasers are employed in high-performance material processing like metal sheet cutting and laser marking [5, 6] or in telecommunications [7]. The fibers are frequently doped with rare-earths such as ytterbium [8–10], because Yb^{3+} possesses a wide absorption band in the near-infrared ~700-1400 nm [11], e.g. around 910 nm in germanium-doped silicate glass (SiO_2:Ge) [12]. Mostly, conversion-efficient diode lasers of up to $\eta_c > 65\,\%$ at 10 W [3] are used a pump sources [13–15]. This demands high optical output powers P_{opt} as well as small lateral beam parameter products BPP_{lat} for an efficient fiber-coupling with low optical losses. The broad-area lasers investigated in this thesis are designed to fulfill these requirements.

Modern diode lasers are grown on a n-type substrate via molecular organic vapor phase epitaxy (MOVPE), using an extreme double-asymmetric large optical cavity (EDASLOC) p-i-n-double-heterostructure design. Usually, a few nanometer thick quantum well (QW) serves as optical resonator, extending over several millimeters in longitudinal direction and some hundred micrometers in lateral direction. It is sandwiched between waveguiding and cladding layers to guide the light by total internal reflection. The fabricated laser chip is then mounted p-side down on a CuW submount, soldered onto a conduction-cooled package (CCP), installed on Cu heat sinks for heat disposal and biased in forward direction. Laser operation starts, once the laser modes are provided with their threshold gain g_{th}, where the gain follows the injected current's path. By choosing the width of the diode's p-metal contact $w_{p\text{-contact}}$, the current's width and thereby gain profile can be tailored. The wider the p-contact width, the wider the electrically pumped region – the *active zone*. However, due to the layers' finite electrical conductivity, the current spreads transversely as the carriers diffuse on their way to the quantum well. Since p-doped semiconductors conduct about three times worse than n-doped ones [16], the current spreads significantly more in p-doped layers than in n-doped. Until

now, it could only be mitigated by reducing the p-doped layers' thickness as done with the EDASLOC design. The problem with spreading current is, that carrier densities N in the lateral outer-regions mostly do not reach the threshold condition $N = N_{th}$. Instead, these carriers recombine non-radiatively and heat up the laser, which degrades the internal efficiency η_{int}, laser threshold I_{th} and optical output power $P_{opt}(I)$ [17–20]. Yet, some lateral outer-regions may still reach threshold, amplify higher-order TE modes and degrade BPP_{lat}.

In this Master's thesis, a novel approach to reduce lateral current spreading will be presented and investigated. Employing a two-step epitaxy, diodes are implemented with buried current apertures (BCA) in the lateral outer-regions by the deep implantation of Si^+ ions into the p-cladding layer. This increases the electrical resistance of implanted regions, which reduces the vertical cross-section of current flow area A. By its placement close above the quantum well and width of $w_{BCA} = 100\,\mu m$, the BCA decouples the electrically pumped area from the p-contact area. This enables the compensation of the device's rise in series resistance $R_s \sim 1/A$ by widening the p-contact to $w_{p\text{-contact}}^{BCA} = 400\,\mu m$. At the same time, this restricts the evaluation of the "pure BCA" functionality to a comparison of different laser designs. The reason for that are the conventional "reference" diodes without buried current apertures, which are used for the comparison. To reach the project's target near-field width of $100\,\mu m$ for fiber-coupling, these require $w_{p\text{-contact}}^{ref} = 100\,\mu m$ wide p-contacts. Additionally, two further designs with a thick sub-contact layer (below the p-contact) are studied, i.e. $700\,nm$ vs. $2900\,nm$. The increase in thickness aims to reduce stress-induced strain on the quantum well, which otherwise lowers the diode's performance, beam quality, reliability and lifetime. Next, the electro-optical properties of these four laser designs will be derived and analyzed from measurements at a heat sink temperature of $T_{HS} = 25\,°C$. The results will be compared with each other, as well as evaluated with simulations of the laser's optical, carrier and thermal dynamics via the software tool *BALaser*. Experimental outcomes of preceding or similar investigations have been published by Martin et al. in [19] (with the author's participation) and by della Casa et al. in [21, 22].

Thesis Outline

First, chapter 2 will outline the physical basics of broad-area diode lasers. This will be followed up by an extensive presentation of the diode design in chapter 3, in particular the EDASLOC structure, the BCA implantation procedure and a short qualitative roundup of the expected effects of the BCA on the current profile and electro-optical properties. Chapter 4 sketches the dynamic optical, carrier and thermal models employed in the simulation. Setups for the measurement of the

power-voltage-current (PUI), spectral, polarization and beam caustic characteristics are shown in chapter 5. This chapter also presents the physical background necessary for the derivation of characteristic parameters such as laser threshold I_{th}, temperature of the active zone T_{az} or lateral beam parameter product BPP_{lat}. All measurement results will be analyzed and discussed in context of the simulations in chapter 6, which is divided into three sections: PUI characteristics, beam caustics and polarization-dependent effects. Finally, the thesis will be summarized in chapter 7 and a short outlook on future investigations will be given.

2. High-Power Edge-Emitting Broad-Area Diode Laser Basics

This chapter provides the physical background to semiconductors and high-power broad-area diode lasers, mainly following the semiconductor chapter in [23, pp. 481–525] and the introduction in [24, pp. 1–20]. It assumes basic knowledge of laser physics, which can be read in standard literature [25–29].

2.1. Photoemission in Semiconductors

The energetic structure of semiconductors is made up of energy bands, which result from the solution of the Schrödinger equation for a single electron in the positive periodic potential of the surrounding atom cores. In the upper conduction band, electrons are delocalized and move freely with the effective mass m_e^*, having an edge energy of

$$E_c(k) = E_g + \frac{\hbar^2 k^2}{2m_e^*}.$$
(2.1)

In the lower valence band, valence electrons are bound until they are excited to the conduction band, e.g. via electrical pumping. Thereby, a promoted electron leaves behind a positively charged quasi-particle – the defect-electron or *hole*. Then, a valence electron in the vicinity of the new hole jumps to its site and occupies the energetic state, leaving another hole. The continuation of this process leads to a constant flow of moving holes. These possess the *electron* edge energy

$$E_v(k) = -\frac{\hbar^2 k^2}{2m_h^*},$$
(2.2)

where m_h^* denotes the effective hole mass, $\hbar$ the reduced Plank constant and k the particle's wave vector (momentum $p = \hbar k$). The concept of effective masses,
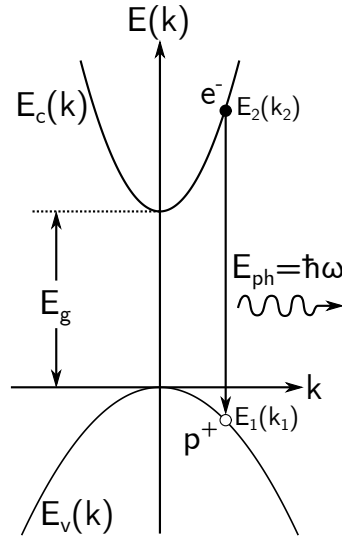
Figure 2.1.: Band structure $E(k)$ for electrons e⁻ and holes p⁺ in a direct semiconductor. The valence band with energy $E_v(k)$ and conduction band with energy $E_c(k)$ are separated by the bandgap E_g. A radiative transition induces the emission of a photon with energy $E_{ph} = \bar{\omega}$.

which replace the free-electron rest mass, is subject to the *nearly-free carrier approximation*. It considers the interaction of carriers with the crystal lattice's atoms. The energy bands are separated by the quantum-mechanically forbidden bandgap E_g, which ranges typically between 0.5 eV and 2.5 eV. In semiconductors, electrons and holes contribute equally to the conduction properties. The probability for an electron (fermion) to occupy a certain energy state E at temperature T in thermal equilibrium is given by the Fermi function

$$f(E,T) = \frac{1}{\exp\left(\frac{E-E_F}{k_B T}\right) + 1},\qquad(2.3)$$

where E_F is the Fermi energy and k_B the Boltzmann constant. At absolute temperature $T = 0\,\text{K}$, the valence band of an undoped (intrinsic) semiconductor is filled completely with bound electrons, while the conduction band remains empty. As such, all electronic states in the valence (conduction) band are occupied $f(E_v,T = 0\,\text{K}) = 1$ (unoccupied $f(E_c,T = 0\,\text{K}) = 0$) and the semiconductor becomes an insulator. Under this condition, E_F lies in the middle of the bandgap and represents the energy level with 50 % occupation probability. With growing temperature, more and more electrons are thermally ionized and the semiconductor becomes conducting, again.

The energy bands described via eqs. (2.1) and (2.2) have a parabolic $E(k)$ dependency, which can be seen in fig. 2.1. If the wave vectors of the conduction band minimum $\vec{k_2}$ and valence band maximum $\vec{k_1}$ coincide (at the Γ-point), then the semiconductor belongs to the direct types at $k_1 = k_2$ (e.g. GaAs) – otherwise to the indirect types $k_1 \neq k_2$ (e.g. Si or Ge) [23, p. 483]. A radiative recombination of an electron-hole pair (at the same k) leads to the spontaneous emission of a photon with energy $E_{\mathrm{ph}} = \hbar\omega$. For indirect semiconductors, this is only possible if further particles like phonons or traps ensure the conservation of momentum. Because such transitions are inefficient and less likely, indirect semiconductors are unsuited for laser operation – at least for serving as active material. In thermal equilibrium, particles minimize their energy, such that electrons occupy states at the lower conduction band edge and holes at the upper valence band edge. Upon incidence of a photon with energy $E_{\mathrm{ph}} = E_g$, a recombination of an electron-hole pair with successive emission of a photon can be stimulated. The emitted photon has the same direction and phase as the incident one, which is known as stimulated emission. It amplifies optical radiation, which forms the basis of laser physics.

Diode lasers make use of a forward-biased double-heterojunction p-i-n design, where an intrinsic (undoped) semiconductor i is sandwiched between n-doped and p-doped ones, which will be explained in more detail in the following two sections. Doping is the implantation of impurities into intrinsic semiconductors (e.g. GaAs) in order to increase their carrier density and thereby conductivity. When the implanted atom (impurity) donates one additional valence electron per atom than necessary for the tetrahedral bond, the semiconductor becomes *n-doped* and the impurity is termed *donator* (e.g. Si) – when it adds one additional hole, one speaks of p-doping and *acceptor* (e.g. C, Zn). The n-doping introduces a new donator energy level E_D close below the conduction band E_c, while the p-doping introduces an acceptor level E_A close above the valence band E_v. The new energy levels are usually separated from E_c and E_v by about $25\,\mathrm{meV}$ [23, pp. 500 sq.], respectively. As such, the new carriers can be thermally ionized at room temperature T~$300\,\mathrm{K}$, providing extra carriers for the conduction. If differently doped semiconductors from different materials are brought together, they form a heterojunction, which is no longer in thermal equilibrium when being forward-biased with voltage U. Electrons and holes are injected into the neutral carrier depletion region, which builds as a consequence of drift and diffusion processes (cf. section 4.2). The coexistence of both carrier types in this region makes it impossible to describe the carrier distribution with only one Fermi function $f(E,T)$. For the nonequilibrium, eq. (2.3) separates into one quasi-Fermi function for the electrons in the conduction band $f(E_1,T) \to f_c(E_1,T)$ with $E_F \to E_{F_c}$ and one for the holes in the valence band $f(E_2,T) \to f_v(E_2,T)$ with $E_F \to E_{F_v}$. Their difference is controlled by the applied voltage $eU = E_{F_c} - E_{F_v}$. Finally, if the rates of stimulated absorption R_{12} and stimulated emission R_{21} (see
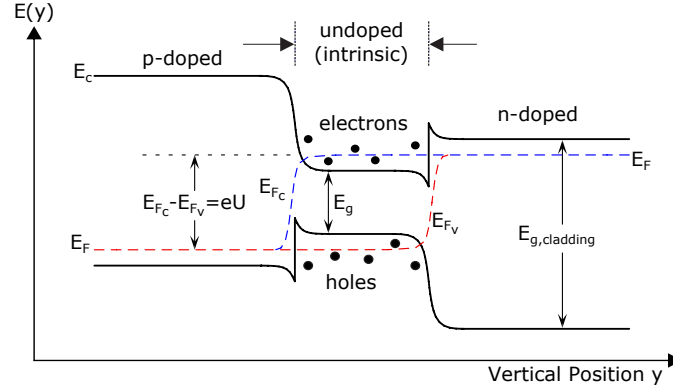
Figure 2.2.: Vertical band structure in a forward-biased p-i-n double-heterojunction diode. In the intrinsic region, the Fermi energy E_F splits to two quasi-Fermi energies for the electrons E_{F_c} and holes E_{F_v}. Here, charge carriers are trapped for efficient radiative recombination due to the higher bandgaps of the surrounding waveguide and cladding materials $E_{\text{g,cladding}}$. Inversion and thereby laser operation is achieved, once the pumped electrical energy eU exceeds the bandgap energy E_g. Then, the quasi-Fermi energies for electrons and holes lie inside their respective energy bands. Adapted from [24, p. 7].

[24, p. 4]) are divided by each other

$$\frac{R_{12}}{R_{21}} = \exp\left[\frac{E_{\text{ph}} - (E_{F_c} - E_{F_v})}{k_B T}\right], \tag{2.4}$$

and when $R_{21} > R_{12}$, the condition for the amplification of an optical wave in a forward-biased heterojunction is revealed:

$$eU = E_{F_c} - E_{F_v} > E_{\text{ph}} > E_g. \tag{2.5}$$

This condition is called population inversion. It is essential for the operation of a (diode) laser and is fulfilled once the (diode) laser is supplied with enough (electrical) energy $eU > E_{\text{ph}}$ to reach transparency and finally threshold.

2.2. Diode Laser Fundamentals and Confinement

For an efficient laser operation, high-power diode lasers employ (vertical) p-i-n double-heterojunction designs. The intrinsic bulk semiconductor (i) with bandgap $E_{\mathrm{g,az}}$ and refractive index n_{az} serves as active medium for the generation of laser light. In conventional double-heterojunction designs, it is surrounded by a p- and a n-doped waveguide layer with bandgap $E_{\mathrm{g,wg}} > E_{\mathrm{g,az}}$ and refractive index $n_{\mathrm{wg}} < n_{\mathrm{az}}$. The higher bandgaps $E_{\mathrm{g,wg}}$ confine the electrons and holes in the active medium, once the diode laser is forward-biased (*carrier confinement*); while the lower refractive indices n_{az} confine the optical mode in the dielectric waveguide via total internal reflection (*optical confinement*). The rear and front facets (transverse (x,z)-plane) of diode lasers are cleaved. They exhibit a natural sharp index contrast to air, resulting in reflection coefficients of about $R \approx 30\,\%$ [24, p. 13]. In this way, a Fabry-Pérot resonator of length L with round-trip length $2L$ is formed. It provides positive feedback for standing waves with vacuum wavelength λ_0 and longitudinal mode number $m = 1,2,3,...$ (# nodes):

$$2L \cdot n_{\mathrm{eff}} = m \cdot \lambda_0. \tag{2.6}$$

Here, n_{eff} denotes the effective refractive index $n_{\mathrm{wg}} < n_{\mathrm{eff}} < n_{\mathrm{az}}$, which is experienced by the propagating optical mode (cf. chapter 4). The actual number of oscillating longitudinal modes depends on n_{eff} and the maximum of the spectral gain (cf. fig. 3.1). When the laser reaches threshold, stimulated emission amplifies the light's intensity J_0 along the optical axis z of the active medium. This is characterized by Beer-Lambert's Law:

$$J(z) = J_0\, e^{\alpha z}, \tag{2.7}$$

where the absorption coefficient α must be replaced by the optical gain $g = -\alpha$. However, depending on the active medium's thickness d and carrier density N, only parts of the modes' vertical intensity distributions overlap with the active zone (especially in quantum wells, cf. section 3.1). Consequently, the gain is lowered by a factor Γ, which is called the (vertical) confinement factor (typ. Γ~10-70 % for d~50-300 nm and Γ<1 % in quantum wells for d<10 nm). Taken together, they form the modal gain:

$$g_m = \Gamma g \tag{2.8}$$

with

$$\Gamma = \frac{\int_{-d/2}^{d/2} J(y) dy}{\int_{-\infty}^{\infty} J(y) dy}. \tag{2.9}$$

Remaining parts of the intensity distribution other than in the active medium are (partially) reabsorbed by scattering at crystal defects or rough interfaces and by absorption from free carriers (FCA) in the other layers (cf. section 3.1) [24, p. 12]. Due to today's state-of-the-art crystal quality, scattering is usually negligible; whereas FCA is unavoidable. This is expressed by the internal (modal) absorption coefficient α_{int}, which adds up with the modal gain to the (total) absorption coefficient:

$$\alpha = \alpha_{\text{int}} - g_m. \tag{2.10}$$

Examples for internal losses α_{int} are photon-phonon scattering and absorption of photons by free charge carriers outside the active zone. A portion of the generated light exits the laser at the front facet with reflectivity R_f, while the rest is reflected at the rear facet R_r and amplified, again. After a full round-trip, the mode's intensity J_{rt} becomes

$$J_{\text{rt}} = J_0 \, R_f \, R_r \, \exp\left[2\left(\Gamma g - \alpha_{\text{int}}\right) L\right]. \tag{2.11}$$

At threshold, J_{rt} equals J_0 after a full round-trip and $g \to g_{\text{th}}$. Inserting this condition into eq. (2.11) reveals the threshold gain g_{th}

$$\Gamma g_{\text{th}} = \alpha_{\text{int}} + \frac{1}{2L} \ln\left(\frac{1}{R_f R_r}\right) \tag{2.12}$$

$$= \alpha_{\text{int}} + \alpha_{\text{mir}} \tag{2.13}$$

with the second summand being identified as the mirror output-losses α_{mir}. Optical modes are amplified when $g_m > \alpha_{\text{int}}$, but lasing starts only when the modal gain $g_{\text{m,th}} = \Gamma g_{\text{th}}$ compensates (equals) the modal internal losses α_{int} *and* the mirror losses α_{int} [24, p. 12].

Up to now, only vertical confinement techniques have been discussed. In order to also achieve a reasonable good beam quality in the lateral dimension x, an appropriate lateral confinement method is required. The lasers investigated in this
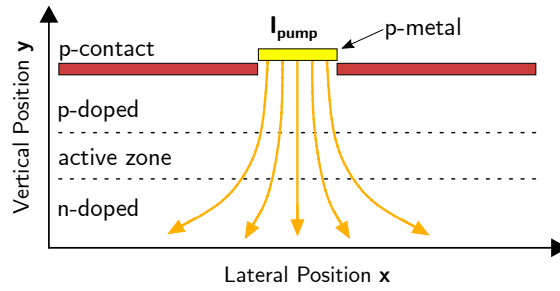
Figure 2.3.: Lateral current confinement in a p-i-n double-heterojunction laser through gain-guiding. The lateral intensity distribution depends on the current profile providing gain to optical modes. The pump current profile I_{pump} shows the technical direction of current flow. The "actual" current consists of a hole current and an electron current, which are injected from both sides into the active zone, as will be explained in chapter 4. Adapted from [24, p. 16].

thesis belong to the class of edge-emitting broad-area diode lasers, which rely solely on *current confinement* in the lateral direction – the so-called gain-guiding.[1] It is mostly realized by usage of a dielectric current aperture as portrayed in fig. 2.3; or by a shallow isolation implantation [24, p. 15], e.g. with He^+ ions. The investigated lasers possess both techniques. Gain-guiding bases on the gain following the pump current profile (cf. eq. (4.7)). Therefore, only those optical modes are amplified, that are supplied with sufficient gain; whereas non-current-carrying regions absorb most of the optical intensity. Other forms of lateral confinement are the (optical) index guiding, e.g. via implementation of trenches with different refractive indices for waveguiding; or the buried heterostructure laser, which incorporates all types of confinement (current, carrier, optical). What's new in this thesis, is the implantation of an additional buried current aperture (BCA), which provides a more precise current confinement than conventional methods. Its implantation and *expected* impact on the electro-optical properties will be discussed in sections 3.2 and 3.3.

---

[1]Other confinement methods like index guiding base on the implementation of (lateral) structures into the diode, e.g. index trenches. These structures create a step in the effective index n_{eff}, which confines the mode in a lateral optical waveguide.

3. Diode Design

3.1. Extreme Double-Asymmetric Large Optical Cavity (EDASLOC) - Structure

Opposed to conventional p-i-n double-heterojunction designs with intrinsic bulk semiconductors, modern high-power diode lasers feature extreme double-asymmetric (EDAS) large optical cavity (LOC) separate-confinement heterostructures (SCH) with a single quantum well (SQW) or multiple quantum wells as active zone(s). Quantum wells (QW) are mostly thinner than 10 nm [24, p. 18], which discretizes the density of states $D(E)$ at the band-edge energies E. In bulk semiconductors, i.e. in active media thicker than $d > 100$ nm [26, p. 11], the density of electronic states rises with $D_c(E) \sim \sqrt{E - E_c}$; while growing in steps at the electronic energy levels of quantum wells (visualized in [25, p. 20]). This ultimately leads to higher max. carrier densities as well as smaller energetic widths of the carrier distribution. Furthermore, the QW's small volume reduces the threshold current I_{th}, increases the (material) gain g and reduces the blue-shift of the gain curve's maximum with carrier density N due to a weakening of the band-filling effect (lower conduction band energy states are occupied, first, such that following transitions require higher photon energies). What is most important: quantum wells allow to be grown with compressive or tensile strain, which will be explained, shortly.

Figure 3.1 compares the gain spectra of a GaAs bulk and a strained InGaAs quantum well for different carrier densities N. As can be seen in fig. 3.1b, the gain maxima at 990 nm shift barely noticeably with rising N. Moreover, at $N \geq 5 \cdot 10^{18}$ cm^{-3}, transitions to the QW's second sub-band create new gain absorption maxima around 915 nm, which corresponds to the target wavelength of the fabricated laser diodes in this thesis.

The term *separate* stems from the separate *primary* confinements of the carriers in the QW, and of the optical modes with an extra bulk waveguiding layer around the QW [26, p. 12]. By that, the former p- and n-doped waveguide layers are sandwiched between cladding layers, which have smaller refractive indices n_{cl} than the waveguides $n_{\mathrm{cl}} < n_{\mathrm{wg}}$ in order to guarantee waveguiding via total internal reflection.

(a) Intrinsic GaAs bulk. The material becomes transparent for $E_{ph} < 1.42\,\mathrm{eV}$.

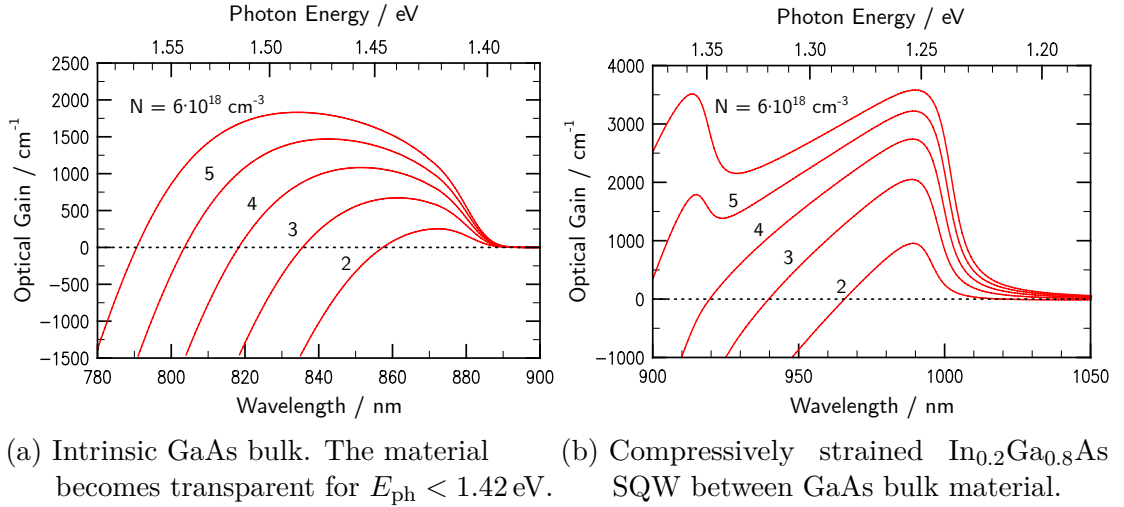(b) Compressively strained $In_{0.2}Ga_{0.8}As$ SQW between GaAs bulk material.

Figure 3.1.: Material-gain spectra at carrier densities $N=2 \cdot 10^{18}$-$6 \cdot 10^{18}\,\mathrm{cm}^{-3}$. A compressive strain weakens the band-filling effect, leading to nearly no spectral shift of the gain maxima with carrier density as opposed to the bulk material. At $N \geq 5 \cdot 10^{18}\,\mathrm{cm}^{-3}$, transitions to the QW's second sub-band increase the gain around $915\,\mathrm{nm}$. Adapted from [24, pp. 11, 18].
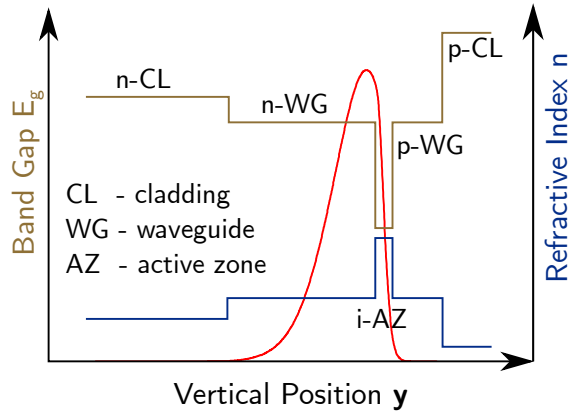
Figure 3.2.: Vertical structure of a modern broad-area diode laser with extreme double-asymmetric (EDAS) double-heterojunction design. The intrinsic quantum well serves as active medium and is sandwiched between waveguides and claddings. The p-doped layers are much narrower than the n-doped ones to reduce the series resistance and optical losses. This also leads to a shift of the fundamental Gaussian mode as sketched in red (taken from [30]).

They also possess higher bandgaps $E_{g,cl} > E_{g,wg}$ to efficiently guide the carriers and confine them in the inserted quantum well with $E_{g,QW} < E_{g,wg}$. Figure 3.2 depicts the refractive index and band gap profiles of diodes with EDASLOC-SCH-SQW design and a sketch of the resulting fundamental Gaussian mode. The much smaller QW reduces the vertical confinement factor Γ, tremendously. It is further decreased by the shift of the fundamental Gaussian mode to the n-doped waveguide due to the asymmetry of the EDASLOC design (here: $\Gamma = 6.6 \cdot 10^{-3}$). In turn, this increases free-carrier absorption in the n-waveguide, being nevertheless preferable to the higher losses in the p-doped layers, as outlined in the following.

In EDASLOC-structures, the active zone is not symmetrically centered, but shifted towards the p-doped cladding and waveguide layers. The asymmetry is motivated by the approx. three times lower conductivity of holes σ_p in p-doped materials than of electrons σ_n in n-doped materials [16, 31] (e.g. GaAs) due to their different effective masses $m_h^* > m_e^*$. This enlarges the electrical resistance $1/\sigma \propto R_p > R_n$ of p-doped regions, which generates more heat ΔT with current (cf. eq. (5.23)), raises thresholds (cf. eq. (5.11)), limits output power (cf. eq. (5.1)) and decreases quantum efficiency (cf. eq. (5.12)). An efficient way to dissipate the generated heat is to keep the p-region as thin as possible and to solder the p-side of the laser chip facing down on the CuW submount (*p-down* mounting). To counter the intrinsic lower conductivity, p-regions are usually doped very high. At the same time, this increases the hole density of states and thereby the optical absorption at free carriers (FCA) [18, 32, 33]. Consequently, a thin p-layer also reduces the internal absorption α_{int} due to the reduction of FCA losses.

Moreover, the light-emitting quantum wells of high-power diode lasers are usually strained, as otherwise a large range of emission wavelengths wouldn't be accessible. III-V semiconductors like GaAs are strained, e.g. by inserting indium, so that the strained quantum well composites to $In_xGa_{1-x}As$ with an accessible wavelength range of approx. 870-1100 nm [24, p. 19]. It's important to note, that the strain is introduced due to lattice mismatching of the QW to the surrounding material. A higher lattice constant than the GaAs substrate generates compressive and a lower lattice constant tensile strain on the QW [26, pp. 18 sq., 218]. The proportion of composition x controls the lattice constant and hence the type of strain as well as the size of the bandgap E_g: with compressively strained quantum wells, the hh-band remains the highest-energy valence band, as shown in fig. 3.3a. It eliminates the degeneration with the *light hole* band in the unstrained state at the Γ-point. Now, it represents the valence band with the most favorable energy for holes [24, pp. 107 sq.]. As a consequence, the valence and conduction band's quasi-Fermi levels shift to lower energies compared with the unstrained state - they approach the energy edges of their respective carrier types, as portrayed in fig. 3.3b [26,
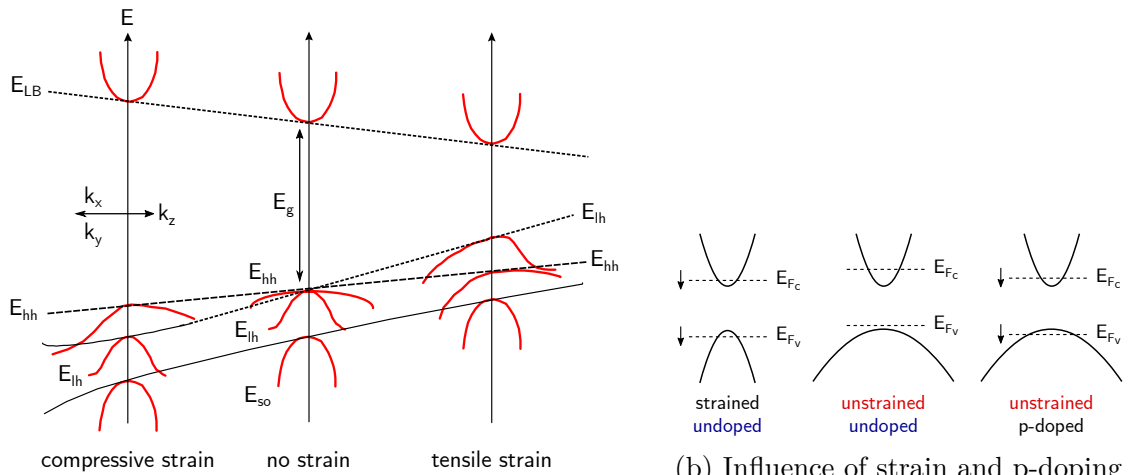
(a) Splitting of valence bands due to strain via lattice-mismatching of the QW to the waveguide. Adapted from [24, p. 108].

(b) Influence of strain and p-doping on the curvatures and quasi-Fermi energies. Adapted from [26, p. 219].

Figure 3.3.: Types of strain for intrinsic and undoped quantum wells and their influence on the energy bands and quasi-Fermi energies (schematic). Compressively strained quantum wells split up the degeneration of the lh- and hh-bands at the Γ-point, leading to more efficient electron-hole-recombinations. This leads to a plethora of desirable effects such as lower transparency current, higher internal quantum efficiency or faster-growing differential gain.

pp. 218–220]. Strain also increases the curvature of the valence band, which reduces the effective mass of holes and results in an approximate equilibrium with the eff. electron mass $m_e^* \approx m_h^*$. This balance induces a more efficient recombination and by that increases the internal quantum efficiency. Additionally, the transparency current I_{tr} shrinks up to a factor of 2 (likewise does the threshold current I_{th}, cf. eq. (5.6)) and the differential gain $g' = \mathrm{d}g/\mathrm{d}N$ of the strained QW grows faster [26, p. 219].

The splitting of the valence bands also has the effect that a polarization direction of the laser light is emitted preferentially. This is due to the orientation of the p-orbitals p_x, p_y, p_z which are predominantly involved in the transition: compressively strained QW emit transverse-electrically (TE) and tensely strained QW transverse-magnetically (TM) polarized light, i.e. perpendicular to the QW plane or parallel to it [24, p. 107]. The InGaAs quantum well lasers used in the thesis are compressively strained and emit TE-polarized light in the near-infrared to serve as pump sources for ytterbium-doped fiber lasers.

3.2. Buried Current Aperture by Deep Isolation Implantation

Standard diode lasers are grown on wafers in a single epitaxy-step using molecular organic vapor phase epitaxy (MOVPE). To achieve a lateral defined current flow and thereby gain-guiding, contact windows are shaped via appropriate metallization [24, p. 185]; shallow ion (e.g. He^+) implantation between p-contact layer and p-metal [24, p. 185]; insulating dielectric layers (e.g. from SiO_2 or Al_2O_3) (and shallow etching of the p-contact layer) [24, p. 187] or by combinations of these as with the diodes of this thesis (p-contact metallization and shallow implantation). On the contrary, the novel diodes of this thesis are manufactured in a two-step epitaxial process, which is depicted in fig. 3.4. Here, the current confinement is achieved by realizing a buried current aperture (BCA) through a technique called *isolation implantation*. The two-step epitaxy enables the deposition of an additional sub-contact layer between p-contact and p-cladding (etch stop) to reduce mechanically stress-induced strain on the quantum well. This layer is important in the light of extra processing steps that exert further stress on the diode.

In the 1st epitaxial phase, the laser structures in fig. 3.4 are deposited on a n-doped GaAs substrate. In general, all n-semiconductors in this thesis are doped with silicon at varying concentration levels. The GaAs substrate is followed by a GaAs buffer layer, the $Al_xGa_{1-x}As$ n-cladding and the $Al_yGa_{1-y}As$ n-waveguide layers,
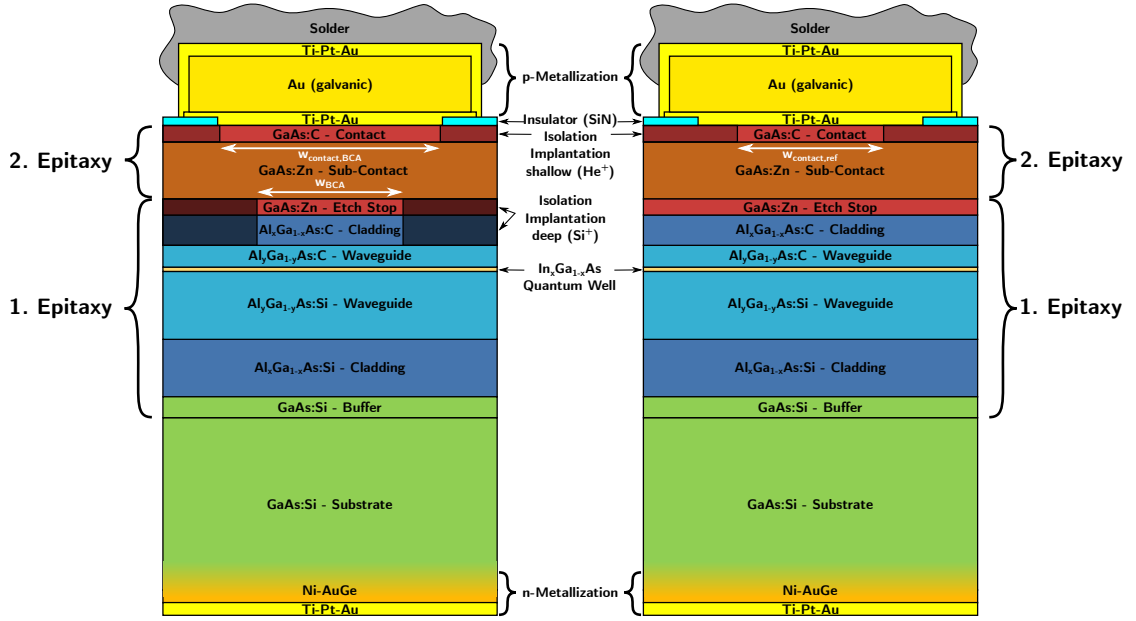
Figure 3.4.: Epitaxial structures of the investigated diodes (not to scale) with naming scheme material:dopant - function. **Left**: Diode with buried current aperture of width $w_{\mathrm{BCA}} = 100\,\mu\mathrm{m}$ and wide p-contact window $w_{\mathrm{p\text{-}contact}}^{\mathrm{BCA}} = 400\,\mu\mathrm{m}$. **Right**: Reference diode without current aperture and with narrower p-contact window $w_{\mathrm{p\text{-}contact}}^{\mathrm{ref}} = 100\,\mu\mathrm{m}$. Both structures are grown in a two-step epitaxy.

which serve the electrical and optical confinement of the double heterostructure (cf. fig. 3.2). Additionally, the n-cladding possesses a high doping concentration $\sim 10^{18}\,\mathrm{cm}^{-3}$ to supply free conduction band electrons as charge carriers - in contrast to the weakly doped $\sim 10^{17}\,\mathrm{cm}^{-3}$ n-waveguide for the reduction of optical absorption losses [22]. Next, the waveguide is grown lattice-mismatched to the single InGaAs quantum well. This induces a compressive strain, which allows the InGaAs QW to be employed as active zone for the emission of TE-polarized light in the near-infrared. In accordance with the EDAS design, the p-doped side of the laser is thinner than the n-doped side and is doped with carbon instead of silicon - with the exception of the zinc-p-doped etch stop and sub-contact layers. The waveguide and cladding layers fulfill the same functions for the valence band holes as their n-pendants do for the conduction band electrons. The first epitaxy step is completed by a highly p-doped GaAs etch stop, which protects the AlGaAs cladding layer from oxidation after the first epitaxy phase.

After the 1st epitaxy, an electric field accelerates Si^+ ions with an energy of $250\,\mathrm{keV}$ at a dose of $1.6 \cdot 10^{14}\,\mathrm{cm}^{-2}$ onto the previously grown laser structure outside of

w_{BCA}. As a result of the ion bombardment, the local crystal lattice is damaged (shaded areas in fig. 3.4). The ions penetrate deep into the etch stop and p-cladding, where they collide (elastically) with the atomic nuclei. This displaces the nuclei from their lattice positions, in turn causing them to collide with further lattice atoms. The subsequent collision cascade causes a variety of defects in the crystal lattice, such as interstitial atoms, vacancies or Frenkel pairs (interstitial atom + vacancy) [34, p. 501]. In the end, the final concentration of the implanted Si$^+$ ions is about two times as big as the already existent doping concentration of the p-cladding layer in order to overcompensate the impact of the doping [35, p. 328] (which is still much smaller than the concentration of GaAs atoms).

In the 2nd epitaxy step, the p-doped GaAs sub-contact layer and the very high p-doped ($\sim 2 \cdot 10^{19}\,\mathrm{cm}^{-3}$) GaAs contact layer are deposited. These two layers serve to protect the diode from mechanical stress, to which it is exposed to during lifetime. Then, He$^+$ ions are used for a shallow isolation implantation into the p-contact layer to define the p-contact window of width $w_{\mathrm{p\text{-}contact}}^{\mathrm{BCA}} = 400\,\mu\mathrm{m} > w_{\mathrm{BCA}} = 100\,\mu\mathrm{m}$. Furthermore, the second epitaxy fulfills the task of a (quasi-) annealing - the thermal healing of the previously created physical crystal defects at high temperatures (approx. $800\,^\circ\mathrm{C}$). Therefore, the BCA's functionality can only be based on chemical effects. In fact, the implanted silicon ions are incorporated into the crystal lattice. As a consequence, they generate deep chemically-activated donor impurities in the bandgap [22]. These impurities act as charge carrier traps, which recombine with holes. They are not thermally ionized at operating temperatures [35, p. 327] and insulate implanted p-regions. The remaining metal layers (Ni-AuGe, Ti-Pt-Au, Au) are deposited via wafer processing, which is of less relevance for this thesis and can be read in standard literature, e.g. [24, pp. 184–199].

Once the wafer is processed, the front facet is coated anti-reflective ($R_f = 2\,\%$, typ. $\mathrm{Al_2O_3}$) and the back facet high-reflective ($R_r = 97\,\%$, e.g. ZnSe or $\mathrm{TiO_2}$). In the penultimate processing step, the broad-area laser is soldered p-down onto a CuW submount (cf. fig. 3.5a), which has a thermal expansion coefficient that is comparable to the one of gallium arsenide ($\alpha_{\mathrm{lin}} \approx 5.7 \cdot 10^{-6}\,/^\circ\mathrm{C}$ [36]). Thus, the submount's thermal expansion is adapted to the laser for a protection against strains. Finally, the lasers are soldered into conduction-cooled packages (CCP, cf. fig. 3.5b) and ultimately installed onto hard-gold plated copper heat sinks. CCPs are expensive due to the choice of material and complexity in production. Yet, they improve the heat disposal, which enables a more reliable, durable and efficient laser operation thanks to reduced heat losses.
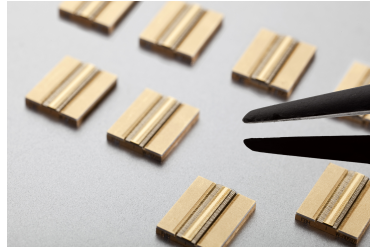
(a) BAL on CuW submount
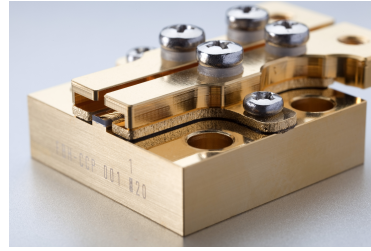
(b) Conduction-cooled pack-age

Figure 3.5.: Photographs of broad-area diode lasers soldered onto CuW submounts and CCP mounts.

3.3. Expected Impact of Buried Current Apertures on Electro-Optical Parameters

In gain-guided lasers, the current's path and thereby the gain profile are determined by the p-contact's area. Nevertheless, the current does not flow perfectly vertical through the laser. Due to the finite conductivities, it is subject to current spreading into the lateral peripheral areas of the QW [37, 38], especially in the p-doped layers as depicted in fig. 2.3. Mostly, charge carrier densities N do not reach the threshold density N_{th} (cf. eq. (5.8)) there. For this reason, carriers recombine predominantly spontaneously or non-radiatively, i.e. do not contribute to the optical output power, heat the device and reduce quantum efficiency (cf. eq. (5.4)). Upon reaching threshold, higher-order lateral modes can be amplified, degrading the lateral beam quality. An implantation of a buried current aperture (BCA) should address these issues as follows.

The high electrical resistance of isolation-implanted zones reduces the current spread I_{spr} to lateral outer-regions. In this way, the ratio of radiatively recombining to injected charge carriers – the internal quantum efficiency η_{int} – should improve. Additionally, the carrier density N in the quantum well below the buried current aperture should grow. By that, threshold current I_{th} shrinks, in return boosting the optical output power P_{opt} (cf. eq. (5.1)). By guiding the current just above the QW, the BCA decouples the pumped area from the overlying p-doped layers and p-contact. This increases the critical thickness for suppressing a certain amount of current spread, which can be utilized by the two-step epitaxy. On the one hand, it enables the deposition of an additional p-doped GaAs sub-contact layer (cf. fig. 3.4) to compensate for mechanically induced stress, to which the diode is exposed during coating and mounting processes. On the other hand, it allows

the p-contact's area A to be enlarged, thus reducing the series resistance R_s of the laser. This is necessary, since the additional p-sub-contact layer as well as the compressed cross-sectional current area increase the series resistance $R_s \propto 1/A$. It remains to be seen in section 6.1, which effect prevails. Furthermore, the larger p-contact area facilitates a more efficient heat disposal, which reduces the thermal resistance R_{th} and by that active zone temperature rise ΔT_{az} with current.

The lateral near-field width w_{NF} is affected by the reduced pump area and shrinks, accordingly. Likewise, a higher current density in the lateral center $x \leq 50\,\mu\text{m}$ than in the outer-region $|x| > 50\,\mu\text{m}$ results in a stronger lateral heat gradient, which intensifies the temperature-induced index change Δn_T (cf. eq. (4.6)). At the same time, this heat gradient and thereby the *thermal lens* shortens in the lateral direction, since the mitigated current spread of BCA designs implies less non-radiative recombinations heating the lateral outer-region. As a consequence, one effect could dominate over the other or both effects could balance each other out. On one side, a lowered effective strength of the thermal lens could delay a narrowing of the near-field and equivalent widening (thermal *blooming*) of the far-field [39]. The beam quality (BPP$_{\text{lat}}$) would benefit from the reduced near-field width and decreased far-field divergence angle at high currents and improve according to eq. (5.25). In case of no effective change of the thermal lens' strength, smaller near-fields would compensate more divergent far-fields and hence not change the beam quality at all. Lastly, the thermal lens could even be enhanced, which would lead to a degradation of the beam quality. Beyond that, a buried current aperture should cause a laterally more homogeneous current profile and thereby a more homogeneous near- and far-field distribution than its reference.

The potential advantages of buried current apertures are contrasted with the potential risks of the two-step epitaxy compared to conventional one-step epitaxy. The former is more complex and requires additional work steps. Therefore, it is more likely that the crystal lattice or diodes are damaged or stressed. It is reasonable to assume that the two-step epitaxy's crystal quality cannot compete with that of the one-step epitaxy, since the epitaxy process is interrupted. This could introduce impurities, which act as scatter centers and produce heat. In turn, the internal quantum efficiency η_{int} would be lowered (cf. eq. (5.12)), and ultimately the device's output power, reliability and longevity.

4. Mathematical Models for Simulating BAL Dynamics

The professional software kit *BALaser* allows the simulation of nonlinear dynamics in high-power edge-emitting **B**road-**A**rea **Laser**s and is being developed at the *Weierstraß-Institute for Applied Analysis and Stochastics* (WIAS) in Berlin. The challenge of simulating a BAL's dynamics is founded on its wide range of spatial dimensions, e.g. vertical QW thickness (7 nm) vs. lateral active zone (BCA) width (100 µm) vs. longitudinal resonator length (6 mm), and temporal dimensions, e.g. changes of the optical field amplitudes (ps) vs. carrier densities (ns) vs. lattice temperature (µs). Such precise simulations require immense processing times of many hours up to several days, even though utilizing efficient algorithms being performed on a parallel computation cluster at the WIAS.

The author did not conduct the simulations himself[1], which is why the subsequent physical models will only cover *BALaser*'s fundamental aspects necessary to understand the presented results. For the sake of readability, functional space (x,y,z) and time t dependencies will only be written were of importance. A partial operator ∂_i denotes a partial derivation with respect to i. The information presented in this chapter originates mainly from the publications of Anissa Zeghuzi et al. [17, 39, 40], Hans Wenzel and Anissa Zeghuzi [41], and partly from Mindaugas Radziunas et al. [42, 43].

4.1. Optical Model

In *BALaser*, the dynamic optical fields are modeled by a 2(space)+1(time)-dimensional traveling wave model. The model makes use of the paraxial, rotating wave and slowly-varying envelope amplitude (SVEA) approximations [41, pp. 20 sqq.]. In the first, it is assumed that the laser beam deviates only slightly from the optical axis $z \gg \sqrt{x^2 + y^2}$, i.e. behaves like a Gaussian beam; while in

---

[1]The author thanks Anissa Zeghuzi for simulating the investigated designs and gratefully acknowledges her support during troubleshooting.

the second, rapidly rotating terms of the form $e^{-i2\omega_0 t}$ and in the third, 2nd-order time $\left|\frac{\partial E}{\partial t^2}\right| \ll \left|\omega \frac{\partial E}{\partial t}\right|$ and space $|\nabla^2 E| \ll |\vec{k}\nabla E|$ derivatives of the electric field $\vec{E}$ are neglected. As a consequence, the optical field superposes as follows:

$$\vec{E}(\vec{r},t) = \vec{e}_x A\Phi(y)\left[E^+(x,z,t)e^{-i\bar{n}k_0 z} + E^-(x,z,t)e^{i\bar{n}k_0 z}\right]e^{i\omega t} + c.c.. \tag{4.1}$$

Here, $E^+(x,z,t)$ denotes forward and $E^-(x,z,t)$ backward traveling TE-polarized waves in the lateral-longitudinal (x,z)-plane of the active zone (the resonator), with *c.c.* as complex conjugate of the first term. Modal properties are encoded in the vertical mode profile $Phi(y)$ (see below), while wavelength properties are represented by the vacuum wave number $k_0 = \omega/c_0 = 2\pi/\lambda_0$, the light's angular frequency ω and wavelength $\lambda_0 = 910\,\mathrm{nm}$, and the vacuum speed of light c_0. The factor $A = \sqrt{d\hbar\omega/(\epsilon_0 \bar{n} n_g)}$ is chosen such that

$$\|E\|^2 = \left|E^+(x,z,t)\right|^2 + \left|E^-(x,z,t)\right|^2 \tag{4.2}$$

is the cavity's photon density, where $d = 7\,\mathrm{nm}$ is the thickness of the active zone, $\hbar$ the reduced Planck constant, ϵ_0 the vacuum permittivity, $\bar{n} = 3.42$ a real-valued refractive background (or reference) index and $n_g = 3.92$ the group index.

All parameters entering eq. (4.1) and the model in general are provided by the *effective index method* (EIM). An effective refractive index change Δn_eff quantifies the wavenumber increase caused by an optical waveguide structure as in diode lasers. The EIM parameters are obtained by multiplying the laser's material parameters (gain, refractive indices, absorption losses,...) with the (transverse) confinement factor $\Gamma = 6.6 \cdot 10^{-3}$ (cf. eq. (2.9)). The latter results from numerical calculations of the real-valued normalized vertical mode profile $\Phi(y)$ of the fundamental mode for the cold cavity; $\Phi(y)$ itself originates from the refractive indices of the epitaxial structure. Then, the traveling waves $E^\pm$ in eq. (4.1) are coupled to each other by the semi-classical traveling wave equations with reflecting boundary conditions at the resonator's facets:

$$\left[\frac{1}{v_g}\partial_t \pm \partial_z\right]E^\pm = \left[-\frac{i}{2\bar{n}k_0}\partial_x^2 - i\Delta\beta(x,z,N(t),T(t),\|E\|^2) + \mathcal{D}\right]E^\pm + F_{sp}^\pm \tag{4.3}$$

where $v_g = c_0/n_g$ is the group velocity and $F_{sp}^\pm$ a stochastic Langevin force modeling spontaneous emission. Likewise the latter, the first term on the right-hand side of eq. (4.3) accounts for diffraction, the second term for complex modal propagation

and the third term for dispersion of the optical field, with the dispersion operator $\mathcal{D}$ (see further below). The complex modal propagation constant $\Delta\beta$ is defined as follows:

$$
\begin{aligned}
\Delta\beta(N,T,\|E\|^2) &= k_0 \Delta n_{\text{eff}}(N,x,z,t) + \frac{i}{2}\left[g_{\text{eff}}(N,\|E\|^2) - \alpha_{\text{eff}}(N)\right] \\
&= k_0 \left[\Delta n_0(x,z) + \Delta n_N(x,z,N) + \Delta n_T(T)\right] \\
&\quad + \frac{i}{2}\left[g_{\text{eff}}(N,\|E\|^2) - \alpha_{\text{eff}}(N)\right].
\end{aligned}
\tag{4.4}
$$

In this equation, $\Delta n_0 = n_0 - \bar{n}$ resembles the deviation of a built-in refractive index n_0 (only nonzero at transverse positions (x,z) of, e.g. optionally etched trenches) to the background index, while

$$
\Delta n_N = -\sqrt{n'N}
\tag{4.5}
$$

corresponds to the (electronic) refractive index change due to changes in the carrier density N, with $n' = 4.4 \cdot 10^{-32}\,\text{m}^3$ as index-change factor [44]. The influence of the local temperature $T(x,z)$ on the refractive index with respect to the heat-sink temperature $T_{\text{HS}} = 300\,\text{K}$ (experiment: $25\,°\text{C} = 298.15\,\text{K}$) is modeled via the thermal index change

$$
\Delta n_T(T) = \int n'_T \left[T(x,z) - T_{\text{HS}}\right] |\Phi(y)|^2 \, dy,
\tag{4.6}
$$

where $n'_T = \partial\bar{n}/\partial T = 2.5 \cdot 10^{-4}\,\text{K}^{-1}$ is the temperature-induced differential index. In other words: high carrier densities N lower the refractive index, while high temperatures T raise it. The last term in eq. (4.4) models the effective gain (also titled "net gain")

$$
g_{\text{eff}}(N) = g' \frac{\ln\left(N/N_{tr}\right)}{1 + \epsilon_s \|E\|^2}
\tag{4.7}
$$

with the differential modal gain $g' = 1655\,\text{m}^{-1}$, the transparency carrier density $N_{tr} = 1.7 \cdot 10^{24}\,\text{m}^{-3}$ and the gain compression factor $\epsilon_s = 6.6 \cdot 10^{-26}\,\text{m}^3$ (modeling spectral hole burning and carrier heating [45]); and effective losses

$$
\alpha_{\text{eff}} = \alpha_{0,\text{eff}} + f_N \cdot N + f_{2P} \cdot \left(\|E\|^2 + \left|E^{\mp}\right|^2\right)
\tag{4.8}
$$

with $\alpha_{0,\text{eff}} = 47\,\text{m}^{-1}$ as eff. internal background absorption due to free-carrier absorption (FCA), $f_N = \Gamma\sigma_N = 16\cdot 10^{-22}\,\text{m}^2$ as modal cross section for FCA in the active region (FCA cross section σ_N) and f_{2P} as modal two-photon absorption coefficient (not relevant for the investigated lasers, only at much higher power densities). At the transparency carrier density N_{tr} (typ. ~$1.8\cdot 10^{18}\,\text{cm}^{-3}$ for an InGaAs/GaAS SQW [26, p. 87]) propagating waves with wavelength λ_0 in the QW will neither be amplified nor absorbed - the medium becomes "transparent".

Since light disperses in refractive media, the slowly varying amplitudes of the macroscopic polarization fields P are coupled to ordinary differential equations for the dispersion, too:

$$\mathcal{D}E^\pm = \frac{g_r}{2}\left(E^\pm - P^\pm\right) \tag{4.9}$$

$$\partial_t P^\pm = \gamma\ \left(E^\pm - P^\pm\right) + i\delta\omega P^\pm \tag{4.10}$$

These equations represent an approximation of the dispersing gain with a Lorentz function of amplitude g_r, half width at half maximum γ and relative central frequency $\delta\omega$.

In short, the electric waves travel through an optical resonator, where they experience gain, loss and dispersion effects being described by eq. (4.2) and eqs. (4.4) to (4.10).

4.2. Carrier Transport and Current Spreading Model

In a BA laser, the resonator's longitudinal dimension (here: 6 mm) is much longer than its lateral dimension (here: 100 µm). This results in only small carrier density gradients in the longitudinal direction compared to the lateral direction $\partial_z N$. Therefore, longitudinal carrier transport will be neglected. A more detailed derivation of the following equations can be found in appendix A.1.

Carrier transport through semiconductors is explained by a carrier diffusion and drift model. The particle flows, i.e. the electron $\vec{j}_n$ and hole $\vec{j}_p$ current densities, depend on the electron σ_n and hole σ_p conductivities of the involved n- and p-layers, as well as on the electron φ_n and hole φ_p quasi-Fermi potentials:

$$\vec{j}_n = +\sigma_n \nabla \varphi_n \tag{4.11}$$

$$\vec{j}_p = -\sigma_p \nabla \varphi_p. \tag{4.12}$$

These densities are affected by the epitaxial vertical double heterostructure, such that they spread on their way to the active zone. Since electron conductivities in n-doped semiconductors are about three times greater than those of holes in p-doped layers (cf. section 3.1), they spread much less than holes. When neglecting the small lateral voltage drop caused by the electron current spreading in comparison to the hole current spreading, a flat quasi-Fermi potential $\nabla \varphi_n \approx 0$ is yielded [46]. As a consequence, a constant electron quasi-Fermi potential can be assumed, which is set to zero $\varphi_n \approx \text{const} = 0$. This means, that the electron current density $\vec{j}_n$ in eq. (4.11) consists only of its vertical component $j_{n,y}$ which does not vary in the vertical direction. Consequently, the total current density $j(N)$ injected into the active region is controlled by the varying hole current density $\vec{j}_p$, and as such by the hole current spread. Due to high potential barriers provided by the epitaxial structure, vertical hole leakage currents can be disregarded. By assuming only lateral carrier diffusion and drift in the thin quantum well, the continuity equation for the hole current density $\vec{j}_p$ can be averaged over the QW thickness d, which ultimately reveals the carrier diffusion equation:

$$\partial_t N = \partial_x \left[D_{\text{eff}}(N) \partial_x N \right] + \frac{j}{ed} - R\left(N, \|E\|^2\right). \tag{4.13}$$

Here, $j(N) = j_{p_y}$ is the injection current density at the boundary of the active zone adjacent to the p-doped region, e the elementary charge and

$$
\begin{aligned}
R(N, \|E\|^2) &= R_{\text{SRH}} + R_{\text{spont}} + R_{\text{Auger}} + R_{\text{stim}} \\
&= AN \;\; + BN^2 \;\; + CN^3 \;\; + R_{\text{stim}}(N, \|E\|^2)
\end{aligned}
\tag{4.14}
$$

the effective recombination (transition) rate $R(N, \|E\|^2) = \tau(N)/N$, with $\tau(N)$ as effective carrier lifetime (until recombination). Here, the first and third terms relate to the nonradiative Shockley-Read-Hall and Auger recombinations, and the second and fourth terms to the radiative spontaneous and stimulated recombinations, with their corresponding recombination coefficients $A = 2 \cdot 10^8 \, \text{s}^{-1}$, $B = 10^{-16} \, \text{m}^3 \, \text{s}^{-1}$ and $C = 4 \cdot 10^{-42} \, \text{m}^6/\text{s}$ (ABC model). The stimulated recombination rate itself is given as:

$$R_{\text{stim}}(N, \|E\|^2) = v_g Re \left[\sum_{i=\pm} E^{i*} \left[g_{\text{eff}}(N, \|E\|^2) E^i - g_r \left(E^i - P^i \right) \right] \right].\qquad(4.15)$$

Equation (4.13) couples the excess carrier density $N(x,z,t)$ to the traveling wave propagation in eq. (4.3), or in other terms the carrier transport to the optical model.

The total current density in the active zone $j(N)$ can be calculated by inserting eq. (A.6) into the hole continuity equation eq. (A.4) in the case of negligible bulk recombination $\nabla \cdot \vec{j}_p = 0$ which yields the Laplace problem for the hole quasi-Fermi potential:

$$\nabla \left(\sigma_p \nabla \varphi_p \right) = 0.\qquad(4.16)$$

This Laplace problem is solvable when applying appropriate vertical boundary conditions ($y = 0$: n-contact, $y = H$: p-contact):

- in the active zone: $\varphi_p|_{y=az} = U_F(N,T)$ with the Fermi voltage $U_F = \varphi_p - \varphi_n$

- at the n- and p-metal contacts: $\varphi_n|_{y=H} = \varphi_p|_{y=H} = U$ and $\varphi_n|_{y=0} = \varphi_p|_{y=0} = 0$ with the applied forward biased voltage U

- remaining device boundaries: $\partial_n \varphi_p = 0$ where ∂_n denotes the normal derivative to the device surface (no vertical y-components of electron current at p-metal contact and hole current at n-metal contact).

Last but not least, the threshold current I_{th} can be formulated in dependence on the lateral spreading current $I_{\text{spr}} = I_{p_x} = j_{p_x}/(LW)$ (cf. eq. (A.15)) [20]:

$$I_{\text{th}}(w) = j_{th, w\to\infty} Lw + I_{\text{spr}}\qquad(4.17)$$

where it is assumed that I_{spr} is independent of the p-contact width w. A current density - dependent formulation can be acquired by dividing eq. (4.17) by Lw. The current density $j_{th, w\to\infty}$ corresponds to the case of an infinitely wide p-contact without any current spreading and can be derived as slope by plotting the threshold current $I_{\text{th}}(w)$ dependence on the p-contact width w for several lasers with different contact widths (not to be done in this thesis). In a similar way, I_{spr} can be obtained for the case of infinitely small contact width $w \to 0$. From eq. (4.17) follows that the threshold current can be either reduced by decreasing the p-contact width w, cavity length L or spreading current I_{spr} (cf. eq. (5.6)).

4.3. Thermodynamic Model

In a p-i-n-semiconductor carriers and phonons relax much faster (ps) to their thermal equilibrium states than they recombine (lifetime). Thus, relaxations can be regarded as instantaneous, with h as the amount of released heat energy being transferred to the thermalized system per unit time and unit volume. The thermodynamic model presented here considers four heat sources.

4.3.1. Heat Generation Model

The first heat source arises from charge carrier scattering at atomic ions (Drude model) and is called Ohmic or Joule heating. Similar to the carrier transport and current model, electrons in the n-doped regions possess high conductivities, which is the reason for the neglection of (electronic) Joule heating h_J. But for the p-doped regions it is given as

$$h_J = h_{J,p} = \frac{j_p^2}{\sigma_p}. \tag{4.18}$$

The second heat source h_{abs} stems from the absorption of photons from stimulated emission. It is separated into parts for outside the active zone

$$
\begin{aligned}
h_{\text{abs,w/az}} = \ & v_g \hbar \omega d \quad \alpha_0(y) \ \frac{n(y)}{\bar{n}} \left|\phi(y)\right|^2 \left\|E(x,z,t)\right\|^2 \\
& + (v_g \hbar \omega d)^2 \beta_{2P}(y) \frac{n(y)}{\bar{n}} \left|\phi(y)\right|^4 \left\|E(x,z,t)\right\|^4
\end{aligned}
\tag{4.19}
$$

and inside the active zone

$$h_{\text{abs,az}} = v_g \hbar \omega f_N N \|E(x,z,t)\|^2, \tag{4.20}$$

where the vertically distributed parameters stand for absorption $\alpha_0(y)$, the real part of the refractive index $n(y)$ and the two-photon absorption coefficient $\beta_{2P}(y)$ (not to be confused with its modal counterpart f_{2P}). In eq. (4.19) background absorption due to doping is represented by the first term, and two-photon absorption in the cladding and waveguiding layers by the second term. Equation (4.20) describes the heating by free carrier absorption in the active zone.

The third heat source emanates from recombinations in the active zone, which is governed by the ABC model:

$$h_{\text{rec,az}} = eU_F(N,T)\left(AN + BN^2 + CN^3\right). \tag{4.21}$$

Here, it has been assumed that $100\,\%$ of reabsorbed spontaneously emitted photons are transformed to heat energy, which is an obvious overestimation since photons can be absorbed in any layer or leave the cavity at the front facet. Nevertheless, this approximation suffices, as far above threshold spontaneous recombinations barely contribute to the heat generation [47]. Also, the lateral temperature distribution is only insignificantly influenced by its vertical analogue.

Finally, the fourth heat source accounts for quantum defect heating:

$$h_{\text{defect}} = R_{\text{stim}}(N,\|E\|^2) \cdot (eU_F(N,T) - \hbar\omega). \tag{4.22}$$

It arises during stimulated recombination, when portions of the carrier energies are converted to heat.

4.3.2. Heat Flow Model

The thermodynamic heat flow is modeled by the macroscopic heat flow equation:

$$c_h \partial_t T - \nabla\left(\kappa_L \nabla T\right) = h(N,\vec{j},\|E\|^2) \tag{4.23}$$

where $c_h \approx 10^6\,\text{J}\,\text{K}^{-1}\,\text{m}^{-3}$ is the heat capacity, $\kappa_L \approx 5 - 200\,\text{W}\,\text{K}^{-1}\,\text{m}^{-1}$ the specific heat conductivity (see table 4.1 for values of κ_L and c_h per layer) and

$$h = h_J + h_{\text{abs}} + h_{\text{rec}} + h_{\text{defect}} \tag{4.24}$$

the summarized heat energy per unit time and unit volume. On the one hand, $h(N,\vec{j},\|E\|^2)$ is influenced by the parameters (excess carrier, injection current and photon density) in its arguments. On the other hand, the heat will modulate the refractive index thermally and with it the light waves' propagation (cf. eq. (4.4)). It also affects the carrier distributions and diffusion, the gain and the recombinations in an implicit way. Equation (4.23) obeys the subsequent boundary conditions:

- (x,y,z) inside the heat sink: $\kappa_L \partial_n T = -\dfrac{T - T_{\text{HS}}}{r_{\text{th}}}$

- (x,y,z) at other outer bounds: $\partial_n T = 0$

Here, $r_{\text{th}} = 5.5 \cdot 10^{-6}\,\text{K}\,\text{m}^2\,\text{W}^{-1}$ encodes the inverse heat transfer coefficient or thermal transmission resistance, with T as absolute and T_{HS} as heat sink temperature. In order to avoid simulating the heat flow over tens of microseconds while the optical model has a temporal resolution of sub-picoseconds – or in other words, to efficiently implement the heat flow equation into the simulation model – some approximations have to be made. These will be sketched in the following.

For short time spans less than $10\,\text{ns}$, transverse (longitudinal z + lateral x) heat flow can be neglected since its spread is much smaller (about $100\,\text{nm}^2$ in $1\,\text{ns}$) than the transverse inhomogeneities of the heat source densities across the $100\,\text{µm} \times 6\,\text{mm}$ active zone (cf. fig. 6.5d). During CW-operation temperatures build up over a substantially longer time span, so that this approximation does not hold. But after some time passes, a quasi-steady state emerges with only minimal residing chaotic fluctuations. Then, the heat flow equation can be split into two parts for a time-constant mean contribution $\bar{h}$ and a fluctuating contribution $h_{\text{fluc}} = h - \bar{h}$, whereas for the latter heat flow can be neglected.

To correctly model the interplay of opto-electronic and thermal effects as described above, the opto-electronic model is iteratively coupled to the heat transport model. In the first iteration, the electro-optical model is solved without assuming a temperature distribution. In the next step, the heat sources are calculated and the stationary heat flow equation is solved. The obtained temperature distribution is then used in the last iteration step. For the simulations discussed in chapter 6, a total of three iterations was performed, with a simulation time of $5\,\text{ns}$ per iteration step. Further details can be read in [39].

Table 4.1.: Important simulation parameters.

Symbol	Quantity	Value	Unit
n_g	group refractive index	3.92	
$\bar{n}$	background/reference refractive index	3.42	
λ_0	central wavelength	$910 \cdot 10^{-9}$	m
r_0	rear facet field amplitude reflectivity	$\sqrt{0.95}$	
r_L	front facet field amplitude reflectivity	$\sqrt{0.01}$	
d	thickness of active region	$7 \cdot 10^{-9}$	m
Γ	confinement factor in active region	$6.6 \cdot 10^{-3}$	
g'	differential modal gain	1655	m^{-1}
N_tr	transparency carrier density	$1.7 \cdot 10^{24}$	m^{-3}
ϵ_s	gain compression factor	$6.6 \cdot 10^{-26}$	m^3
$\alpha_{0,\mathrm{eff}}$	effective internal background absorption	47	m^{-1}
f_N	cross section for free carrier absorption	$16 \cdot 10^{-22}$	m^2
n'_N	carrier density induced differential index	$4.4 \cdot 10^{-32}$	m^3
n'_T	temperature induced differential index	$2.5 \cdot 10^{-4}$	K^{-1}
A	Shockley-Read-Hall recombination coeff.	$2 \cdot 10^8$	s^{-1}
B	spontaneous emission recombination coeff.	$1 \cdot 10^{-16}$	$\mathrm{m}^3\mathrm{s}^{-1}$
C	Auger recombination coeff.	$4 \cdot 10^{-42}$	$\mathrm{m}^6\mathrm{s}^{-1}$
r_th	thermal transmission resistance	$5.5 \cdot 10^{-6}$	$\mathrm{Km}^2\mathrm{W}^{-1}$
T_HS	heat sink temperature	300	K
κ_L	heat conductivity		
	semiconductor layers	11 to 16	$\mathrm{W(Km)}^{-1}$
	insulation / substrate & contact-layer	5 / 44	$\mathrm{W(Km)}^{-1}$
	gold-contact / submount	70 / 200	$\mathrm{W(Km)}^{-1}$
c_h	heat capacity		
	semiconductor layers	$1.7 - 1.8 \cdot 10^6$	$\mathrm{JK}^{-1}\mathrm{m}^{-3}$
	gold contact	$2.47 \cdot 10^6$	$\mathrm{JK}^{-1}\mathrm{m}^{-3}$
	submount	$2.82 \cdot 10^6$	$\mathrm{JK}^{-1}\mathrm{m}^{-3}$

5. Measurement Setups and Determination of Characteristic Parameters

All measuring stations share the same base structure, on which the laser diodes are installed. From the bottom upwards, this structure consists of:

- adjustment tables for the vernier adjustment of the lasers

- a Cu heat sink with attached water cooling for the dissipation of waste heat from the Peltier element

- a Peltier element to temper the heat sink on 25 °C

- a CCP mount with the laser diode

- a temperature control device to temper the Peltier element and measure the mount's temperature

- a power supply to operate the laser diodes (not drawn)

The power supplies and temperature controllers employed are listed in table 5.1.

Table 5.1.: Power supplies and temperature controllers at the measurement stations.

Station	Power Supply	Temperature Controller
PUI, Spectrum Polarization	LDX-36000	Newport Model 3150 arroyo 5400
Beam Caustic	arroyo 4320	arroyo 5310

5.1. Power(P)-Voltage(U)-Current(I) Characterization

The setup in fig. 5.1 records the optical output power P_{opt} and the diode voltage U of a mounted laser as a function of its pump current I. A *Keithley Multimeter 2000* measures the voltage between heat sink (p-contact) and mount (n-contact). For power measurement, a *gentec UP19K-15S-W5-D0* thermoelectric sensor is mounted on a rail at a fixed distance. It converts the near-infrared radiation of the diode into electrical energy, which in turn is assigned to an output power by means of an internal calibration table. The optical output power results as follows:

$$P_{opt}(I) = \frac{h\nu}{e} \cdot \eta_{\text{int}} \cdot \frac{\alpha_{\text{mir}}}{\alpha_{\text{mir}} + \alpha_{\text{int}}} \cdot (I - I_{\text{th}}). \tag{5.1}$$

It depends on the energy of a photon $E = h\nu$ (Planck's constant h, frequency ν) per elementary charge e, the internal quantum efficiency η_{int} (the ratio of radiatively recombining to injected charge carriers), the losses at the mirror facets α_{mir} (cf. eq. (2.13)), the internal losses α_{int} (cf. eq. (2.10)) as well as the difference between pump current I and threshold current I_{th}. The facet losses again depend on the resonator length L and the reflectivities of the front facet R_f and back facet R_r:

$$\alpha_{\text{mir}} = \frac{1}{2L} \ln \left(\frac{1}{R_f R_r} \right). \tag{5.2}$$

Equation (5.1) can be briefly written as:

$$P_{opt} = \frac{h\nu}{e} \cdot \eta_{\text{ext}} \left(I - I_{\text{th}} \right) = S \left(I - I_{\text{th}} \right), \tag{5.3}$$

with the external differential quantum efficiency

$$\eta_{\text{ext}} = \eta_{\text{int}} \frac{\alpha_{\text{mir}}}{\alpha_{\text{mir}} + \alpha_{\text{int}}} \tag{5.4}$$

and the slope S[1] of the PUI curve. This relationship follows directly from the slope's definition:

---

[1]In the literature S is often labeled as "slope efficiency". However, the slope S is dimensional [W/A] for which reason the author refrains from referring to it as slope efficiency.
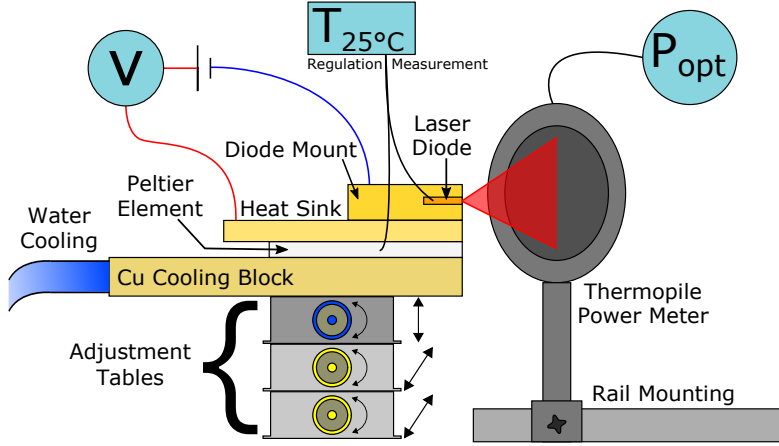
Figure 5.1.: Setup for measuring the power-voltage-current characteristics of a diode. A power supply pumps the diode with a constant current, while a voltmeter measures the diode voltage between diode mount and heat sink. The optical output power heats the thermopile power meter, creating an electrical signal, which is internally converted into a power value.

$$S = \frac{dP_{opt}}{dI} = \eta_{\text{ext}} \frac{h\nu}{e}. \tag{5.5}$$

Various effects such as thermal rollover at high currents or kinks can influence the linearity of a P(I)-curve. For this reason, characteristic parameters like slope S or series resistance R_s are only calculated from a linear regime at low currents, as will be elucidated in detail in chapter 6.

With the beginning of laser operation through stimulated emission, the output power increases abruptly, i.e. the slope changes in an interval dI by a large amount dS. This can be applied to determine the threshold current I_{th}. First, the local maximal peak of the slope's derivative dS/dI or, equivalently, the second derivative of the optical output power d^2P_{opt}/dI^2 is identified in the vicinity of the observed threshold. This peak is then fitted with a Gaussian bell curve to compensate for the current increment ΔI limiting the determination's precision. Lastly, the Gaussian's center x_c equals the threshold current I_{th} (cf. fig. 5.2c). The threshold current depends on the laser device as a whole. For SQW lasers [25, p. 54], I_{th} assembles from the QW's dimensions width w, length L and thickness d, internal losses α_{int} (without distinguishing active and passive losses in- and outside the AZ, respectively), mirror losses α_{mir} and confinement factor Γ to

$$I_{\text{th}} = w L j_{\text{tr}} \exp\left[\frac{\alpha_{\text{int}} + \alpha_{\text{mir}}}{\Gamma G_0}\right], \tag{5.6}$$

where j_{tr} is the transparency current density of the active medium:

$$j_{\text{tr}} = N_{\text{tr}} \frac{ed}{\eta_{\text{int}} \tau(N_{\text{tr}})} \tag{5.7}$$

with the transparency carrier density N_{tr} and carrier lifetime $\tau(N)$. Inserting eq. (5.7) into eq. (5.6), the threshold carrier density can be identified [26, p. 65]:

$$N_{\text{th}} = N_{\text{tr}} \exp\left(\frac{\alpha_{\text{int}} + \alpha_{\text{mir}}}{\Gamma G_0}\right), \tag{5.8}$$

which can be expressed in terms of the ABC model (cf. eq. (4.14)) *almost* at threshold [26, p. 60], i.e. without stimulated recombination, as

$$N_{\text{th}} = \tau(N_{\text{th}}) \left(A N_{\text{th}} + B N_{\text{th}}^2 + C N_{\text{th}}^3\right). \tag{5.9}$$

Combining eqs. (5.6) to (5.9) and understanding that Shockley-Read-Hall A and Auger C recombinations play a negligible role for state-of-the-art quantum well lasers near threshold, the threshold current for an active zone volume of $V_{\text{az}} = wLd$ becomes

$$I_{\text{th}} \cong N_{\text{tr}}^2 \frac{e V_{\text{az}}}{\eta_{\text{int}}} \exp\left(2\frac{\alpha_{\text{int}} + \alpha_{\text{mir}}}{\Gamma G_0}\right). \tag{5.10}$$

The gain prefactor G_0 is a constant that is proportional to the differential gain g' (cf. eq. (4.7)). Its analytical derivation and calculation is rather complex [48] and exceeds the scope of this thesis. Unfortunately, it can not be evaluated experimentally, either, since no identically constructed lasers with different cavity lengths L were fabricated. This holds also true for other characteristic parameters such as internal efficiency η_{int} and losses α_{int} or the transparency current density j_{tr}. An exemplary experimental determination of G_0 and cavity-length parameters can be found in [41, pp. 6–8]. When operated at high currents, a diode heats up due to the increase of Joule heating and losses. With increasing temperature, the laser performance degrades, which can be empirically modeled by an exponential threshold shift to higher currents [24, p. 200] [26, p. 82] [25, p. 75]:

$$I_{\text{th}}(T_2) = I_{\text{th}}(T_1) \exp\left(\frac{T_2 - T_1}{T_0}\right). \tag{5.11}$$

Here, $I_{\text{th}}(T_2)$ and $I_{\text{th}}(T_1)$ denote threshold currents at their respective ambient temperatures T_2 and $T_1 < T_2$, and T_0 the characteristic temperature of the threshold current. This behavior can be traced back to a related degradation of the external quantum efficiency:

$$\eta_{\text{ext},2}(T_2) = \eta_{\text{ext},1} \exp\left(\frac{T_1 - T_2}{T_\eta}\right), \tag{5.12}$$

where T_η is the characteristic temperature of the (external) quantum efficiency. T_0 and T_η are material parameters and measures for the temperature sensitivity of the laser device (typ. $T_0 \geq 200\,\text{K}$ and $T_\eta \sim (2-3)\,T_0$ for strained InGaAs/AlGaAs-QW lasers [26, p. 81]) – the higher T_0 and T_η, the less prone are the respective quantities to higher device temperatures. As a result of the threshold shift, the maximal output power that can be reached with a certain current, shrinks. The eqs. (5.11) and (5.12) describe the behavior of the diodes in short pulse operation with pulse widths below $1\,\mu\text{s}$ at a duty cycle of 1:1000 in the temperature range of 10-50 °C. Consequently, they neglect the self-heating during measurement and are only roughly valid for CW-operated lasers.

Another characteristic parameter for the performance of a laser diode is the conversion efficiency η_c, which relates the optical output power P_{opt} to the electrical input power $P_{el} = UI$:

$$\eta_c = \frac{P_{opt}}{UI}. \tag{5.13}$$

The conversion efficiency is an important figure of merit for high-power physics with laser bars and stacks reaching hundreds to thousands of watts of optical output power per device. For this reason and because its qualitative discussion at the highest measured current $\eta_c(12\,\text{A})$ does not differ from discussing the maximal output power $P_{\text{opt}}(12\,\text{A})$ due to their proportionality, the conversion efficiency will not be further evaluated in chapter 6. At max. current, the conversion efficiencies $\eta_c(12\,\text{A})$ of the investigated diodes range from 57 % to 61 %.

In terms of current-voltage characteristics, diodes obey the Shockley equation for a real heterojunction diode [49, p. 454][50]:

$$I(U) = I_{\text{sat}} \left[\exp\left(\frac{e(U - IR_s)}{nk_BT} \right) - 1 \right] \tag{5.14}$$

with the saturation current I_{sat}, the applied forward voltage U, the series resistance R_s (see below) and the diode ideality factor n. Often, the (inverted) factor e/k_BT is termed thermal voltage $V_T(T) = k_BT/e$. Equation (5.14) can be inverted to present the $U(I)$ characteristic of a real diode below threshold:

$$U(I) = IR_s + n\frac{k_BT}{e} \ln\left(1 + \frac{I}{I_{\text{sat}}} \right) \quad \text{for } I < I_{\text{th}}. \tag{5.15}$$

Above threshold, the carrier density clamps as most injected carriers are immediately converted into photons, which causes the voltage across the diode to clamp, too [25, pp. 70 sq.]. Then, – neglecting thermal effects – U(I) continues to rise linearly:

$$U(I) = IR_s + U_0 \quad \text{for } I > I_{\text{th}}, \tag{5.16}$$

where the device voltage U_0 is a measure for the energy gap of the cladding layers $E_{\text{g, clad}}$ and the bandgap: $E_{\text{g, clad}}/e > U_0 > E_g/e$ [25, p. 73] [51]. From eq. (5.16) follows directly the definition of the series resistance

$$R_s = \frac{\Delta U}{\Delta I} \quad \text{for } I > I_{\text{th}}, \tag{5.17}$$

which expresses the ohmic resistance of the laser diode. Here, I and U are measured quantities and R_s and U_0 are fit parameters. The series resistance is identified as the slope of the linearly extrapolated diode voltage $U(I)$ in the linear regime $1\,\text{A} \gtrsim I \lesssim 3\,\text{A}$ (nearly free of thermal influences). The device voltage $U_0 = U(0\,\text{A})$ is the intersection of that fitting curve with the voltage axis. Since the diodes are mounted in a conduction cooled package (CCP), to which the power supply is connected to, presented values of R_s include a small constant extra resistance. The evaluation of characteristic parameters from the PUI curve is depicted in fig. 5.2.
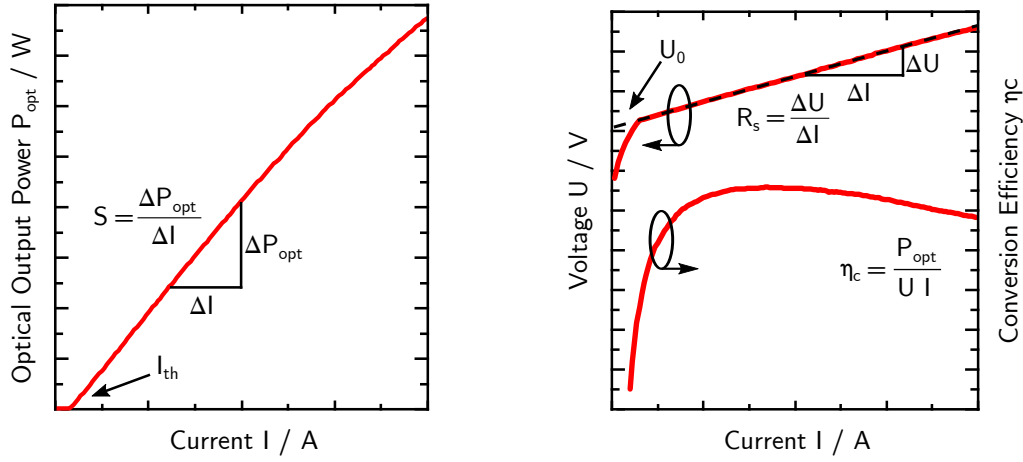
(a) The slope $S = \Delta P_{\mathrm{opt}}/\Delta I$ matches the slope of a linear fit of the optical output power in the linear regime.

(b) The device voltage U_0 is extrapolated from the intersection of a linear fit of the voltage curve $U(I)$ with the voltage-axis in the linear regime – its slope $R_s = \Delta U/\Delta I$ being the series resistance.
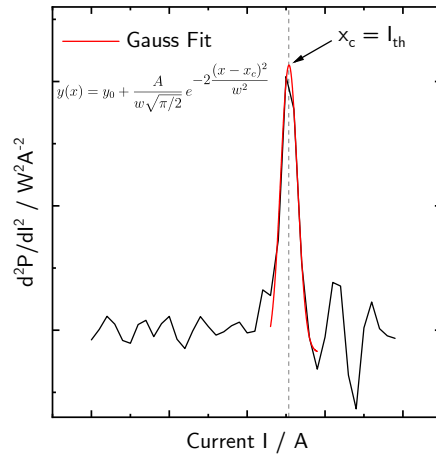
(c) The threshold I_{th} is identified as the center of a Gaussian fit of the maximum of $\mathrm{d}^2 P_{\mathrm{opt}}/\mathrm{d}I^2$.

Figure 5.2.: Identification of characteristic PUI-parameters based on a typical PUI measurement. The linear regime ranges from ca. $1\,\mathrm{A}$ to $3\,\mathrm{A}$ for the avoidance of thermal effects at higher currents.

5.2. Spectral Mapping

As shown in fig. 5.3, an integrating sphere pushed as close as possible without contact to the measuring tower is used for the spectral characterization. An Ulbricht sphere is an integrating sphere used to convert and measure directional radiation into diffuse radiation. It features a nearly ideal diffuse reflecting inner coating (mostly made of sintered PTFE, marketed as *Spectralon* [52]) according to *Beer-Lambert's Law*, at which the laser light entering through an opening is reflected several times. Two theoretical assumptions are made:

1. directional radiation of incident light through the main opening is diffusely scattered on the inner walls
2. residual openings for the detectors (*ports*) are illuminated exclusively by diffusely scattered light.

Therefore, it can be stated that the illuminance on each surface element inside the sphere is the same and thus proportional to the total incident luminous flux. The Ulbricht sphere *integrates* the illuminated surface elements and neutralizes the directional characteristic of the laser radiation. Its ports are connected to an *Ocean Optics HR4000* grating spectrometer for measuring the wavelength-dependent intensity distribution – aka *spectral map* – in the range 890-1050 nm with an attached fiber cable. In addition, neutral density filters can be installed on the port to exploit the full dynamic range of the spectrometer.
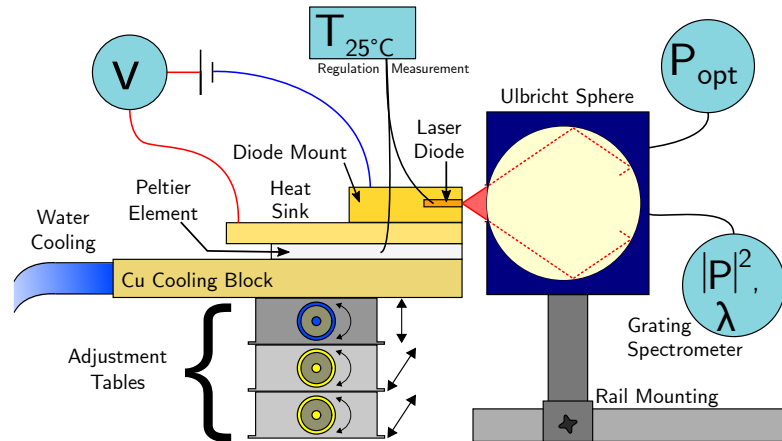

Figure 5.3.: Setup for the recording of spectral maps. The laser light is diffusely scattered many times inside the Ulbricht sphere. By that, its directionality is removed and intensity reduced, allowing to make use of the spectrometer's full dynamic range.
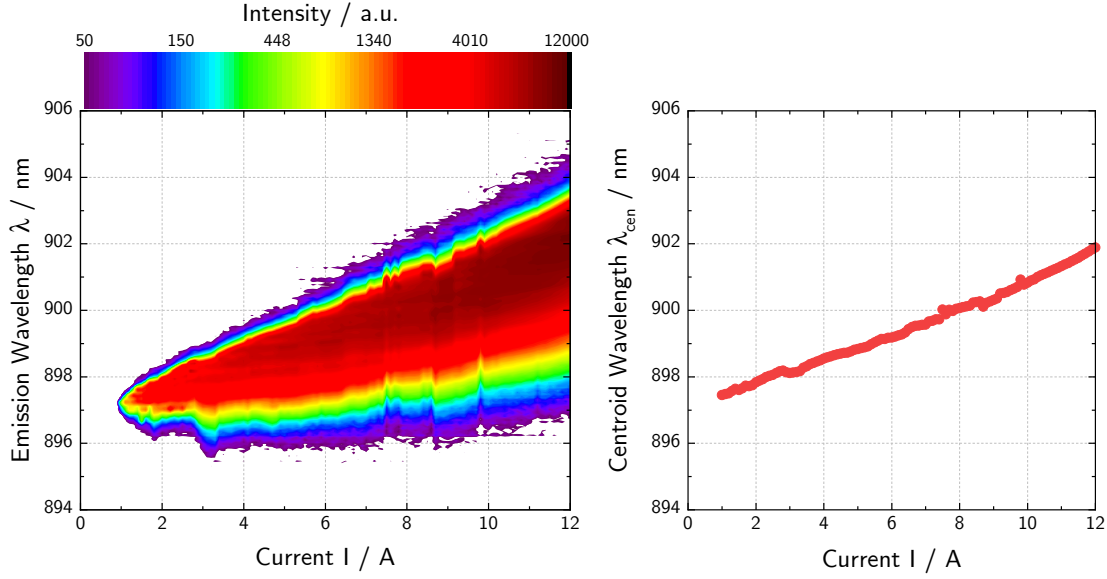
Figure 5.4.: Spectrum and centroid wavelength λ_{cen} of a BCA2900 diode. Its active zone heats up by about $1.2\,\mathrm{K/A}$, which leads to a shift of about $0.38\,\mathrm{nm/K}$. BCA700 designs heat up by about $0.95\,\mathrm{K/A}$, as plotted in fig. 6.5c. Dislocations, e.g. at $7.5\,\mathrm{A}$ or $10\,\mathrm{A}$ indicate mode switching.

Finally, the centroid wavelength λ_{cen} is determined from the spectrometer data after deduction of the electronic noise. For this purpose, the cumulative distribution is calculated by integrating and normalizing the spectral intensity distribution $I(\lambda)$. It is then inverted to compute the inverted cumulative distribution function and evaluated at $\lambda = 50\,\%$ (the median) to reveal the centroid wavelength λ_{cen}. An exemplary spectrum of a BCA2900 diode and its λ_{cen} plot are depicted in fig. 5.4. The intensity maximum of the emission wavelength is driven by the spectral gain maximum (cf. fig. 3.1). Increasing currents cause a thermal expansion of the cavity length L with temperature as well as a rise in the (effective) refractive index n_{eff} (cf. eq. (4.6)), resulting in a different resonator configuration in eq. (2.6). Both effects lead to a Fabry-Pérot wavelength shift for diode lasers of typ. 0.06-$0.2\,\mathrm{nm/K}$ [24, p. 34]. On top of that, the bandgap and hence spectral gain maximum $g(\lambda)$ (cf. fig. 3.1) shift with temperature by typ. $0.33\,\mathrm{nm/K}$ [24, p. 34]. For the presented BCA2900 diode, the active zone temperature rises from $1\,\mathrm{A}$ to $12\,\mathrm{A}$ by about $13.3\,\mathrm{K/11\,A}=1.2\,\mathrm{K/A}$, determined from the calculated AZ temperatures in fig. 6.5c. Compared with its spectrum, the measured centroid wavelength shift in the same range accounts to $(902\,\mathrm{nm} - 897.5\,\mathrm{nm})/(41\,\mathrm{K} - 27.8\,\mathrm{K}) \approx 0.33\,\mathrm{nm/K}$. Opposed to that, BCA700 diodes heat up by about $10.4\,\mathrm{K/11\,A}=0.95\,\mathrm{K/A}$, corresponding to a shift of about $\Delta\lambda_{cen}/\Delta T_{az} \approx 0.28\,\mathrm{nm/K}$.

5.3. Thermal Resistance and Active Zone Temperature

With increasing current, more heat is generated in the active zone, which originates from the growing losses, e.g. via optical absorption or nonradiative recombination. The conduction of the waste heat through the device creates a *thermal resistance* R_{th} between active zone and heat sink. It is defined as the ratio of temperature rise in the active zone $\Delta T_{\text{az}} = T_{\text{az}} - T_{\text{HS}}$ from the heat sink temperature $T_{\text{HS}} = 25\,°\text{C}$ and the thermal power P_{th} of the waste heat [24, pp. 199, 290]:

$$R_{\text{th}} = \frac{\Delta T_{\text{az}}}{P_{\text{th}}} = \frac{\Delta T_{\text{az}}}{UI - P_{opt}} \tag{5.18}$$

where P_{th} equals the difference of electrical input power $P_{el} = UI$ and optical output power P_{opt}. The lasers in this thesis are mounted p-down, for which the waste heat flows from the InGaAs quantum well through the p-doped epitaxial layers to the heat sink. A higher R_{th} or ΔT_{az} mitigates the electrical confinement in the active zone due to the decrease of the bandgap with temperature (Varshni formula [53]), thus flattening the QW (cf. fig. 3.2). Higher temperatures also promote thermally activated processes like leakage currents (over the hetero barriers) or nonradiative recombinations [24, pp. 199 sq.]. These effects result in an increase of the threshold current and a decrease of the external differential efficiency (cf. eq. (5.5)), which can be expressed phenomenologically by Equations (5.11) and (5.12).

The temperature rise of the active zone ΔT_{az} is calculated from the shift of the centroid wavelength with temperature $\Delta \lambda_{\text{cen}}/\Delta T_{\text{az}}$. To accomplish this, eq. (5.18) is rewritten as

$$R_{\text{th}} = \frac{\Delta \lambda_{\text{cen}}(T)}{\Delta P_{\text{th}}} \left(\frac{\Delta \lambda_{\text{cen}}(T)}{\Delta T} \right)^{-1} \Bigg|_{T_{\text{HS}}}. \tag{5.19}$$

First, the centroid wavelength λ_{cen} – known from the evaluation of the spectral map (cf. section 5.2) – is plotted over the thermal power P_{th}, which is known from the PUI measurement (cf. section 5.1). Second, the resulting curve is approximated linearly, with its slope $\lambda_{\text{cen}}(T_{\text{az}})/P_{\text{th}}$ revealing the first factor in eq. (5.19). Unfortunately, due to the natures of measurement, diode behavior (mode switching etc.) and imperfect fabrication, fluctuations occur. For this reason, parts of the $\lambda_{\text{cen}}(P_{\text{th}})$-plot may possess nonlinear curve progressions, which need to be avoided when fitting linearly. The R_{th} derivation from a linear regime is depicted in fig. 5.5. The second factor in eq. (5.19) can be calculated through knowledge of the change of bandgap

with temperature. For this, $E = hc/\lambda$ is differentiated with respect to T and rearranged as follows:

$$\frac{\mathrm{d}E_g}{\mathrm{d}T} = -\frac{hc}{\lambda_{\mathrm{cen}}^2}\frac{\mathrm{d}\lambda_{\mathrm{cen}}}{\mathrm{d}T} \tag{5.20}$$

$$\Longleftrightarrow \frac{\mathrm{d}\lambda_{\mathrm{cen}}}{\mathrm{d}T} = -\frac{\lambda_{\mathrm{cen}}^2}{hc}\frac{\mathrm{d}E_g}{\mathrm{d}T}\bigg|_{T_{\mathrm{HS}}}. \tag{5.21}$$

Anew, a factor remains unknown: the change of bandgap with temperature $\mathrm{d}E_g/\mathrm{d}T$. Its value is of empirical nature (based on the Varshni formula, e.g. [54]), depends on the type of active medium incl. composition factor x and has been investigated by several groups in [55]. Based on these investigations, its value is set to $\mathrm{d}E_g/\mathrm{d}T = -0.5\,\mathrm{meV/K}$ for the $\mathrm{In_{1\text{-}x}Ga_xAs}$ SQW employed in this thesis. This now allows for the computation of eq. (5.21), which can then be inserted into eq. (5.19) to calculate the thermal resistance. At last, the knowledge of R_{th} and thermal power P_{th}, which is deducted from a combination of two separate measurements, allows for the calculation of the active zone's temperature (rise) by rearranging eq. (5.18):

$$\begin{aligned} T_{\mathrm{az}} &= T_{\mathrm{HS}} + R_{\mathrm{th}} \cdot (UI - P_{\mathrm{opt}}) \\ \Longleftrightarrow \Delta T_{\mathrm{az}} &= R_{\mathrm{th}} \cdot (UI - P_{\mathrm{opt}}). \end{aligned} \tag{5.22}$$

The utilization of this equation can be seen in fig. 6.5 in section 6.2.1. In linear regimes, U can be approximated as $U = U_0 + R_s\,I$, which reveals the monotonically dependence of temperature rise on series resistance:

$$\Delta T_{\mathrm{az}} \approx R_{\mathrm{th}} \cdot (U_0 I + R_s I^2 - P_{\mathrm{opt}}). \tag{5.23}$$
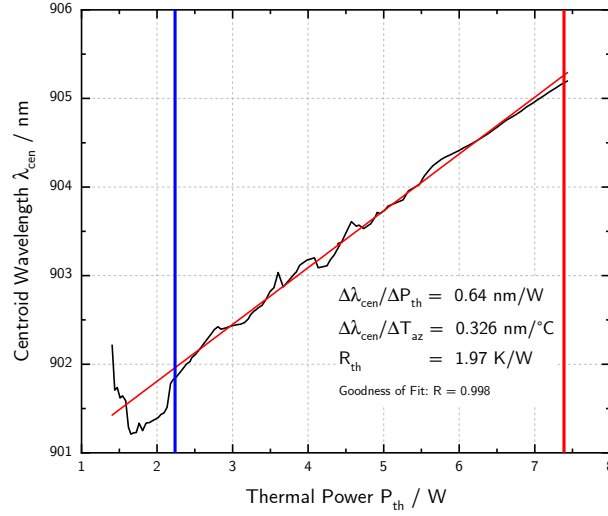
Figure 5.5.: Exemplary determination of the thermal resistance R_{th} from a linear interval enclosed by a blue and a red reference line. The choice of the linear interval allows for the avoidance of thermally-induced nonlinear effects such as mode switching. With knowledge of the thermal resistance, the active zone temperature T_{az} can be calculated.

5.4. Beam Caustics and Beam Quality

The setup for measuring the beam caustics can be seen in fig. 5.6. First, the laser beam is collimated with a lens of focal length $f_1 = 8\,\text{mm}$. It is then attenuated by a cascade of beam attenuators in such a way, that, together with the right combination of neutral-density (ND) filters, the damage thresholds of the photodiode apertures are not reached. The ND filters are located between the telescope lens with $f_2 = 500\,\text{mm}$ and the spherical far-field lens with $f_3 = 400\,\text{mm}$. Combined with the collimating lens, the telescope lens acts as a Kepler telescope and produces a magnified image of the near-field and far-field by the factor $M = f_2/f_1 = 62.5$. The far-field lens is only used for far-field measurements. It (Fourier-)transforms the near-field (Fresnel diffraction) – coming from the infinite by collimation – into the far-field (Fraunhofer diffraction) and images it at a focal length distance of f_3 onto the photodiodes. The second-last component is a beam splitter, which allows the simultaneous observation and adjustment of the image and attenuates the beam by a further $50\,\%$. At the end, two photodiodes are placed on a translation stage behind two apertures of $10\,\mu\text{m}$ and $50\,\mu\text{m}$ width, respectively. The smaller aperture is mostly used for scanning the spatially small far-field of BA lasers and the larger one for the spatially wider near-field. For BA lasers, the near-field width w_{NF} (at the front facet) is identical to the beam waist's width $w(z_0)$ due to a BA laser's
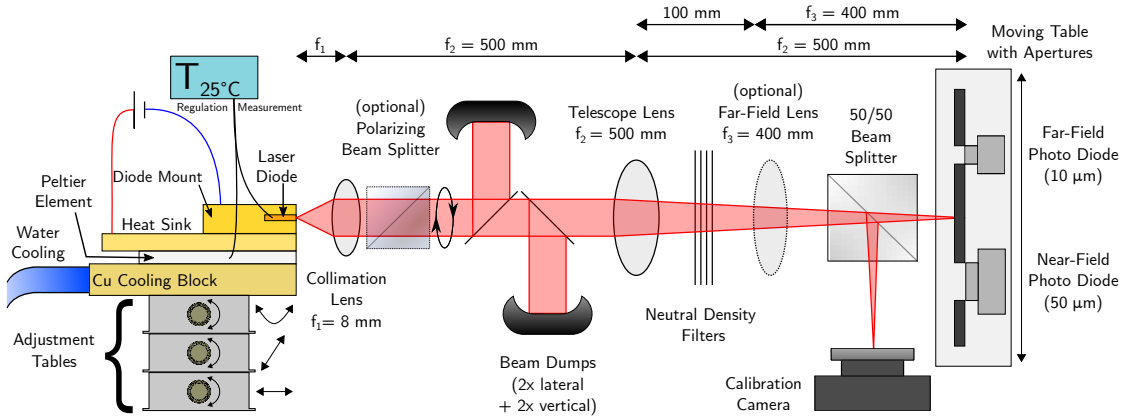
Figure 5.6.: Setup for measuring the near- and far-field distributions of a collimated laser beam. The lateral and vertical beam dumps and neutral density filters weaken the intensity in both polarizations, such that the sensitive photodiodes behind the two apertures are not oversaturated or damaged. A telescope lens magnifies the image 62.5 times, while the (optional) far-field lens transforms the near-field into the far-field. The beam is calibrated and further weakened by a calibration camera and beam splitter. An optional rotatable polarizing beam splitter behind the collimating lens allows for a polarization-resolved measurement.

dimensions. The measurement signal is processed by a *Keithley* multimeter.

True to the Abbe criterion $a \geq \frac{\lambda}{n \sin(\theta)} = \frac{\lambda}{\mathrm{NA}}$, the resolution limit of the near-field width amounts to $a \geq \frac{915\,\mathrm{nm}}{0.5} = 1.83\,\mu\mathrm{m} \approx 2\,\mu\mathrm{m}$. It should be noted that its validity requires illumination with coherent light. With BA lasers, however, the modes are only coherent to themselves and not to each other. In this respect, the Abbe criterion can only represent a rough guide number for the near-field's resolution.

The transformation to the far-field converts the detector position x to the (half) far-field divergence angle:

$$\theta = x \cdot \frac{f_2}{f_1 f_3}. \tag{5.24}$$

This equation follows directly from the transfer matrix method of matrix optics for the far-field setup, after being reduced to its essential components (airway, collimating/telescope/far-field lens) [57, pp. 120 sq.]. It is valid for the paraxial beam approximation $\sin(\theta) \approx \tan(\theta) \approx \theta$. Entering the focal lengths f_1, f_2 and f_3 as well as the far-field aperture width $x = 10\,\mu\mathrm{m}$ into eq. (5.24), the angular
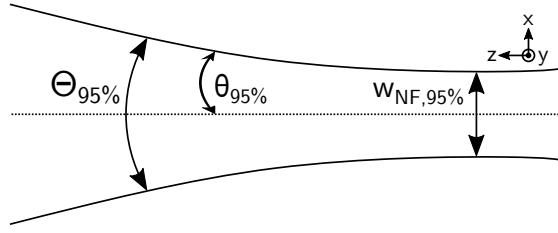
Figure 5.7.: Gaussian beam propagating along the optical axis (z-direction). In all experiments, the near-field width $w_{\mathrm{NF},95\%}$ is detected at the laser's front facet, i.e. at its beam waist position z_0; and the full far-field divergence angle $\Theta = 2\theta$ at a distance much greater than the Rayleigh length $z \gg z_R$, each with 95 % power content.

resolution can be estimated to approximately 0.1°. In a similar fashion, the near-field amplitude is Fourier-transformed at the transition to the far-field. Even so, this aspect shall not be discussed further and instead reference shall be made to the literature [27, pp. 141 sq.].

Ultimately, near-field width w_{NF} and (full) far-field divergence angle Θ unite in the lateral beam parameter product:

$$\mathrm{BPP}_{\mathrm{lat}} = \frac{w_{\mathrm{NF}} \cdot \Theta}{4}. \tag{5.25}$$

Here, the divisor 4 is necessary, because the BPP's definition uses the half near-field width $w_{\mathrm{NF}}/2$ and half far-field divergence angle $\theta = \Theta/2$, as illustrated in fig. 5.7. The $\mathrm{BPP}_{\mathrm{lat}}$ expresses the focusability (colloquially the *quality*) of a laser beam, independent from its wavelength. This is important, since the diode lasers investigated in this thesis will be operated as pump sources for fiber lasers, which demands an efficient coupling to the fiber and hence low $\mathrm{BPP}_{\mathrm{lat}}$. From a physical point of view, it makes sense to determine the widths and divergence angles of the detected near-field and far-field intensity distributions at positions, where their max. intensities I(0) dropped to I(0)/e^2, commonly denoted as $w_{\mathrm{NF},1/e^2}$ and Θ_{1/e^2}. Nevertheless, this thesis follows industry standards, which define the near-field width and far-field divergence angle (and subsequently the $\mathrm{BPP}_{\mathrm{lat}}$) at positions, where 95 % of the beam's power (p.c.) is contained [57, p. 21]. These values are defined by the second momenta of their respective intensity distributions and centered around the first momenta, as explained in detail in DIN EN ISO 11146-1:2005 [58].

A related figure of merit to describe a beam's quality, is the *beam quality factor* M^2 or more precise *beam propagation ratio* [57, p. 22]. The Gaussian beam represents

the idealization of a spherical wave in the paraxial approximation $\sqrt{x^2 + y^2} \ll z$. In practice, though, the shape of an ideal Gaussian beam can only be approached. Therefore, the ratio of the experimentally determined (lateral) beam parameter product $\mathrm{BPP_{exp}}$ and the ideal (lateral) beam parameter product $\mathrm{BPP_{id}}$ compares a real (experimental) beam to the ideal Gaussian beam of wavelength λ:

$$M_{\mathrm{lat}}^2 = \frac{\mathrm{BPP_{exp}}}{\mathrm{BPP_{id}}} = \frac{\mathrm{BPP_{exp}}}{\lambda/\pi} \geq 1. \tag{5.26}$$

Due to the diffraction limit of the Gaussian beam, $\mathrm{M^2_{lat}}$ is always equal or greater than 1. Both, BPP and M² are suited to compare focusabilities or beam qualities of different lasers. Simply spoken, the lower the $\mathrm{BPP_{lat}}$ or $\mathrm{M^2_{lat}}$, the better the beam. In this thesis, the $\mathrm{BPP_{lat}}$ is used as figure of merit for the beam quality.

5.5. Degree of Polarization

The polarization of the radiation is measured with the setup shown in fig. 5.8. First, the emitted laser light is adjusted to the same beam height along the optical axis using an iris aperture. It is then collimated in the vertical and lateral directions using a *fast axis collimator* (FAC) and a *slow axis collimator* (SAC) (two plane-convex cylindrical lenses). The most distant point still visible (approx. $2\,\mathrm{m}$) is focused. Now, a polarizing beam splitter (PBS) and an integrating sphere with connected photodiode are placed in the beam path at the greatest possible distance (approx. $1.50\,\mathrm{m}$), where the beam diverges the least. When the photodiode operates in short-circuit mode (linear proportionality to incident intensity), it generates a small short-circuit current, which is converted into a voltage by a transimpedance amplifier and read by a *Keithley 486 Picoammeter*. The voltage signal can then be assigned to an output power via the spectral responsivity curve of the photodiode – it is, however, sufficient to measure the relative intensity signals as done here. Against this background and for a better comprehensibility, the signal will be referenced as *power signal $P(I)$* from now on. From the reference angle ($\omega_{\mathrm{ref}} = 0°$), the measuring program rotates the PBS by a preset angle in any increments (here: $\omega_{\mathrm{tot}} = 248°$ in $\Delta\omega = 8°$ intervals). The reference angle was defined once by the angle of maximal transmission of a TE-polarized laser through the PBS. The total rotation of the polarizing beam splitter must include both maxima of the selected polarization, i.e. it must rotate by at least 180°). For an ideally adjusted setup without systematic errors, the two maxima lie on the same intensity level.
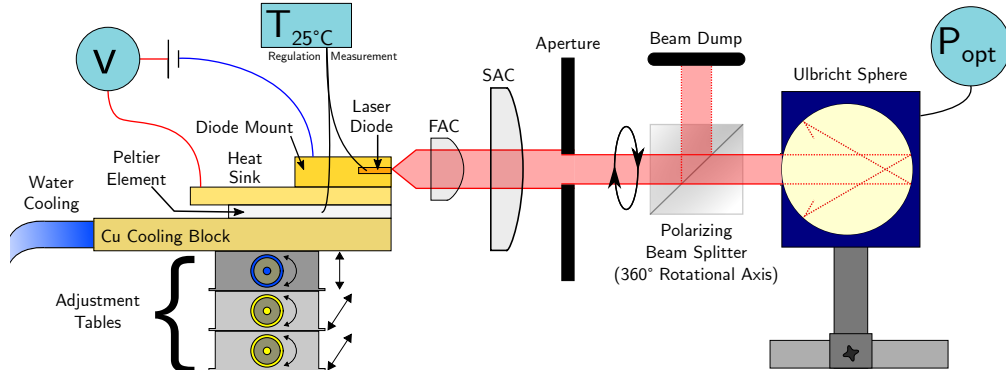
Figure 5.8.: Setup for measuring the degree of polarization. The fast-axis (FAC) and slow-axis (SAC) collimators collimate the laser beam in the vertical y- and lateral x-axis, respectively. Its width is further reduced by an aperture. In this way, a tumbling of the beam when rotating the polarizing beam splitter is prevented, which would also influence the transmitted polarization. The beam's power is measured by a picoammeter, which is connected to a photodiode and the Ulbricht sphere.

The power signal is recorded at every rotation angle ω, such that a positive(!) cosine or sine curve is created (depending on the reference angle, i.e. 0° for TE or −45° for TM). This positive (co-)sine curve is then fitted non-linearly with $A + B\sin^2(C\omega - D)$, as seen in fig. 5.9. The average standard error of the nonlinear fit accounts to about $\Delta_\omega = 3\,\%$ (adapted from [59]). Finally, two degrees of polarization are calculated: the DOP and DOP_{TE}. The equation for the former is:

$$DOP = \frac{|P_{TE} - P_{TM}|}{P_{TE} + P_{TM}}. \tag{5.27}$$

Equation (5.27) is the conventional degree of polarization that equals 1 for an ideal linearly polarized laser. The powers P_{TE} and P_{TM} reflect the maximum and minimum value of the fitted power distribution in fig. 5.9, respectively. Beyond that, professional users are interested in the proportion of polarized light in the total light of the selected polarization, since most high-power BA lasers employ strained quantum wells (cf. section 3.1), emitting close to 100 % polarized light (cf. section 6.3). For this purpose, the DOP_{TE} is defined as follows:
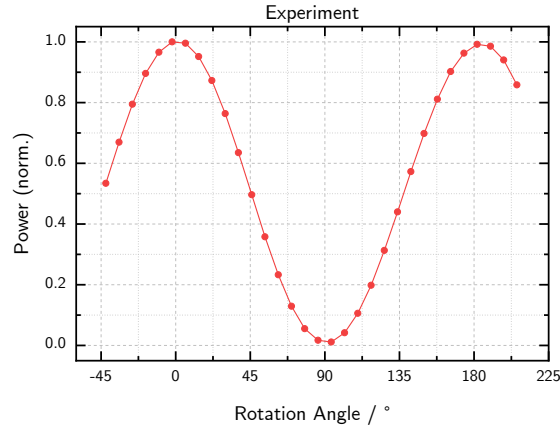
$$DOP_{TE} = \frac{P_{TE}}{P_{TE} + P_{TM}}. \tag{5.28}$$

Figure 5.9.: Typical polarization measurement with a rotation angle increment of $\Delta\omega = 8°$. The maxima and minima are at the rotation angles of highest TE- and TM-transmission, respectively.

In case of TM-polarized light, the numerator of eq. (5.28) equals P_{TM} instead of P_{TE}. Unwanted polarizations are mechanically stress-induced by strains, which are caused by soldering the laser diodes onto the submount, mounting them in their holders or attaching them to the heat sink. One of the goals of the project is to reduce these influences by using a thick sub-contact layer as shown in fig. 3.4. In the polarization analysis in section 6.3, the degree of TE-polarization DOP_{TE} will be utilized as a measure for mechanical stress.

6. Analysis of the Impact of Buried Current Apertures in Experiment and Simulation

In this chapter, results from the experimental characterization of diode lasers with buried current apertures (BCA) ($w_{\text{p-contact}} = 400\,\mu\text{m}$, $w_{\text{BCA}} = 100\,\mu\text{m}$) and without BCA ($w_{\text{p-contact}} = 100\,\mu\text{m}$) for $700\,\text{nm}$ and $2900\,\text{nm}$ thick sub-contact layers at a heat sink temperature of $T_{\text{HS}} = 25\,^\circ\text{C}$ will be presented and evaluated. The designs will be abbreviated as BCA700, ref700, BCA2900 and ref2900, where the three letters indicate the implantation (buried current aperture or none=reference) and the number the thickness of the sub-contact layer ($700\,\text{nm}$ or $2900\,\text{nm}$). For the sake of readability and better discussions only data of the "best" diodes will be depicted in measurement plots. These "best" diodes are selected in view of maximal output power, slope and linearity of the P-I-curve and will be kept the same throughout the remainder of the thesis.

Characteristic parameters like slope S or threshold I_{th} will be derived from the measurements, averaged between the specimens of each design and displayed in tables along with their standard deviations (SD) according to GUM 7.2 [60, p. 25]. Standard deviations will be rounded up to one significant digit. Systematic uncertainties due to the measurement devices will be provided along the results. There are three specimen of ref700, BCA2900 and ref2900 each, and six specimen of BCA700. The author is aware of the low sample size of three specimens for the first three designs, resulting in a high student's t-factor of $t = 1.32$ (student's t-distributions, not Gaussian) for the respective standard deviations ($p = 0.683$) of ref700, BCA2900 and ref2900 ($t = 1.11$ for BCA700) [60]. However, the focus of this thesis lies on the properties of the buried current aperture structures. To assure a similar presentation style between all results (without cherry-picking) and to characterize derived parameter ranges, it has been chosen to calculate and demonstrate the mean and standard deviation of every design.

All simulations, e.g. carrier density or refractive index distribution, beam caustic (near-field, far-field) and polarization measurements have been conducted at seven

current operating points: $I_{th}+50\,\text{mA}$ ("close above threshold"), $2\,\text{A}$, $3.5\,\text{A}$, $5\,\text{A}$, $7.5\,\text{A}$, $10\,\text{A}$ and $12\,\text{A}$. Therefore, current-dependent parameter changes can be tracked in high detail. In the experiment, current I is provided by a constant-current supply, while the simulations run in dependence on the diode voltage U. The operating points differ marginally from the experimental points due to a compromise between computation and evaluation time.

Here, an appointment has to be made: since the author didn't conduct the simulations himself, certain fit parameters have not been adapted in full extent to the experiment. The most important are the Shock-Read-Hall recombination coefficient A as in eq. (4.14), which contributes (slightly) to the laser threshold via the rate of deep level recombinations as in eq. (5.9) [24, pp. 41–43]; the eff. background absorption coefficient $\alpha_{0,\text{eff}}$ due to FCA, which governs the threshold, external differential quantum efficiency and slope as in eq. (5.5); and the inverse heat transfer coefficient r_{th}, which directs the laser's mean temperature as in the boundary conditions for the heat flow at the end of section 4.3.2. As a consequence, the simulated PUI curves as well as other parameters such as near and far-field widths differ quantitatively from the experimental results, e.g. in threshold, slope, facet and bulk temperatures and field intensities. However, relative deviations between BCA and reference stay the same and can therefore be used for comparison with the experiments.

6.1. Power-Voltage-Current (PUI) Parameters

Figure 6.1a shows the diode voltages U and the optical output powers P_{opt} of the best diodes with and without buried current aperture for thin (700 nm) and thick (2900 nm) sub-contact layers. Below threshold, the current I of a diode rises exponentially according to the Shockley diode eq. (5.15). Hence, the applied forward voltage $U(I)$ rises logarithmically with current, until the laser reaches its threshold $U(I_{th})$. Above threshold $I > I_{th}$, the carrier density clamps because of the fast stimulated recombination rates. By that, the voltage $U(I)$ and optical output power $P_{\text{opt}}(I)$ continue to rise linearly (cf. eq. (5.16)). Especially for currents greater than $5\,\text{A}$ kinks in the PUI curves occur, which are also visible in the voltage curves. These develop due to nonlinear opto-electronic and thermal effects, e.g. dynamic changes of the refractive indices caused by nonuniform local carrier densities and temperatures (cf. eq. (4.4)), which favor higher-order lateral TE modes with different power distributions [25, pp. 37 sq.]. Kinks are often identifiable as shifts in the spectrum, since other modes (longitudinal and lateral) experience other effective indices n_{eff} (Fabry-Pérot shifts) and centroid wavelengths
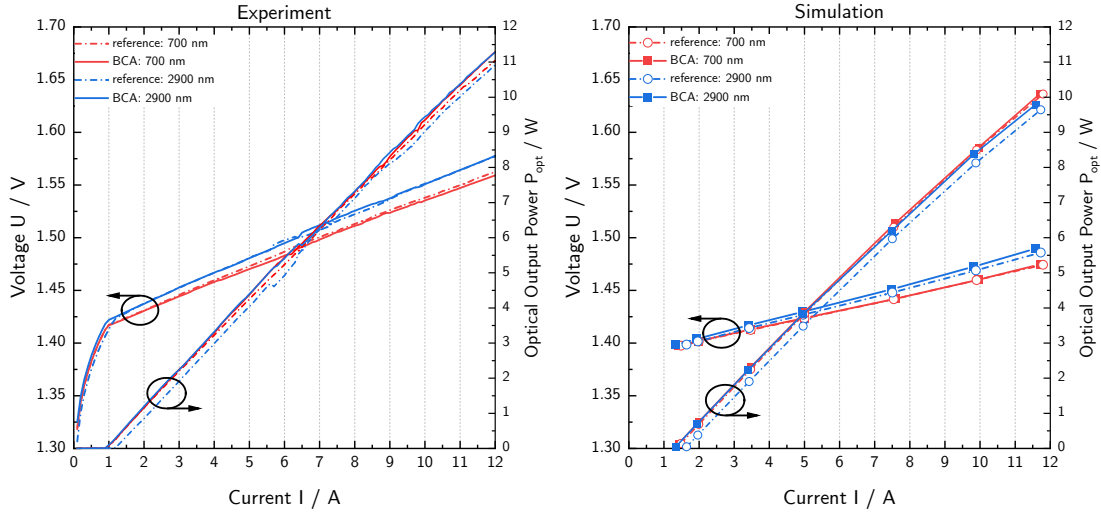
(a) Experiment with 120 current steps

(b) Simulation with 7 data points resembling the experimental working points

Figure 6.1.: Experimental and simulated PUI curves of the (in experiment best) diodes with (BCA, solid) and without (reference, dash-dotted) buried current aperture for 700 nm (red) and 2900 nm (blue) thick sub-contact layers at 25 °C and 300 K, respectively.

λ_{cen} (cf. fig. 5.4). Additionally, raising the former argumentation from behind, by affecting the carrier distribution kinks are also visible in the U(I) curves [25, p. 71]. At high currents, the voltage and power curves bend downwards (here: slightly), because of the laser's temperature rise with increasing Joule heating and optical absorption losses. This is connected to a rise in threshold via eq. (5.11) and reduces the slope, too (cf. eq. (5.12)). Table 6.1 contains the characteristic electro-optical parameters, which are averaged from the individual results of the diode evaluation, with their standard deviations (SD) in brackets and deviations Δ_{ref}^{BCA} of BCA to reference designs. In the following, parameter changes will be discussed in terms of these deviations for each sub-contact layer thickness.

First, the reduction of the threshold from ref700's 960(3) mA by 9 mA to BCA700's 951(9) mA is not significant as it lies within the SD interval. This contrasts the 2900 nm design with its threshold reduction by 20 % to 949(11) mA, which equals BCA700's threshold (within the SD). Still, the slopes and max. output power of both BCA structures each increase by 40 mW A^{-1} (3-4 %) and 300 mW (2-3 %), respectively. However, the systematic power measurement uncertainty of ±3 % dilutes these differences in uncertainty. Moreover, due to the high standard deviation of ref700, the BCA implantation does not significantly reduce the series

Table 6.1.: Extrapolated mean characteristic parameters of the best diodes from experiment, and deviations of BCA to reference design $\Delta_{\text{ref}}^{\text{BCA}}$. The slope S and series resistance R_s have been calculated from linear regressions (least squares) in the interval 1.1-3 A of the P(I) and U(I) curves, respectively, except for the 1.3-3.2 A interval of the ref2900 diodes due to their higher thresholds. The threshold I_{th} has been identified from a Gaussian fit of the local maximum of $\mathrm{d}^2 P_{\text{opt}}/\mathrm{dI}^2$. The uncertainties in brackets are the standard deviations from averaging the specimens' results (P_{opt}, I_{th}) or the standard errors from the linear progression (S, R_s). Systematic measurement uncertainties amount to $\pm 3\,\%$ for power P_{opt} and $\pm 0.004\,\%$ for voltage U.

Design	I_{th}/mA	$\Delta_{\text{ref}}^{\text{BCA}}$	$S/\text{W A}^{-1}$	$\Delta_{\text{ref}}^{\text{BCA}}$	$P_{\text{opt}}(12\,\text{A})/\text{W}$	$\Delta_{\text{ref}}^{\text{BCA}}$	$R_s/\text{m}\Omega$	$\Delta_{\text{ref}}^{\text{BCA}}$
ref700	960(3)	$-1\,\%$	1.05(1)	$3\,\%$	11.0(1)	$2\,\%$	14.6(4)	$-5\,\%$
BCA700	951(9)		1.09(1)		11.3(1)		13.8(1)	
ref2900	1193(16)	$-20\,\%$	1.05(1)	$4\,\%$	10.9(1)	$3\,\%$	15.6(1)	$-2\,\%$
BCA2900	949(11)		1.09(1)		11.2(1)		15.2(1)	

resistance of the 700 nm design (ref700: 14.6(4) mΩ vs. BCA700: 13.8(1) mΩ). Although, it does barely significantly reduce R_s of the 2900 nm structure by 2 % from 15.6(1) mΩ to 15.2(1) mΩ. Owing to the thicker diode design, there is also a significant difference of $\Delta R_s = 9\,\%$ between BCA700 and BCA2900. In short, the buried current aperture has the tendency to reduce the laser's threshold and series resistance, while increasing its slope and maximum output power, but the experimental results' significances are mostly too low to *safely* validate any positive effect on the electro-optical parameters. Now, the experimental PUI curves and parameters will be compared with their simulated analogs. Please keep in mind, that the simulations haven't been adapted to the experiment.

Figure 6.1b shows the simulated PUI curves of four lasers, which are similarly designed to the experimental BCA (solid) and reference (dash-dotted) diodes with 700 nm (red) and 2900 nm (blue) thick sub-contact layers. As can be seen, the simulated P(I) curves of the 700 nm designs run parallel to each other. For the experimental BCA700 and ref700 specimens in fig. 6.1a, this holds only true for small currents until about 3 A. It does so, too, for regions around kinks, e.g. from 6.5 A to 9 A. The BCA2900 design also runs parallel to the 700 nm diodes, despite from a marginal deviation towards 12 A. As with the experiment, the simulated ref2900 design has a significantly greater threshold, so its P(I) curve runs with a current-offset parallel to the other simulated P(I) curves. The simulated 700 nm voltage curves are nearly indistinguishable, which also holds for the experimental

Table 6.2.: Extrapolated characteristic parameters from simulation and deviations of BCA to reference design $\Delta_{\mathrm{ref}}^{\mathrm{BCA}}$ for each parameter. The slope S, threshold I_{th} and series resistance R_s have been calculated from linear regressions (least squares) of the first three simulation points (about 1-3.5 A) of the P(I) and U(I) curves, respectively. The uncertainties in brackets are the standard errors of the linear regression (rounded up).

Design	I_{th}/mA	$\Delta_{\mathrm{ref}}^{\mathrm{BCA}}$	S/W A^{-1}	$\Delta_{\mathrm{ref}}^{\mathrm{BCA}}$	$P_{\mathrm{opt}}(12\,\mathrm{A})$/W	$\Delta_{\mathrm{ref}}^{\mathrm{BCA}}$	R_s/mΩ	$\Delta_{\mathrm{ref}}^{\mathrm{BCA}}$
ref700	1349(1)		1.06(1)		10.4(1)		7.3(1)	
BCA700	1283(1)	$-5\,\%$	1.06(1)	$0\,\%$	10.4(1)	$0\,\%$	7.3(1)	$0\,\%$
ref2900	1600(1)		1.04(1)		10.0(1)		8.5(1)	
BCA2900	1287(1)	$-20\,\%$	1.06(1)	$2\,\%$	10.3(1)	$3\,\%$	8.6(1)	$1\,\%$

2900 nm U(I) curves, whereas the experimental ref700 U(I) curve grows a little bit steeper than its exp. BCA700 counterpart.

To quantify these relationships better, the characteristic parameters are extrapolated from the simulated PUI curves. This is done with a linear regression in case of threshold, slope, and series resistance; and with a non-linearly fit in case of maximum output power to account for thermal effects. The simulated parameters are presented in table 6.2, together with the deviations $\Delta_{\mathrm{ref}}^{\mathrm{BCA}}$ of BCA to reference designs. When comparing the simulation's $\Delta_{\mathrm{ref}}^{\mathrm{BCA}}$ with those of the experiment, they differ at most by 5 p.p. (percentage points), that is to say $\Delta_{\mathrm{exp}}^{700}R_s = -5\,\%$ vs. $\Delta_{\mathrm{sim}}^{700}R_s = 0\,\%$; while being identical (rounded) at best, e.g. $\Delta_{\mathrm{exp}}^{2900}I_{\mathrm{th}} = \Delta_{\mathrm{sim}}^{2900}I_{\mathrm{th}} = -20\,\%$. In general, these deviation differences between experiment and simulation are smaller for 2900 nm designs than for 700 nm. Concerning the trends from BCA to reference between experiment and simulation, the following aspects can be stated:

1. the simulation of ref700/BCA700 overestimates the threshold reduction by 4 p.p. while completely neglecting any changes in slope (+3 p.p.), max. output power (+2 p.p.) and series resistance (-5 p.p.)

2. the simulation of ref2900/BCA2900 predicts the deviations in threshold and max. output power correctly (0 p.p.), underestimates the increase in slope by +2 p.p. and even prognosticates a slight increase of series resistance by 1 % instead of decrease by $-2\,\%$ as in the experiment.

To this point, the impact of buried current apertures on the experimental and simulated electrical parameters has been analyzed. With the help of simulations of the spreading current, time-averaged lateral carrier density and gain, the underlying reasons for the observed behavior will be investigated.
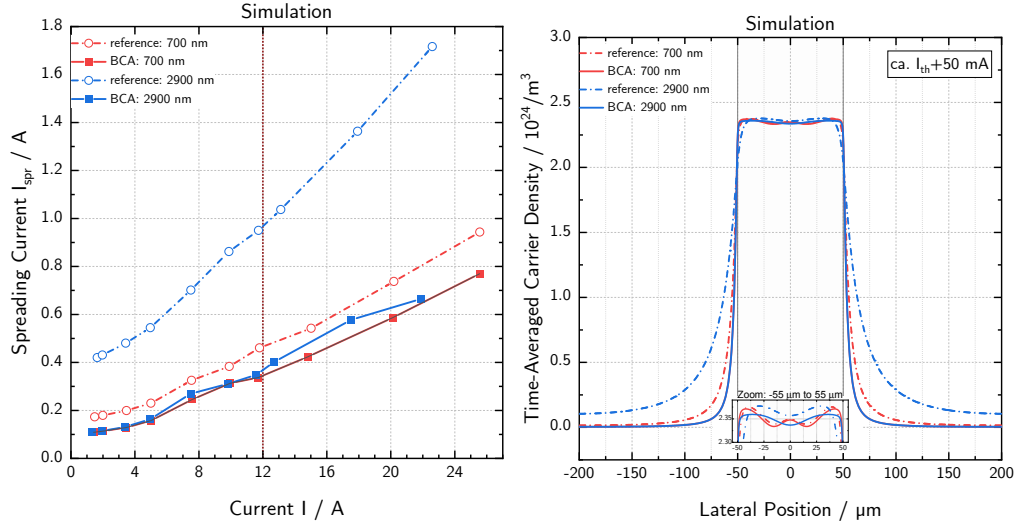
(a) Absolute spreading currents I_{spr} being the sum of all currents inside the active zone beyond $x = \pm 50 \,\mu m$ (BCA and reference).

(b) Time-averaged lateral carrier densities $50 \,mA$ above threshold I_{th}. The inset shows an enlarged view of the active zone.
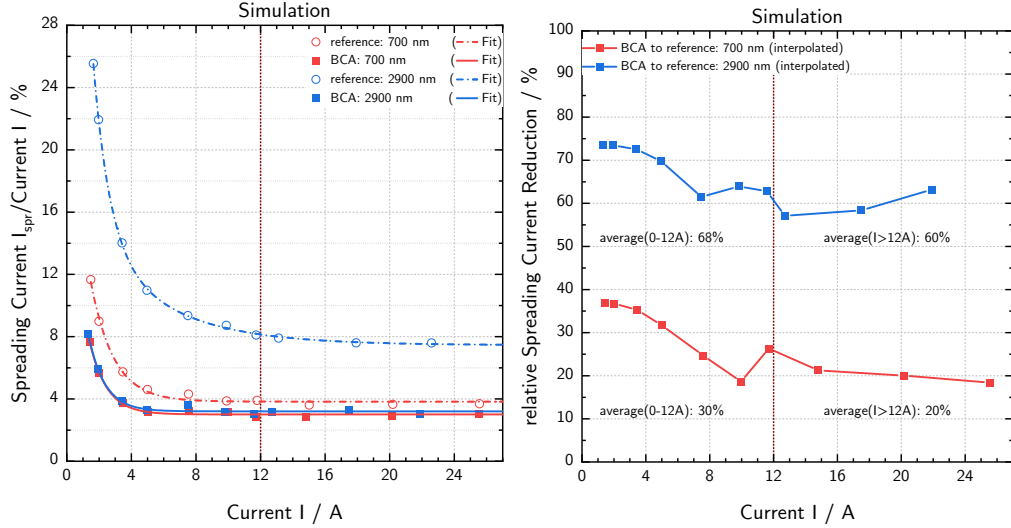
(c) Relative spreading current, i.e. fraction of I_{spr} to injected current I. Fit parameters are given in table 6.3.

(d) Relative reduction of (interpolated) spreading currents from reference to BCA designs.

Figure 6.2.: Simulations of spreading currents and time-averaged lateral carrier densities of diodes with (BCA, solid) and without (reference, dash-dotted) buried current aperture for $700 \,nm$ (red) and $2900 \,nm$ (blue) thick sub-contact layers at $300 \,K$. Vertical dotted lines indicate the max. current in experiment.

6.1.1. Threshold Current

By definition, spreading currents are the sum of all currents outside the BCA width (or p-contact width in case of reference designs) being injected into the active zone. They rise monotonically with the threshold current I_{th} and p-contact width (cf. eq. (4.17)). In fig. 6.2b the lateral distribution of the carrier density is shown (time-averaged from three 5 ns long simulation intervals). It proves the reduction of current spread in the lateral outer-regions ($|x| > 50\,\mu\text{m}$) of the quantum well thanks to the buried current apertures. Inside the active zone $|x| \leq 50\,\mu\text{m}$ all designs fluctuate to some extent (see inset). Both BCA700 and BCA2900 designs stretch the carrier density (CD) to the AZ's edges, such that BCA2900's curve flattens as opposed to BCA700. The proportion of current "loss" by current spreading is depicted in fig. 6.2a. Already close above threshold I_{th}+50 mA, BCA700 reduces the spreading current by $\Delta I_{\text{spr}} = 65\,\text{mA}$ ($-37\,\%$) and the BCA2900 by $\Delta I_{\text{spr}} = 311\,\text{mA}$ ($-74\,\%$) to an equal level of 109 mA, independent from the sub-contact layer thickness. Apart from small rounding errors, these decreases in spreading currents match exactly the differences in the simulated threshold currents of 66 mA (BCA700 to ref700) and 313 mA (BCA2900 to ref2900) in table 6.2.

Consequently, the reduction in simulated threshold I_{th} can be fully attributed to the reduction of current spread I_{spr} by the buried current apertures. This is obviously true for the thick BCA2900 design, where simulation and experiment coincide with $\Delta I_{\text{th}} = -20\,\%$, but not for the thin BCA700 design with a 4 p.p. difference from simulation $\Delta^{700}_{\text{sim}}I_{\text{th}}$ to experiment $\Delta^{700}_{\text{exp}}I_{\text{th}}$. Based on the simulation results, this implies a higher "intrinsic BCA efficiency" in terms of threshold reduction for the thicker 2900 nm than for the thinner 700 nm design.[1]

The reasons can only be speculated. Owing to the smaller distance of the p-contact layer to the quantum well for the 700 nm design, the current spread and hence threshold reduction might be overrated by the software tool *BALaser*. The (effective) BCA width of the fabricated BCA700 diodes could also be slightly larger than 100 µm or the implantation could be not as steep as it should, therefore resulting in a greater current spread. Lastly, as *BALaser* simulates lasers only above threshold, the latter have been linearly extrapolated from the P(I) curve, but not via second derivation of the output power with respect to current $\mathrm{d}^2 P_{\text{opt}}/\mathrm{dI}^2$ as for the fabricated designs. The corresponding simulation thresholds might thus lie

---

[1]Attention: Do not confuse this with the efficiency of the reduction in current spread, which is obviously greater for BCA2900 than for BCA700 due to the much higher spread of the hole current on its path through the thick sub-contact layer to the AZ. Here, we are solely analyzing the relative threshold current deviations $\Delta^{\text{BCA}}_{\text{ref}}I_{\text{th}}$ between simulation and experiment. The thresholds of BCA700 and ref700 deviate stronger from each other in the experiment than predicted by the simulation – this is not the case for BCA2900 and ref2900.

a bit below the values presented in table 6.2, as the linearly extrapolated thresholds are usually smaller than with the second derivation method (in the absence of kinks or saturating effects, which have been taken into account when determining the experimental thresholds). This is because the linear method takes both spontaneous and stimulated emission above threshold into account, whereas the 2nd-derivation method identifies the onset of stimulated emission [24, p. 43]. Then, the $\Delta_{\mathrm{ref}}^{\mathrm{BCA}}$ differences between simulation and experiment would shrink for both designs; while the thick 2900 nm diodes might "compensate" this reduction due to their higher standard deviations of up to 16 mA.

6.1.2. Series Resistance

The series resistance R_s depends on the current spread in the p-layers as described in section 4.2. The injection current into the active zone $I = I_{\mathrm{stripe}} + I_{\mathrm{spr}}$ composes of the stripe current I_{stripe}, which flows vertically below the p-contact and the spreading current I_{spr} outside the BCA width (similar width for references). The sum itself stays constant, but the higher the spreading current's strength, the wider the current spread. In theory, a smaller spreading current decreases the cross-sectional area A of vertical current flow and thereby raises series resistance $R_s \propto 1/A$. Unfortunately, *BALaser* is not able to output the current distribution above the active zone in order to assess the current-carrying cross-sectional area A and by that the spreading current. As such, the change in series resistance can not be traced back quantitatively to corresponding changes of simulated or measured parameters in p-regions above the quantum well and will only be evaluated qualitatively in the following. Additionally, this hinders the calculation of specific resistances per layer, which would have allowed for a better comparability of BCA and reference designs in view of the different p-contact widths ($w_{\mathrm{p\text{-}contact}}^{\mathrm{BCA}} = 400\,\mu\mathrm{m}$ vs. $w_{\mathrm{p\text{-}contact}}^{\mathrm{ref}} = 100\,\mu\mathrm{m}$).

In fig. 6.2c the fraction of spreading current to injected current, i.e. the relative reduction of spreading current per injected current I_{spr}/I, is plotted. All values demonstrate decaying progressions, approximating constant values until 12 A, except ref2900. Therefore, three operating points above 12 A up to roughly 25 A have been simulated, added and fitted together with the other points with exponentially-decaying functions. The fit formulas and parameters are listed in table 6.3. At high currents, all curves approximate constant values ("y_0") which have been derived from the fits as the y-axis-intersection for an infinite current. The BCA700 and BCA2900 diodes both converge from about 8 % relative spreading current close above threshold to 3.0(1) % and 3.2(1) % at 12 A, respectively. Surprisingly, the blue dash-dotted ref2900 curve can not be fitted properly with a single-, but a

Table 6.3.: Fit parameters of the exponentially decaying fits in fig. 6.2c. The uncertainties in brackets are the standard errors of the exponential regression.

Design	BCA700	ref700	BCA2900	ref2900
Equation	$y(x) = A_1 \cdot exp(-x/\tau_1) + A_2 \cdot exp(-x/\tau_2) + y_0$			
y_0	3.01(5)	3.83(9)	3.20(7)	7.5(2)
A_1	18(2)	22(2)	18(3)	57(5)
τ_1	1.07(8)	1.4(2)	1.0(1)	1.0(2)
A_2	0	0	0	9(2)
τ_2	-	-	-	4.6(8)

double-exponentially decaying function. This indicates the influence of physical effects on the spreading current of ref2900 designs, which the other structures do not experience. In fact, ref2900 approximates a relative spreading current of $y_0 = 7.5(2)\,\%$, which is nearly double the amount of ref700 with $y_0 \approx 3.8(1)\,\%$.

To estimate the impact of the BCA implantation into reference structures (apart from the p-contact width change), the relative reduction of spreading current from reference to BCA, i.e. $\frac{I_{spr,ref} - I_{spr,BCA}}{I_{spr,ref}}$ has been calculated. But before applying the math on the simulation values in fig. 6.2a, all spreading currents I_{spr} needed to be interpolated to the same x-basis in order to divide BCA and reference values at the exact same currents. To assure the least possible error, the sum of stripe and spreading current per sub-contact thickness has been taken as x-basis for the XY spline interpolation algorithm instead of the experimental operating points. Above 12 A, ref2900 gains an increasing x-offset to BCA2900 of up to 0.6 A at about 22 A, whereas no such increase is visible for the 700 nm designs. Apart from this particular range, all other spreading currents possess small x-offsets of 0.15 A at max. After interpolation, the above formula could be applied, with the results being depicted in fig. 6.2d. On average, the BCA reduces the spreading current compared to its reference in the range 0-12 A by 30 % for the 700 nm and by 68 % for the 2900 nm design. Nevertheless, concerning series resistance, the first three simulation points are of higher importance, since these represent the linear regime for the derivation of several characteristic parameters. The values at these points are nearly equal, making up for a relative I_{spr} reduction by 36 % for 700 nm and by 73 % for 2900 nm. Despite the latter being twice as big as the former, BCA2900's simulated series resistance of $R_s = 8.6(1)\,\text{m}\Omega$ does not significantly differ from its reference value $R_s = 8.5(1)\,\text{m}\Omega$, which holds also true for the 700 nm structure ($R_s = 8.5(1)\,\text{m}\Omega$ for both). In contrast, the series resistance reductions in the experiment account to $-5\,\%$ and $-2\,\%$ with respect to 700 nm and 2900 nm.

Nevertheless, as already stated, these reductions have no or bare significance. As a consequence, three possibilities emerge:

1. The reduction in spreading current reduces the experimentally observed series resistance of the BCA design compared to its reference. However, the electro-optical model employed in *BALaser* does not cover this R_s reduction.

2. Compared with the references, the BCA design does not change the series resistance within the measurement uncertainty. A possible decrease of R_s by the enlarged p-contact-width $w_{\text{p-contact}}^{\text{BCA}} = 400\,\mu\text{m}$ of the BCA designs might be countered by an increase of R_s due to decreasing current spread width w_{spr} (ideally down to $w_{\text{BCA}} = 100\,\mu\text{m}$). As such, the *effective* BCA width $w_{\text{BCA,eff}}$ would be smaller (higher R_s) in the experiment than in the simulation.

3. The BCA structure reduces the spreading current width $w_{\text{spr}}(I_{\text{spr}})$ *and* the series resistance, at the same time. This could be due to a significant increase in device temperature even at lower currents (cf. fig. 6.5), which fundamentally reduces a semiconductor's (series) resistance.

In any case, further measurements are needed to increase the results' significances in order to reveal the true influences and underlying reasons of the BCA design on the series resistance.

6.1.3. Slope and Maximum Output Power

Obeying the simple laser model outlined in section 5.1, slope S is defined by eq. (5.5) and optical output power P_{opt} by eq. (5.3). Therewith, P_{opt} is proportional to S and rises monotonically with decreasing threshold I_{th}. The slope itself depends on the photon energy $h\nu = hc/\lambda$ and the external differential quantum efficiency η_{ext}, which comprises of the internal efficiency η_{int}, the mirror losses α_{mir} and the internal losses α_{int}. The latter three quantities are governed by the laser device design and the emitting wavelength λ by the maximum of the spectral gain. In turn, the eff. gain g_{eff} depends logarithmically on the carrier density N as in eq. (4.7). Lastly, the threshold current I_{th} depends on the threshold carrier density N_{th} (cf. eqs. (5.6) to (5.9)). In section 6.1.1, the reduction of I_{th} and the subsequent increase of $P_{\text{opt}}(12\,\text{A})$ has already been discussed, i.e. lower eff. gain leads to higher thresholds and lower output powers. Furthermore, the significances of $P_{\text{opt}}(12\,\text{A})$ and $S = \Delta P_{\text{opt}}/\Delta I$ (derived from the linear regime) in table 6.1 are too low, since they're subject to the systematic power measurement uncertainty of $\pm 3\,\%$. Thereby, a few factors influencing S and consequently $P_{\text{opt}}(12\,\text{A})$ remain, which will be discussed in a qualitative manner in the following.

First of all, the active zone temperature T_{az} regulates the external diff. quantum efficiency η_{ext}. Rauch et al. [61] show that for quasi-continuous wave (QCW) operation, η_{ext} can degrade by about 30 % with a temperature rise of $\Delta T_{\text{az}} = 15\,\text{K}$. It is trivial to assume, that this degradation is even worse for CW-operated devices. Forestalling the influence of measured mean AZ temperature rise ΔT_{az} in fig. 6.5c, the BCA700 diodes heat from threshold to 12 A by about 11 K and the BCA2900 diodes by about 13 K, which translates to about 20-30 % degradation of the ext. diff. quantum efficiency and thus slope (over the full current range). Here, the ΔT_{az} curve of the ref700 design runs parallel to the BCA2900 curve, while ref2900 heats up on average by about the same as BCA2900. Thus, it could be assumed that the slopes of the 2900 nm structures are smaller in the vicinity of 12 A than for 700 nm. Yet, maximum output powers of the BCA designs 10.3(1)-10.4(1) W are equal within their standard deviations. This indicates, that the degradation of ext. quantum efficiency with active zone temperature rise is *not* a driving force behind slope and maximum output power – at least not for the 2900 nm designs.

As sketched above, the distribution of carrier density N or effective gain g_{eff} can affect the slope, too. Of particular interest are phenomenons, which decrease the rate of stimulated radiative recombinations and by that the external diff. quantum efficiency η_{ext} (and slope) as examined in [62]. One such phenomenon is the lateral carrier accumulation (LCA) [57, pp. 75 sq.]. Naturally, the threshold carrier density N_{th} is reached first in the laterally centered region below the injection stripe (p-contact), where it amplifies the fundamental mode. With increasing current, this region expands to (nearly) the whole stripe width $w_{\text{p-contact}}$, providing higher-order modes with gain. But the thermal lens, that builds up with current and temperature (investigated in section 6.2), constrains the already-existent TE modes into the center region. This way, stimulated recombination in the lateral outer-regions decreases, while carrier density increases, as these carriers won't be depleted by the existing modes of the optical field. This is, until the gain in the edge region is high enough to amplify the next higher-order TE mode, degrading the lateral beam parameter product as well as slope and output power via the creation of kinks. Additionally, high LCA corresponds to high carrier density gradients near the edges, resulting in increased carrier diffusion into the lateral outer-regions and reduced internal quantum efficiency. Therefore, different LCA gains between different laser designs can account for differences in slope and optical output power.

As the slope S has been determined in the linear regime from about 1 A to 3 A and the maximum output power at 12 A, it makes sense to investigate the lateral optical gain profiles at the first three ($I_{\text{th}}+50\,\text{mA}$, 2 A, 3.5 A) and the last operating point (12 A). These profiles are depicted in fig. 6.3, where every subfigure contains a zoomed inset of the active zone ($|x| \leq 50\,\mu\text{m}$), shown from $-55\,\mu\text{m}$ to $55\,\mu\text{m}$ for

a better visualization of the lateral carrier accumulation.[2]

From the first three gain profiles follows, that outside the active zone no noteworthy change in gain takes place between figs. 6.3a to 6.3c. In each profile, the gains of both BCA designs start symmetrically from the outermost lateral simulation point $x = \pm 200 \, \mu m$ at roughly $g_{eff} = -4200 \, m^{-1}$ (loss), having been reduced from the reference values of $-3300 \, m^{-1}$ and $-1900 \, m^{-1}$ for BCA700 and BCA2900, respectively. As expected, the BCAs increase the optical losses (negative gain) in the lateral outer-regions due to the local reduction of carrier density N. Close above threshold, LCA is not distinguishable, yet. It becomes first clearly visible at 2 A, where all designs build side lobes near the edges $x = \pm 50 \, \mu m$. At this current, the gains of both BCA peak at $410 \, m^{-1}$, while reaching their maximum at $470 \, m^{-1}$ at 3.5 A. Then, inside the active zone $|x| \leq 50 \, \mu m$ all designs portrayed in figs. 6.3a to 6.3c drop to a mean gain level of about $370 \, m^{-1}$ due to the carrier clamping above threshold. The amount of this drop Δg_{eff} can be used as a measure for the LCA gain in reference to the center region of the active zone. In fact, BCA700 and BCA2900 accumulate 25 % and 50 % more gain at the device edges at 2 A than their respective references. These numbers change at 3.5 A to 22 % for BCA700 and 122 % for BCA2900. Finally, at 12 A, the gain profile has lost its symmetry and the plateau inside the AZ rises to about $430 \, m^{-1}$. On the left side, BCA700's gain drops by 20 % more than its reference ($\Delta g_{eff}^{BCA} = 190 \, m^{-1}$ vs. $\Delta g_{eff}^{ref} = 150 \, m^{-1}$) and on the right side nearly 450 % more than its reference at the same location ($220 \, m^{-1}$ vs. $55 \, m^{-1}$). For the BCA2900 design, the LCA gain drops by 185 % more on the left and by 221 % more on the right side than ref2900. On average, the BCA implantation reduces the gain outside *and* inside the active zone by 37 % and 1 % for the 700 nm design and by 142 % and 3 % for the 2900 nm design, respectively.

In summary, both BCA structures accumulate at least 25 % and up to ~450 % more gain (carriers) at the device edges than their references. These lateral accumulations become highly asymmetrical at 12 A. On average, the BCA implantation reduces (increases) the gain outside (inside) the active zone by -37 % (+1 %) for the 700 nm design and by -142 % (+3 %) for the 2900 nm design. It can be assumed that the reduction of gain outside the active zone is the main reason for the accumulations. The overall improvement of the gain profile supports a potential superiority of BCA over reference designs in terms of slope and output power that might be proven in future investigations.

---

[2]The gain minima of symmetric profiles at low currents correspond to the near-field maxima of the first TE modes, which are visible due to lateral spatial hole-burning. This is founded in the self-consistent iterative algorithm of the simulation tool *BALaser.*

(a) ca. $I_{th}+50\,\text{mA}$

(b) ca. $2\,\text{A}$
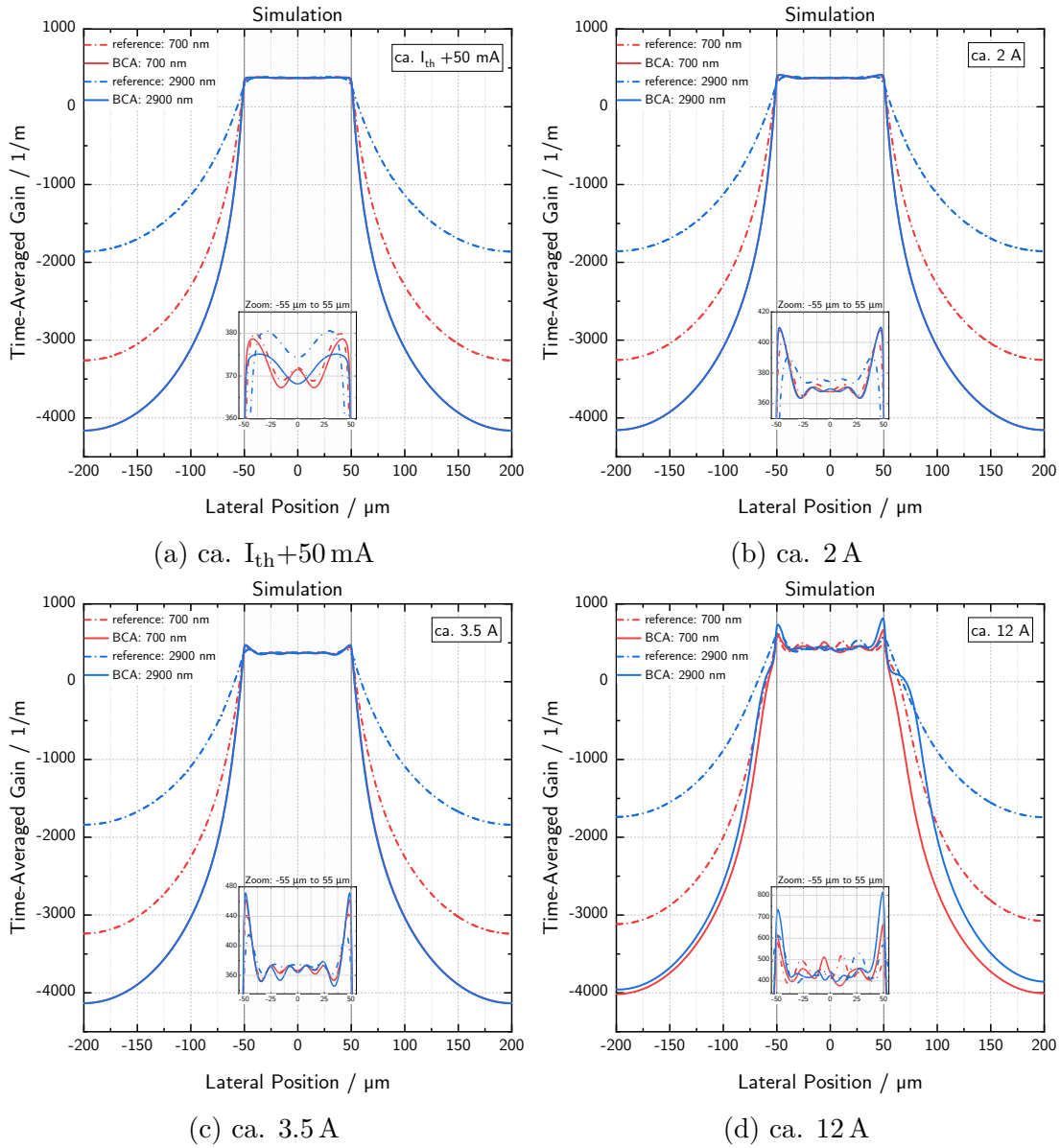
(c) ca. $3.5\,\text{A}$

(d) ca. $12\,\text{A}$

Figure 6.3.: Simulation of time-averaged lateral effective gain profiles of diodes with (BCA, solid) and without (reference, dash-dotted) buried current aperture for $700\,\text{nm}$ (red) and $2900\,\text{nm}$ (blue) thick sub-contact layers at $300\,\text{K}$.

6.1.4. Section Summary

In this section, measured and simulated PUI curves have been compared to each other. For a better quantification, the most important characteristic parameters laser threshold I_{th}, slope S, maximum output power $P_{opt}(12\,A)$ and series resistance R_s have been extrapolated from the experiment and simulation data. Relative changes Δ_{ref}^{BCA} between reference and BCA in the experiment have been analyzed and compared with the simulation. Often, these changes are of bare or even no significance, when standard deviations nearly or completely overlap. Disregarding systematic uncertainties, the thicker BCA design has been found to marginally improve the optical parameters about $1\,\%$ more than the thin BCA design, e.g. slope by $4\,\%$ and $P_{opt}(12\,A)$ by $3\,\%$ vs. $3\,\%$ and $2\,\%$. This isn't surprising considering that the $2900\,nm$ reference structure is not meant for industrial usage, being intrinsically less efficient than the $700\,nm$ reference, because of its huge current spread. However, considering the systematic power measurement uncertainty of $\pm 3\,\%$, no significant differences between the slopes and output powers of BCA and reference designs could be determined. Additionally, buried current apertures may lead their trumps only at currents higher than $12\,A$. For this reason, successive measurement campaigns with higher numbers of diode specimens and current ranges are needed.

Furthermore, the differences in Δ_{ref}^{BCA} between experiment and simulation coincide more for $2900\,m$ diodes than for $700\,nm$ (deviation ranges: $\Delta_{700\,nm} = $ 0-3\,% vs. $\Delta_{2900\,nm} = $ 2-5\,%). An overestimation of the current spread in thin designs by *BALaser* or simply insufficient statistics might be the cause. Regarding electrical parameter changes, the threshold and series resistance of $2900\,nm$ BCA diodes could be reduced by $20\,\%$ and $2\,\%$, respectively, whereas no significant change in threshold $(-1\,\%)$ and series resistance $(-5\,\%)$ could be identified for the $700\,nm$ specimens. The latter can be attributed to the high standard deviation of the $700\,nm$ reference structure. The reduction in spreading current strength has been discovered to be responsible for the reduction of threshold. If there is a link between spreading current and series resistance, it must not be pronounced as the relative spreading current has been lowered by the BCA implantation by $36\,\%$ for $700\,nm$ and by $73\,\%$ for $2900\,nm$ designs – although there is no significant difference between the respective simulated series resistances in the linear regime. A possibility remains, that deeply implanted Si atoms diffuse into the active zone, n-dope the InGaAs QW [63], decrease the local resistance and by that the series resistance. This possibility isn't simulated and could explain the reduction in series resistance observed in the experiment, but not in the simulation.

6.2. Assessment of Beam Caustics and Beam Quality

6.2.1. Near-Field

Figure 6.4 depicts the measured and simulated mean 95 % power (intensity) content near-field widths $w_{\mathrm{NF},95\,\%}$ with their standard deviations. For the measurements in fig. 6.4a, the following aspects can be noted:

- the near-field widths of ref700, BCA700 and BCA2900 peak at 5 A and approximate 82 μm at 12 A

- the near-field width of ref2900 peaks at 7.5 A, surpassing all other designs up to 118 μm, then drops steeply to 73 μm at 12 A

- of all designs, 700 nm designs deviate the strongest in the range 3.5-7.5 A

- after each narrowing, the near-fields of all designs widen slightly; at least, the slope of their narrowing decreases (except ref2900).

(a) Experiment   (b) Simulation
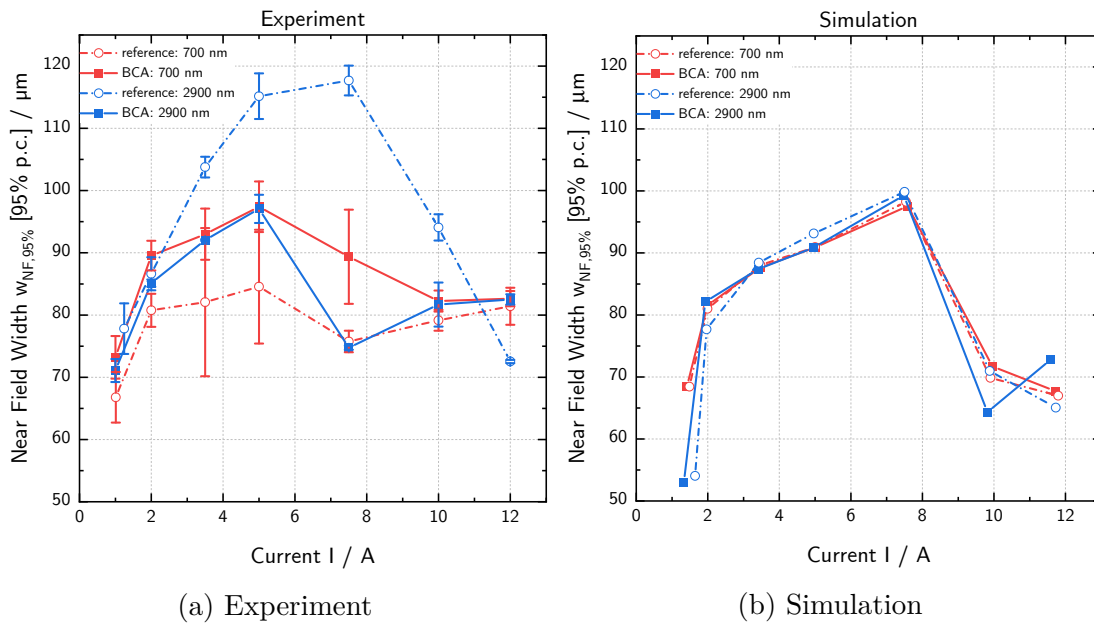
Figure 6.4.: Measured mean and simulated near-field widths with 95 % power content (p.c.). The error bars represent the standard deviations from averaging.

To some extent, this is consistent with the simulation in fig. 6.4b, except that all curves peak at 7.5 A, while having run nearly parallel to each other up to this point. Then, like in the experiment, they drop steeply and approximate a similar value (67 µm) at 12 A, except BCA2900 which grows again by about 10 µm. A particular role play the ref2900 diodes: the reason for their large deviations from the simulation is that *BALaser* does not calculate the heating due to current spread, the latter being the greatest for this design. Interestingly, in the experiment the thick reference diodes seem to be the outliers, whereas in the simulation the BCA2900 structure differs from the courses of the other curves at the last two operating points.

Now, the reason for the shrinking of the mean near-field widths for high currents, leading to a S-like curve shape, will be discussed. Owing to the BAL facets' different coatings (high-reflective at the rear, anti-reflective at the front), the optical field profile inside the resonator becomes longitudinally asymmetric. The asymmetry lowers the effective gain g_{eff} and by that increases the threshold I_{th} (cf. eqs. (2.13), (4.7) and (5.6)), which decreases the optical output power P_{opt} (cf. eq. (5.3)) [64]. As stimulated recombination rates are high within regions of high photon density, injected carriers will recombine fast, resulting in low carrier densities N near the front facet and high carrier densities near the rear facet. Consequently, spatial carrier density and optical intensity profiles are inverted to each other inside the active zone. Again, threshold current rises and output power shrinks [64]. Additionally, carriers absorb optical radiation, hence further increase optical losses α_{eff} (cf. eq. (4.8)); while also recombining non-radiatively, creating heat and reducing internal efficiency η_{int} [24, p. 205]. This phenomenon is known as longitudinal spatial hole burning [64]. It induces a longitudinal temperature and refractive index variation, based on the asymmetric optical profile (cf. fig. 6.6).

In their 2017 publication, Rauch et al. [61] analyze the near-field-narrowing of broad-area diode lasers utilizing temperature simulations. They prove the dependence of the near-field width on the longitudinal temperature variation, more precisely on the temperature-induced refractive index change (here: $\Delta n_T(T) = 2.5 \cdot 10^{-4}\,\text{K}^{-1}$) – the *thermal waveguide* or *thermal lens* (cf. eq. (4.4) and fig. 6.6). They identify a design-specific critical current I_{crit}. Below this value, resonator modes will only be locally disturbed by the induced thermal waveguide, such that on average they still follow the built-in vertical waveguide of the diode laser. But above I_{crit}, the modes start to obey the thermal waveguide. By reason of the thermal index variation, more optical intensity is concentrated on a width $< 100\,\mu\text{m}$ (BCA: w_{BCA}, reference: $w_{\text{p-contact}}$). Therefore, less optical intensity and higher carrier density is found near the edges, as seen in fig. 6.3. This gives rise to a carrier-induced refractive index reduction at the edges of $4.4 \cdot 10^{-32}\,\text{m}^{-3}$ (cf. eq. (4.4)), inverting the originally

anti-guiding lateral index profile created by the gain-guiding (now: smaller index in center, higher index at edges) [41, p. 26]. As a consequence, a self-focusing mechanism between regions with low carrier density (high opt. intensity, e.g. in center) and high carrier density (e.g. at the edges) can occur. It can produce so-called lasing filaments, which are visible in the lateral near- and far-fields, and heighten the facet load, thus potentially reducing the catastrophic optical mirror damage (COMD) power level. Hence, carrier-induced anti-guiding (negative index change) and temperature-induced guiding (positive index change) are competing effects (cf. [65]).

Obviously, the critical current for near-field-narrowing of ref700, BCA700 and BCA2900 in the experiment lies somewhere in the range 5-7.5 A and close to 7.5 A for ref2900; while in the simulation being always between 7.5 A and 10 A. In the publication [61], the slope of the NF width as function of current (at the front facet) flattens slightly at the highest simulated and measured currents, but doesn't widen for a second time as seen in fig. 6.4. As far as the author is aware of, such a S-shaped near-field width curve has not been reported, yet.

Now, the temperature gradients responsible for the near-field-narrowing at currents greater than 5 A, will be investigated. Figure 6.5 presents the simulated and measured mean temperature distributions of the standard diode designs. The experimental mean active zone temperatures in fig. 6.5c (lower curves) have been averaged and extracted from the shift of the centroid wavelength with current as explained in section 5.3. In fig. 6.5a, the simulated longitudinally-averaged temperature in dependence on the lateral position, and vice versa in fig. 6.5b, are portrayed. As seen in the former, the maximal lateral temperature range $\text{rng}(T_{\text{az,lat}})$ from coldest to hottest position accounts to about 4 K at 7.5 A for all designs. At 10 A, $\text{rng}(T_{\text{az,lat}})$ varies in the range of 5.7-6.4 K, in ascending order: BCA700, ref700, ref2900, BCA2900. In case of longitudinal temperature, $\text{rng}(T_{\text{az,long}})$ accounts to about 6.6-6.7 K at 7.5 A for all designs, except ref2900 with 5.7 K. At 10 A, $\text{rng}(T_{\text{az,long}})$ accounts to about 10.5 K for all designs. On average, the active zone's mean temperature will rise by 3.6-4 K in the simulation and by 3(2)-3.6(8) K in the experiment (no significance).

The exact values, ranges from minimum to maximum, range differences ("heating" as measure for increase of thermal lens) between lower and higher current and experimental mean temperature rise of the active zone are given in table 6.4. From the table, the following conclusions can be drawn:
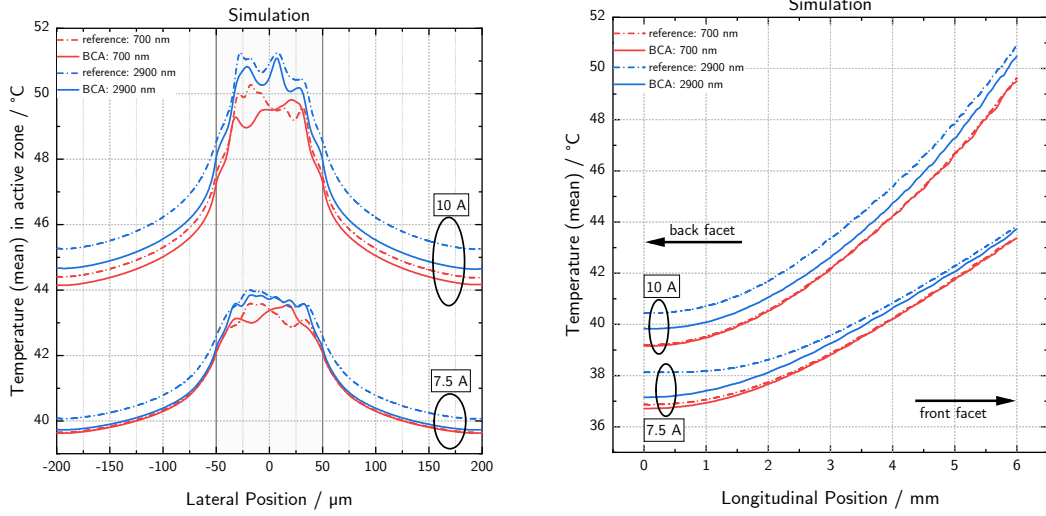
(a) Simulated lateral temperature in AZ. Longitudinal temperature is averaged at every lateral position.

(b) Sim. longitudinal temperature in active zone. Lateral temp. is averaged at every longitudinal position.
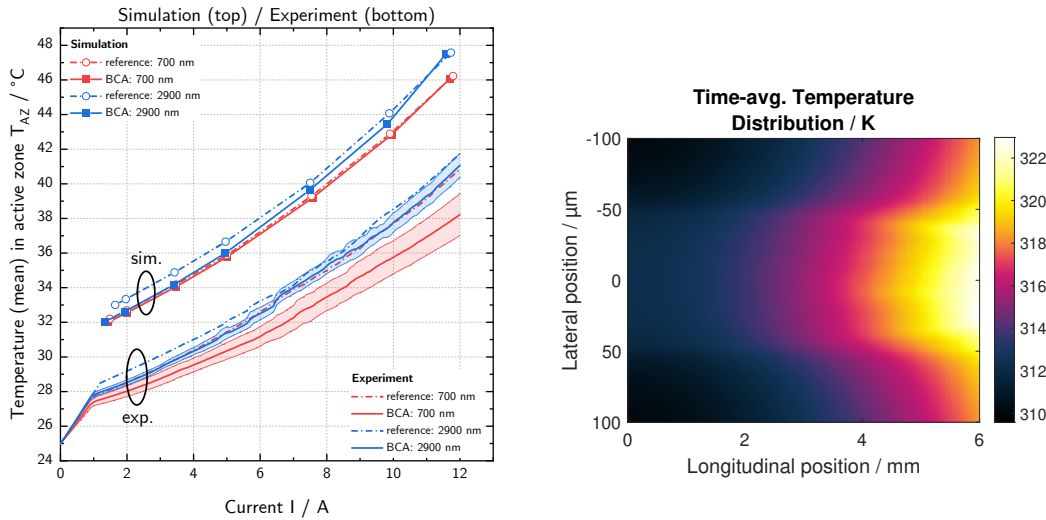
(c) Sim. and exp. mean temperature in AZ. Shaded areas represent standard deviations from averaging; SDs of references are omitted due to readability, but are similar in shape and width to their BCA counterparts.

(d) Time-averaged temperature distribution of 700 nm BCA design at 10 A. Plot is exemplary for all designs and taken directly from *BALaser* output. Most heating concentrates near the front facet.

Figure 6.5.: Lateral, longitudinal (1D) and (total, 2D) mean temperature distributions in active zone of simulated and measured BCA and reference designs.

Table 6.4.: Temperature ranges rng(T_{az}) from coldest to hottest position of simulated lateral and longitudinal temperature distributions in fig. 6.5 for 7.5 A and 10 A, range differences ("heating") and mean temperature rise of active zone from 7.5 A to 10 A (with standard deviations in brackets). The longitudinal heatings are roughly twice as big as the lateral ones, leading to stronger thermal waveguiding in the longitudinal direction within the investigated current step. The mean temperature rise in the AZ follows the trend of longitudinal heating.

| | rng($T_{\mathrm{az,lat}}$) / K | | | rng($T_{\mathrm{az,long}}$) / K | | | $\Delta T_{\mathrm{az,mean}}$ / K | |
Design	7.5 A	10 A	Heat.	7.5 A	10 A	Heat.	Sim.	Exp.
BCA700	3.9	5.7	1.8	6.7	10.4	3.7	3.6	3(2)
ref700	3.9	5.9	2.0	6.6	10.4	3.8	3.6	3(2)
BCA2900	4.1	6.4	2.3	6.6	10.6	4.0	3.8	3.2(1)
ref2900	3.9	6.0	2.1	5.7	10.5	4.8	4.0	3.6(8)

- temperature ranges per current are relatively constant between different designs (i.e. value ranges in each column), except for the lateral temperature ranges of all designs at 10 A and the outlier ref2900 at rng($T_{\mathrm{az,long}}$)(7.5 A)

- heating from 7.5 A to 10 A between designs with same sub-contact layer thickness is similar within an interval of ± 0.2 K; exception: long. temperature ranges of 2900 nm designs (because of the low temperature range of 5.7 K of ref2900 at 7.5 A), resulting in a 20 % stronger longitudinal heating compared to BCA2900

- except at $T_{\mathrm{az,long}}$(7.5 A), BCA2900 exhibits the highest temp. ranges and also the highest lateral heating of 2.3 K between the two currents

- longitudinal heating from 7.5 A to 10 A is roughly twice as strong as lateral heating and even higher for ref2900

- mean temperature rise of AZ in simulation and experiment follow the trend of longitudinal heating, though no significance in experiment, especially due to large standard deviation of 700 nm designs.

These results characterize the underlying temperature variations of the 95 % p.c. (power content) near-field width curves in fig. 6.4. The associated refractive index changes can be viewed exemplarily for BCA700 in fig. 6.6a. From 7.5 A to 10 A, Δn_{eff} rises by about $1.5 \cdot 10^{-3}$ at the front facet (5-6 mm) and by about half as much near the back facet (0-2 mm) in the active zone. Here, the longitudinal index

range inside the active region grows from $(2.5-4) \cdot 10^{-3}$ to $(3-5.5) \cdot 10^{-3}$, i.e. from $\Delta n_{\text{long}} = 1.5 \cdot 10^{-3}$ to $\Delta n_{\text{long}} = 2.5 \cdot 10^{-3}$ and thus nearly doubling the thermal lens' strength. Furthermore, the imprint of the optical field shown in figs. 6.6e and 6.6f becomes visible via carrier depletion of regions in figs. 6.6a and 6.6b and via the formation of index spikes with $\Delta n_{\text{eff}} \approx 5 \cdot 10^{-3}$ extending over 2 mm into the resonator.

Despite showing the strongest longitudinal heating (4.8 K) within the current step, the simulation still fails to reproduce the 2900 nm reference design's extraordinary near-field widening up to about 120 µm at 7.5 A and subsequent narrowing to nearly 70 µm at 12 A. As stated before, this is most probably due to the negligence of spreading-current-induced diode heating which is naturally the greatest for the thick reference design (cf. fig. 6.2a). Additionally, the simulated and measured AZ mean temperatures ΔT_{az} (last columns in table 6.4) indicate the dominance of the longitudinal heating over the lateral heating, such that the AZ's mean temperature rise is governed by the longitudinal temperature evolution. Finally, the near-field width trends of simulation and experiment differ in the range from 10 A to 12 A, i.e. experimental NF widths approach 82 µm (except ref2900 shrinks), whereas simulated ones still decrease (except BCA2900 rises). The averaged AZ mean temperatures of the range 10-12 A account to 37(1) °C, 39.2(9) °C, 39.3(6) °C, 40.1(5) °C for BCA700, ref700, BCA2900 and ref2900, respectively. Given the standard deviations, these mean temperatures may not explain the observed trend. For this reason, it remains unclear, why most designs approach the same 95 % p.c. NF width at high currents. Further measurements at currents greater than 12 A are needed.

Figure 6.5d depicts the color-coded simulated temperature distribution of the 700 nm BCA diode in dependence on the lateral and longitudinal positions. It stands exemplary for the other designs, which look comparable in shape. Inside the BCA or p-contact (reference) width of $|x| \leq 50$ µm most of the heat ($T_{\text{az}} \geq 318$ K) will be produced within a distance from the front facet of about 2 mm (yellowish area).

(a) Index change of BCA700 at 7.5 A

(b) Index change of BCA700 at 10 A

(c) Carrier density of BCA700 at 7.5 A

(d) Carrier density of BCA700 at 10 A

(e) Field intensity of BCA700 at 7.5 A

(f) Field intensity of BCA700 at 10 A
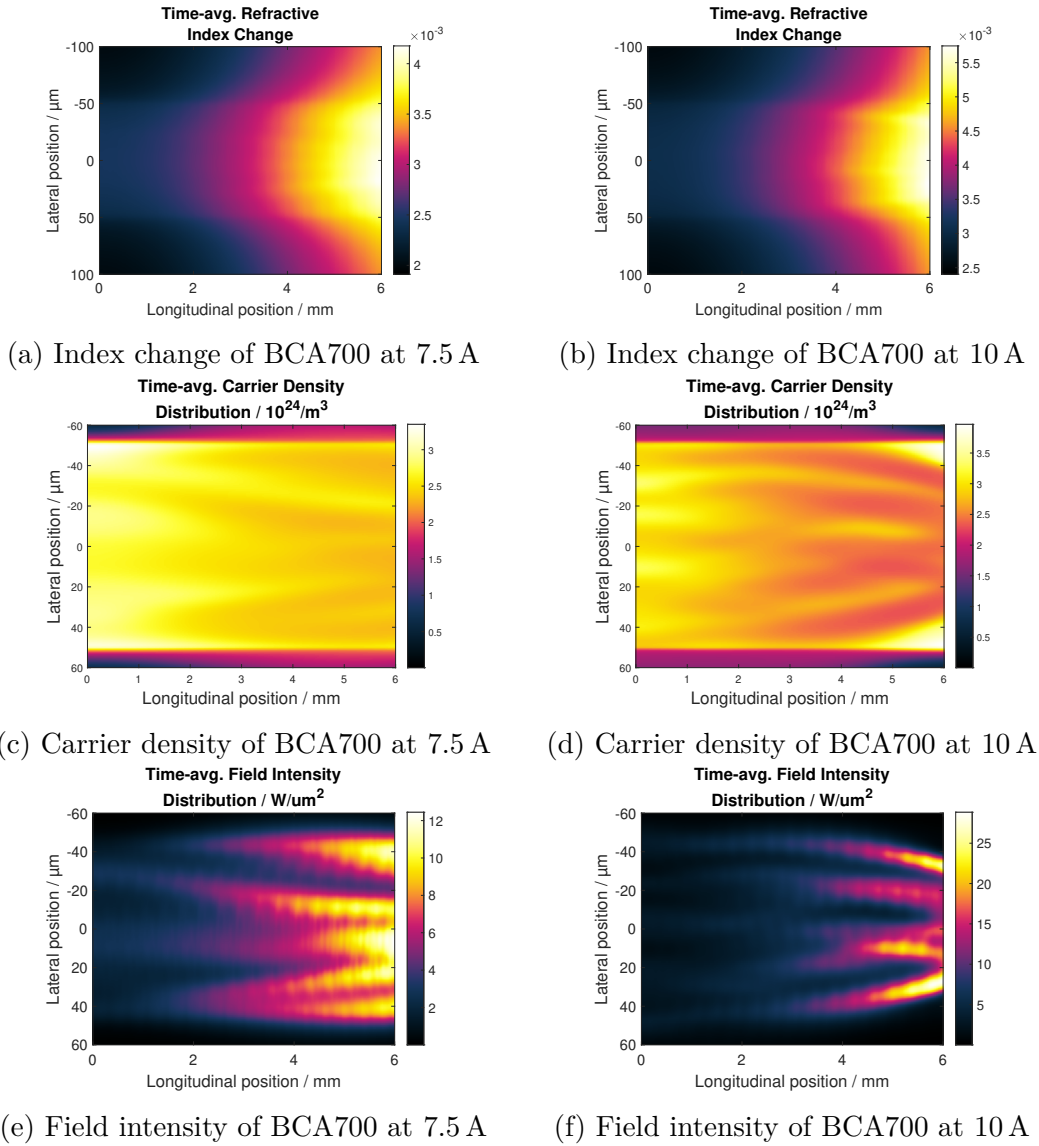
Figure 6.6.: Comparison of refractive index change, carrier density and opt. field intensity distribution of BCA700 design between 7.5 A and 10 A. Graphs are direct output of *BALaser* and visualize the the parameters responsible for the near-field-narrowing. Pay attention to the different lateral scaling of the refractive index change. 6.6b and 6.6d are more structured than at 7.5 A due to long. spatial hole burning, resulting in stronger filamentation and lateral carrier accumulation at the edges. Near-field-narrowing towards the front facet at 10 A is clearly recognizable in 6.6f.
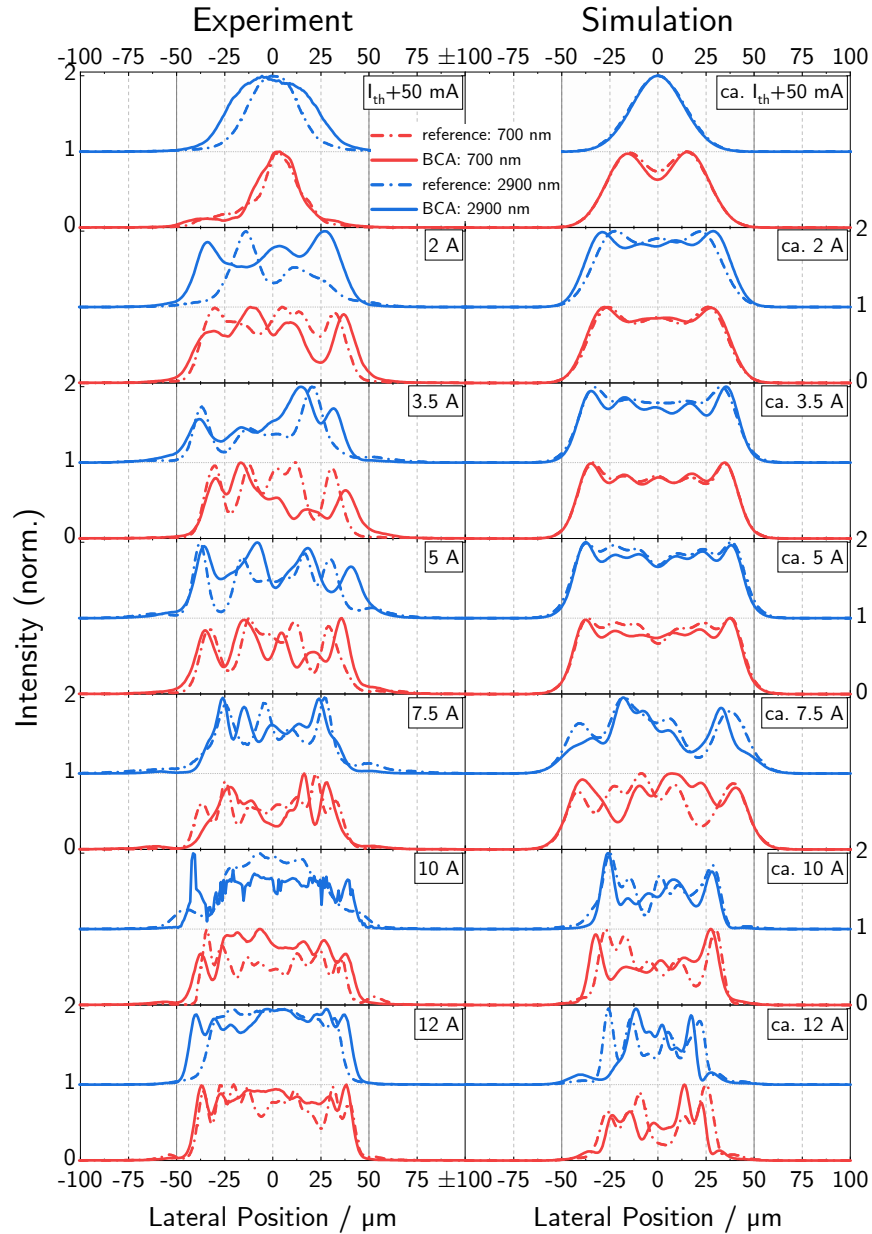
Figure 6.7.: Experimental and simulated near-field intensity distributions of the best standard designs at all operating points. At most currents, the near-fields develop side lobes with high intensities, which result from lateral carrier accumulations through the gain-guiding mechanism. The near-fields superpose of many TE modes, mainly producing stronger intensity fluctuations than in the simulation.

6.2.2. Far-Field

Figure 6.8 portrays the measured and simulated mean full divergence angles $\Theta_{95\%}$ (actually "intensity content") of the far-fields of all diodes. It follows, that all far-fields broaden in a somewhat linear fashion by 7° to 9° from $I_{th}+50\,mA$ to 12 A, with a bending in the current region around 5 A, resulting in (flattened) S-like $\Theta_{95\%}$ curves as with the near-fields in fig. 6.4 in the former section. Since far-fields (FF) can be regarded as Fourier-transformed near-fields (NF) for small lateral angles [26, p. 557], the FF broadening, i.e. the change of far-field, increases when the NF narrows. This can be seen especially at the onset of NF narrowing at 7.5 A (10 A for ref2900) in fig. 6.8a, with a FF broadening of about 1.5° (5-7.5 A) for each design except of about 2.5° for BCA2900 as well as ref2900 (7.5-10 A). However, in contrast to the exp. near-fields of BCA700, ref700 and BCA2900, which approximate a similar width of 82 μm at 12 A, the measured 95 % divergence curves of the far-fields run parallel to each other in the region 8.7°-9.7°, though with no significant difference. With BCA2900 being the exception, all simulated far-fields in fig. 6.8b approach a common max. value of about 7.8°, too. Similar in experiment and simulation in terms of far-field broadening is the dominance of the BCA2900 design over the 700 nm designs for currents greater than 7.5 A, apart from ref2900 at the last two exp. operating points.

(a) Experiment
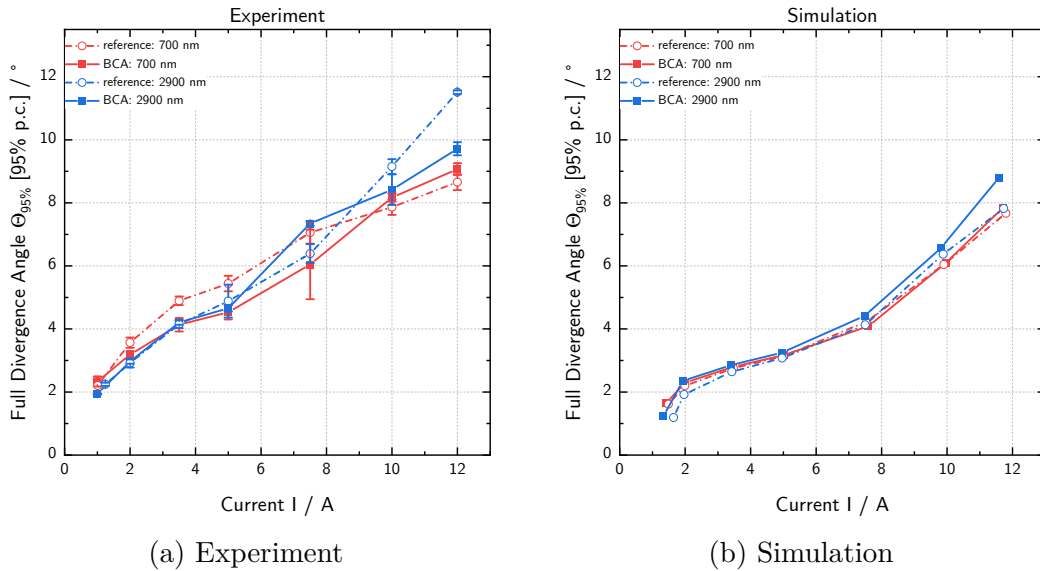
(b) Simulation

Figure 6.8.: Experimental and simulated full far-field divergence angles with 95 % power (intensity) content. Error bars are the standard deviations from averaging.

As discussed in the former section, a large longitudinal temperature gradient induces a thermal lens and by that a near-field-narrowing in certain current regimes, influencing the far-field, correspondingly. Nevertheless, high divergence angles indicate the oscillation of higher-order lateral modes. These are amplified, when carriers drift and diffuse into lateral outer-regions or accumulate at the device edges. According to the investigations of Piprek and Li [66], lateral carrier accumulation (see below) at the contact (or BCA) edges can account for up to 50 % of the lateral far-field broadening (hinted by [67]), i.e. the *change* of the lateral divergence angle. In fact, the simulated (95 %) far-field of BCA2900 (fig. 6.8b) broadens from 10 A to 12 A by 2.2° and from 1.2° at I_{th}+50 mA to 8.8° at 12 A by 7.6°. The former range corresponds to a broadening of 2.2°/7.6°=29 % (experiment: 1.3(6)°/7.8(3)°=17(7) %) compared to the rise in the whole current range, and to 2.2°/5.3°=42 % (experiment: 1.3(6)°/6.5(5)°=20(9) %) of the broadening up to 10 A. In particular the results of the simulated BCA2900 and measured ref2900 (25(3) % and 34(4) % for same ranges, respectively) structures are in line with the observations in [66]. In general, the broadening at high currents in the experiment is not as steep as in the simulation.

Figure 6.9 depicts the time-averaged lateral carrier densities at all operating points and 25 A. Above threshold, the carrier density in the active zone ($|x| < 50$ µm) clamps to a constant level of about $2.35 \cdot 10^{24}$ m^{-3}, because of spatial hole-burning, i.e. carriers recombine faster than they are injected [26, p. 542]. Up to 5 A, the carrier densities continue to rise and peak near $x = \pm 50$ µm. This phenomenon is known as lateral carrier accumulation (LCA). With increasing injection current, these peaks approach the AZ's edges from the inside, i.e. from ± 42 µm close above threshold over ± 48 µm (2 A) to ± 49 µm (3.5 A) to ± 50 µm (12 A). In other words, the carrier density (and gain) plateaus inside the active zone widen slightly with rising current, so the carriers accumulate more and more at the edges. The 7.5 A operating point is an exception: the LCA near $x = \pm 50$ µm shrinks for all designs. Beyond that, beginning at 7.5 A and continuing at higher currents, carriers start to accumulate in the lateral outer-regions $|x| > 50$ µm, which is noticeable by the laterally extending *bulges*. Up to 7.5 A, carrier density profiles have hardly changed at all in the lateral outer-regions, staying relatively symmetrical with respect to the center $x = 0$ µm. While BCA700 and ref700 share comparable bulges, BCA2900 and ref2900 do not (except at 25 A). Actually, the bulges of the BCA2900 design at 7.5 A and 12 A are the most pronounced. In addition, LCA peaks of BCA2900 surpass all other LCA peaks, while those of BCA700 are mostly just barely larger than ref700 (if at all). Furthermore, ref2900 shows even less LCA at 10 A and particularly at 25 A than ref700.
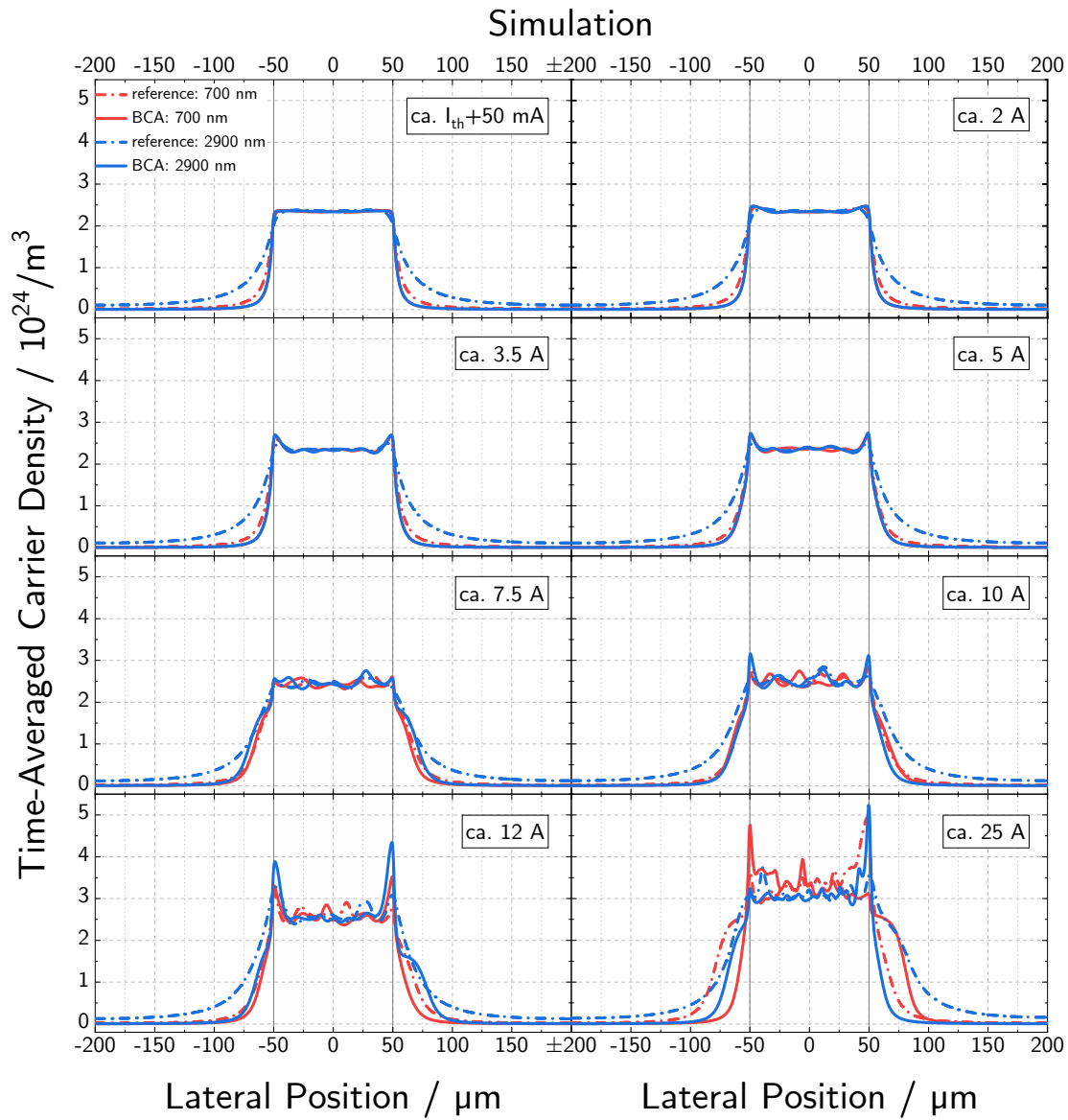
Figure 6.9.: Simulated time-averaged lateral carrier densities at the experimental operating points and 25 A. Diodes with buried current apertures portray a stronger lateral carrier accumulation than reference diodes, especially for higher currents. For qualitative details of the active zone, please refer to the zoomed insets in fig. 6.3.

These findings indicate a more inhomogeneous carrier density distribution of diodes with a 2900 nm thick sub-contact layer and slightly also for diodes with BCA implantation. The inhomogeneities can be recognized as bulges, as is the case at $x > 50\,\mu$m of BCA2900 at 12 A, but also as LCA peaks of BCA designs exceeding those of their references, e.g. also at 12 A (exceptionally visible at 25 A). Depending on the carrier density, lateral inhomogeneities provide higher-order lateral TE modes with gain, which widens the far-field as seen in fig. 6.8b. Taking the BCA2900 bulge at 12 A as an example, (positive) gain is indeed provided up to about $x = 70\,\mu$m (cf. fig. 6.3d), as is for ref2900 (BCA700: $x \approx \pm 57\,\mu$m, ref700: $x \approx \pm 60\,\mu$m). Since the measured divergence angles of the BCA2900 design exhibit very small standard deviations in the range of up to $\pm 0.2°$ (max.: $\pm 0.5°$ at 10 A, cf. fig. 6.8a), it is very likely that these (simulated) lateral inhomogeneities are the cause for the (real) far-field broadening of the 2900 nm BCA design. The extreme broadening of ref2900's measured far-field for currents above 7.5 A correlates with its extreme near-field-narrowing due to thermal waveguiding. Thus, ref2900's $\Theta_{95\%}$ progression can be explained by the fact, that its structure possesses the highest "measured" mean active zone temperature of all designs, as depicted in fig. 6.5c (*far-field blooming*). As a side note: such carrier density / gain bulges near the edges also explain the small side peaks of near-fields at higher currents in fig. 6.7, which will be explored in more detail in section 6.3.2.

Concerning the two 700 nm designs, no general noteworthy difference between their CD distributions can be identified; as is the case with the measured $\Theta_{95\%}$ curves for currents greater than 5 A (due to SD). However, at 2-5 A, measured divergence angles of BCA700 and ref700 differ significantly, with the reference broadening stronger than the BCA design. What may *not* serve as reason, is the marginally higher longitudinal temperature gradient of ref700 $\Delta T_{\mathrm{az,long}} = 3.8\,$K than BCA700 $T_{\mathrm{az,long}} = 3.7\,$K (hence stronger thermal lens, near-field-narrowing and far-field broadening). This is because the corresponding experimental critical current for the formation of a thermal lens lies in the range 5-7.5 A (7.5-10 A for ref2900), as shown in the former section and visualized by the simulated optical field profiles in fig. 6.6. Instead, in this current region, experimental carrier density distributions of 700 nm reference diodes might be wider than predicted by the simulation. This favors broader far-fields, as seen in the simulation at 25 A for $x > 50\,\mu$m.
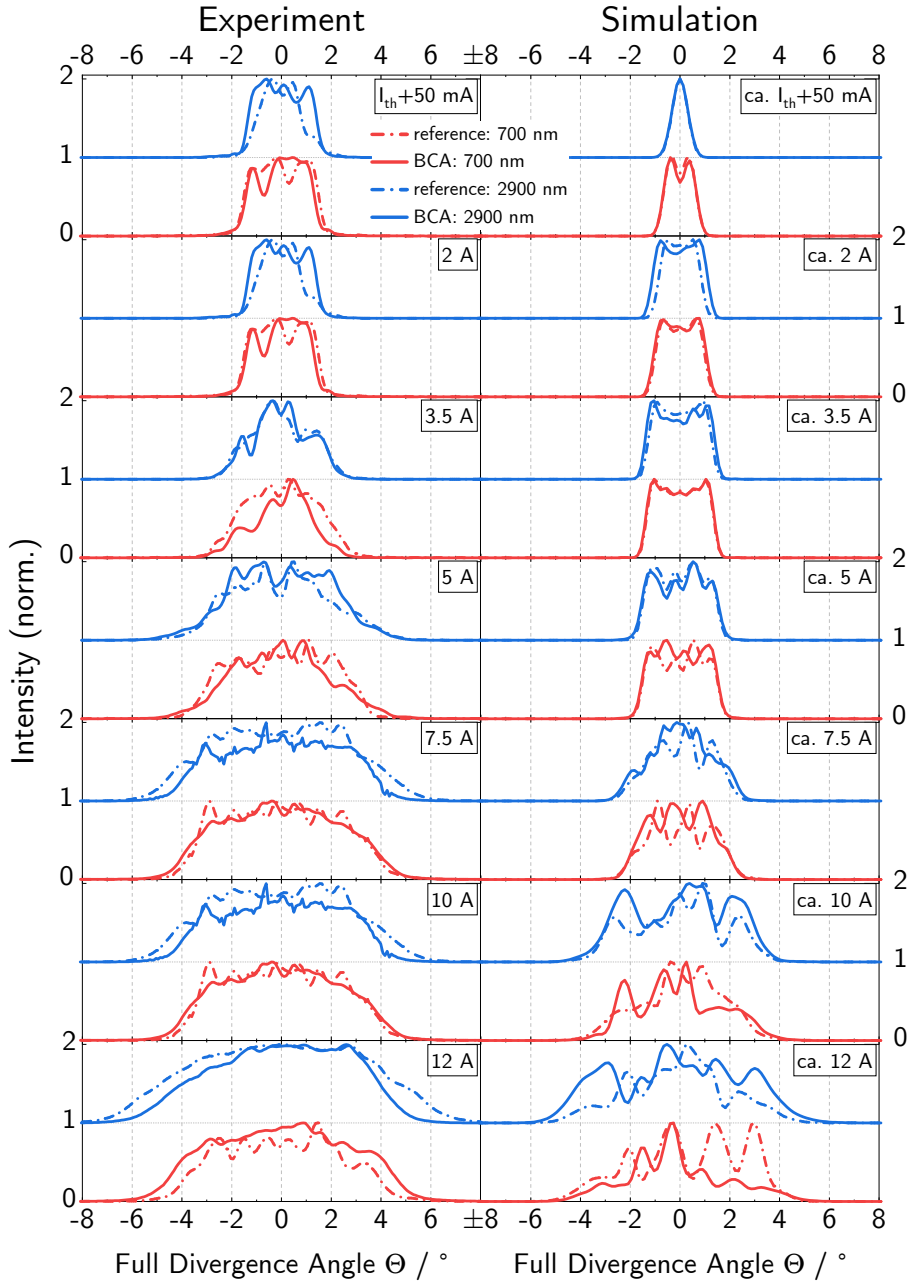
Figure 6.10.: Experimental and simulated far-field intensity distributions of the best standard designs at all operating points. The critical current for thermal waveguiding in the range 5-7.5 A (7.5-10 A for ref2900 and simulation) causes a broadening of the far-field. This creates more homogeneous far-fields than below 7.5 A in the experiment and than above 7.5 A in the simulation.

6.2.3. Beam Quality

Current Dependence

Figure 6.11 depicts the lateral beam parameter products in experiment and simulation including 95 % of the beam's power (intensity). The experimental $BPP_{lat,95\%}$ has been calculated using eq. (5.25) and the ideal BPP_{ideal}=0.29 mm mrad (dashed purple line) using eq. (5.26) with $\lambda = 915$ nm and $M^2_{lat} = 1$, where the latter serves as rough guideline for the best BPP_{lat} possible. The experimental error bars / measurement uncertainties have been propagated from the near-field widths $w_{NF,95\%}$ and full far-field divergence angles $\Theta_{95\%}$. As expected, up to 10 A (2.75-3 mm mrad) no significant difference between the BCA700, ref700 and BCA2900 designs can be observed. In fact, up to 7.5 A these graphs run nearly parallel to each other.

(a) Experiment

(b) Simulation
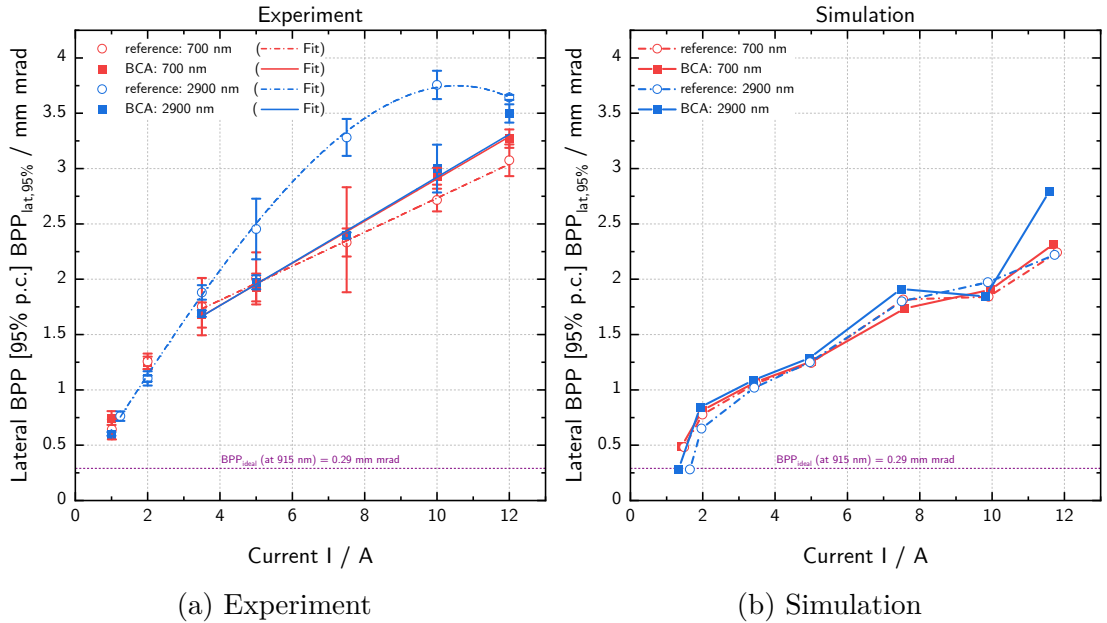
Figure 6.11.: Experimental and simulated lateral beam parameter product with 95 % power content (p.c.) with linear (ref700, BCA700, BCA2900) and cubic (ref2900) fits. The measurement uncertainties (error bars) have been propagated from the standard deviations (from averaging) of $w_{NF,95\%}$ and $\Theta_{95\%}$ using Gaussian's law of uncertainty propagation. The ideal BPP is not accurate and barely serves as an orientation, since the actual centroid wavelength λ_{cen} of each laser hasn't been taken into account, but instead the project's target wavelength $\lambda = 915$ nm.

This is because of the rule of thumb "narrow near-field, divergent far-field" as demonstrated in the former subsections. For example, apart from their high standard deviation, the ref700 diodes possess the narrowest near-field on average (cf. fig. 6.4a) up to 10 A, but also the most divergent far-field (cf. fig. 6.8a) up to 7.5 A. This argumentation can be repeated analogously for every design, which leads to the mostly linear and parallel running $BPP_{lat,95\%}$ curves seen both in experiment and simulation. Only for high currents at 10 A and above, deviations between the mentioned designs (not ref2900) begin to appear, though with no significance (e.g. BCA700 vs. ref700) or bare significance (e.g. ref700 vs. ref2900 or BCA2900). The high measurement uncertainties of the 700 nm structures and partially also of ref2900 in the range from 3.5 A to 7.5 A are clearly reflected in the lateral beam parameter product. In general, BCA2900 displays the smallest standard deviations (SD) of all designs (± 0.09 mm mrad at max.), except at 10 A. What's most remarkable, is the progression of the ref2900 design, again. Its $BPP_{lat,95\%}$ shows hardly any SD up to 3.5 A, then surpasses the others at 5 A with high SD, peaks at 3.8 mm mrad at 10 A with lower SD and decreases to 3.6 mm mrad at 12 A with its lowest SD (± 0.02 mm mrad) of all designs. This progression is comparable to ref2900's near-field width curve in fig. 6.4a. As such, it originates from its wide and high current spreading observed in fig. 6.2 and the thermal waveguide, which forms at high currents.

In comparison with the simulation in fig. 6.11b, all curves progress qualitatively similar to the experiment with minor differences, except for ref2900. These differences are: the progression of the ref2900 curve and the position/range of the critical current, as investigated in context of the near-field-narrowing in section 6.2.1. The narrowing invokes a slope reduction of the $BPP_{lat,95\%}$ curves at 7.5 A for BCA700, ref700 and BCA2900 and at 10 A for ref2900 in the experiment; and at 10 A for all designs in the simulation. Finally, the outstanding increase of BCA2900 at the last operating point by 0.5 mm mrad (to 3.5 mm mrad) in experiment and by 1 mm mrad in the simulation can be attributed to an inhomogeneous lateral carrier density distribution, which favors higher-order TE modes as pointed out in the analysis of the far-fields in the former section.

For a better estimation of the $BPP_{lat,95\%}$ degradation with current, appropriate ranges of the graphs in fig. 6.11a have been fitted linearly. Here, the sizes of the y-error bars (SD) have been accounted for by weighing the fit points with their standard deviations ("instrumental weight $1/\sigma^2$"), so points with small SD get more importance in the fitting process. Also, the goodness of fitting is represented by scaling the computed standard errors with the square root of the reduced χ^2 value. For further information, please refer to the fitting documentation [68–71]. The resulting slopes S_{BPP} of the linear regression are collected in table 6.5. In some

Table 6.5.: Slopes of experimental lateral beam parameter products (95 % p.c.) taken from linear fits in the given current ranges. Italic values incorporate high *fitting* uncertainties and are given for comparison purposes only. The uncertainties in brackets are the standard errors (SE) of the linear regression. The low SE of the ref2900 fit in the first column is due to the $1/\sigma^2$ weighting of the first and last fit points, which possess considerably lower SDs.

	Slope S_{BPP} of exp. $\mathrm{BPP}_{\mathrm{lat},95\,\%}$ / mm mrad A^{-1}		
Design/Range	3.5 A $-$ 12 A	$\mathrm{I_{th}}$+50 mA $-$ 7.5 A	$\mathrm{I_{th}}$+50 mA $-$ 12 A
BCA700	0.19(1)	*0.30(5)*	*0.22(2)*
ref700	0.15(1)	*0.24(5)*	*0.21(2)*
BCA2900	0.19(1)	*0.28(4)*	*0.27(3)*
ref2900	*0.20(2)*	0.44(3)	*0.26(2)*

regions, graphs deviate strongly from single straight lines, i.e. have low goodness of fitting, which is why the slopes calculated in these regions are written italic. From the first column follows, that there is no difference in $\mathrm{BPP}_{\mathrm{lat},95\,\%}$ degradation $(0.19(1)\,\mathrm{mm\,mrad\,A^{-1}})$ between the two BCA designs for currents equal or greater than 3.5 A. In fact, in this range, ref700 presents the lowest degradation $S_{\mathrm{BPP}} = 0.15(1)\,\mathrm{mm\,mrad\,A^{-1}}$ of all designs. From close above threshold to 7.5 A (second column), ref2900 exhibits a linear trend and the highest $\mathrm{BPP}_{\mathrm{lat},95\,\%}$ degradation $S_{\mathrm{BPP}} = 0.44(3)\,\mathrm{mm\,mrad\,A^{-1}}$ measured. With respect to the whole current span (last column), there are neither significant differences between the 700 nm ($\sim 0.22(2)\,\mathrm{mm\,mrad\,A^{-1}}$) diodes, nor for the 2900 nm ($\sim 0.27(3)\,\mathrm{mm\,mrad\,A^{-1}}$) ones, but the latter degrade faster than the former.

Temperature Dependence

Following the work of Winterfeldt in [57, pp. 41 sqq.], the influence of the induced thermal waveguiding on the lateral beam parameter product can be evaluated by plotting $\mathrm{BPP}_{\mathrm{lat},95\,\%}$ in dependence on the active zone temperature increase ΔT_{az}. This is because ΔT_{az} is a relative change, which can be compared between different laser designs; whereas current is a static absolute measure, i.e. different lasers may possess different active zone temperatures at the same current and hence different thermal lenses. In this specific discussion, inhomogeneities of the carrier densities will be neglected. The active zone temperatures T_{az} are calculated from the wavelength shift of the spectrum with temperature, as derived in section 5.3 and portrayed in fig. 6.5c, and subtracted from the heat-sink temperature $T_{\mathrm{HS}} = 25\,°\mathrm{C}$ to reveal $\Delta T_{\mathrm{az}} = T_{\mathrm{az}} - T_{\mathrm{HS}}$. Then, the data points are fitted linearly for $\Delta T_{\mathrm{az}} > 4\,\mathrm{K}$
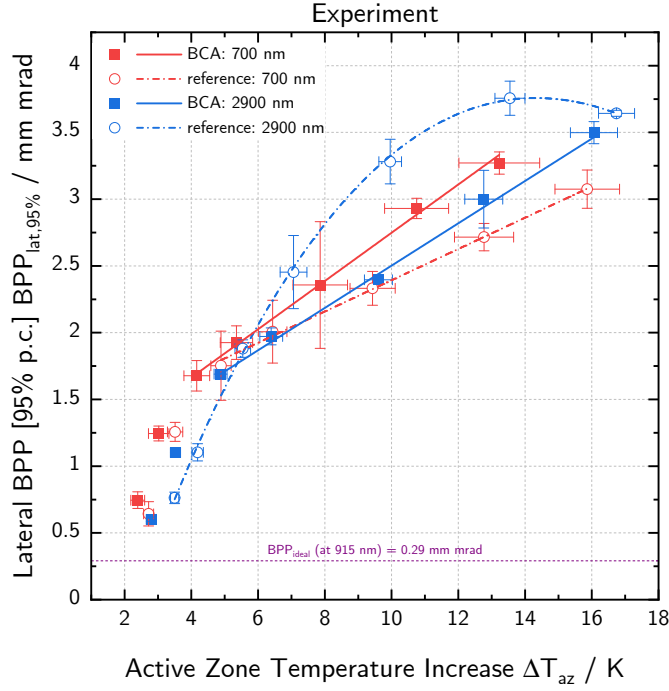
Figure 6.12.: Experimental lateral beam parameter product with 95 % power content against active zone temperature increase. The BCA designs and the 700 nm reference design have been fitted linearly in the range 4-16 K, whereas the 2900 nm reference has been fitted with a cubic polynomial in the full ΔT_{az} range. Fit parameters are listed in table 6.6. Measurement uncertainties are represented by x- and y-error bars, which have been propagated by and obtained from the York linear fit.

in the cases of BCA700, ref700 and BCA2900 and cubic-polynomial for the complete temperature increase range in case of ref2900; with the results shown in fig. 6.12. In order to account for the standard deviations of ΔT_{az} (x) *and* $\mathrm{BPP}_{\mathrm{lat},95\%}$ (y) when fitting, the York linear model has been used [72, 73]. The fit parameters are provided in table 6.6.

What's most noteworthy by comparing fig. 6.11a with fig. 6.12, is the similarity of the $\mathrm{BPP}_{\mathrm{lat},95\%}$ curve progressions. It is therefore reasonable to state that the internal temperature rise of the active zone has a high - if not the highest - impact on the lateral beam parameter product.[3] Similar to [57, p. 44], a linear model for

---

[3]Unfortunately, the conducted simulations do not allow to distinguish between the different influences of carrier density distribution and active zone temperature, since both rise with current.

Table 6.6.: Fit parameters of the curves in fig. 6.12 for a cubic polynomial fit $y(x) = \mathrm{BPP}_0 + \mathrm{S_{th}}\, x + \mathrm{C} x^2 + \mathrm{D} x^3$ in the given ΔT_az range. Uncertainties in brackets are the standard errors of the regression method. The linear $(C = D = 0)$ fitting range begins with the third operating point $(\Delta T_\mathrm{az} \approx 4\,\mathrm{K})$. Italic values are linear fit parameters that don't reflect ref2900's curve progression and are given for comparison purposes only.

Param./Design	BCA700	ref700	BCA2900	ref2900	
ΔT_az range		4-16 K			2-18 K
$\mathrm{BPP}_0/\mathrm{mm\,mrad}$	0.9(2)	1.2(3)	0.9(1)	*1.0(4)*	-1.8(3)
$\mathrm{S_{th}}/\mathrm{mm\,mrad\,K^{-1}}$	0.18(2)	0.12(2)	0.16(1)	*0.17(4)*	0.87(9)
$C/\mathrm{mm\,mrad\,K^{-2}}$	0	0	0	0	-0.04(1)
$D/\mathrm{mm\,mrad\,K^{-3}}$	0	0	0	0	0.0005(4)

the ΔT_az dependence of the $\mathrm{BPP_{lat,95\,\%}}$ emerges from fig. 6.12:

$$\mathrm{BPP_{lat,95\,\%}}(\Delta T_\mathrm{az}) = \mathrm{BPP}_0 + S_\mathrm{th}\Delta T_\mathrm{az}. \tag{6.1}$$

Here, $\mathrm{BPP}_0 = \mathrm{BPP_{lat,95\,\%}}(0\,\mathrm{K})$ resembles an intrinsic non-thermal ground-level, which originates from the device design and S_th the thermal degradation slope. Equation (6.1) holds true for the structures BCA700, ref700 and BCA2900 for $\Delta T_\mathrm{az} \geq 5\,\mathrm{K}$. For ref2900, no linear dependence can be found for higher temperatures (only up to $\Delta T_\mathrm{az} = 11\,\mathrm{K}$ like with current), but a cubic dependence for the full ΔT_az range. The 2900 nm reference diodes can not be compared properly, due to their non-linear progression. As such, the linear model may only be applied up to $\Delta T_\mathrm{az} = 7\,\mathrm{K}$, or 10 K at maximum, which disqualifies ref2900 from comparison with the other designs. From table 6.6 the thermal slopes read $0.18(2)\,\mathrm{mm\,mrad\,K^{-1}}$, $0.12(2)\,\mathrm{mm\,mrad\,K^{-1}}$ and $0.16(1)\,\mathrm{mm\,mrad\,K^{-1}}$ for BCA700, ref700 and BCA2900, respectively. Neither do both BCA designs differ significantly in thermal slope nor do BCA2900 and its reference. However, BCA700's $\mathrm{BPP_{lat,95\,\%}}$ degrades thermally 50 % faster than its reference, although BCA700' active zone heats up less with current. Concerning the non-thermal ground-level BPP_0, no significant difference between any structure can be determined at all.

6.2.4. Section Summary

In section 6.2.1, the measured widening and successive narrowing of the near-field with current and temperature has been investigated. Except for ref2900, whose near-field widens extremely and narrows subsequently, the $w_{\mathrm{NF},95\%}$ curves exhibit a S-shaped curvature and approximate a common width of about $82\,\mu\mathrm{m}$ (cf. fig. 6.4). This behavior is reasoned by the simulation with the creation of a thermal waveguide at the critical current I_{crit}: from $7.5\,\mathrm{A}$ to $10\,\mathrm{A}$ the diode heats about two times as much in the longitudinal direction (~$4\,\mathrm{K}$) than in the lateral direction (~$2\,\mathrm{K}$) (cf. fig. 6.5). For example, when BCA700 passes I_{crit} between $7.5\,\mathrm{A}$ and $10\,\mathrm{A}$, the longitudinal refractive index change from rear to front grows from $\Delta n_{\mathrm{long}} = 1.5 \cdot 10^{-3}$ to $\Delta n_{\mathrm{long}} = 2.5 \cdot 10^{-3}$ and thus nearly doubles the thermal waveguide's strength. This effect is even stronger for the other designs (especially ref2900), since the respective longitudinal temperature ranges are even greater. The effect would be verified by the trend of the experimental mean active zone temperature rises (last column in table 6.4), if it weren't for their high standard deviations, e.g. $\Delta T_{\mathrm{az,mean}}^{\mathrm{BCA700}} = 3(2)\,\mathrm{K}$. The common approximation to $w_{\mathrm{NF},95\%} = 82\,\mu\mathrm{m}$ can be traced back to the lateral carrier accumulation at the active zone edges, that is discussed in context of the far-fields. LCA peaks provide higher-order TE modes with gain. At the same time, they create high carrier density gradients, which boosts carrier diffusion into lateral outer-regions. In fact, positive gain is provided in a design-dependent small region $|x| \gtrsim 50\,\mu\mathrm{m}$ that exceeds the active zone. This is the origin of the measured near-field side lobes at high currents. Furthermore, high carrier densities reduce the refractive index (cf. eq. (4.5)), which works against the induced thermal waveguide, re-confines the optical mode and stabilizes the near-field narrowing.

Beyond that, it is important to note that the experimental $T_{\mathrm{az,mean}}$ values of the $700\,\mathrm{nm}$ designs are more diversified, leading to standard deviations that are one magnitude higher than the $2900\,\mathrm{nm}$ values. In other words, although the simulation (no significance in experiment) indicates a stronger heating of diodes with a $2900\,\mathrm{nm}$ sub-contact layer, those diodes reproduce more close temperature values than their $700\,\mathrm{nm}$ variants. Concerning the shape of the lateral near-field distributions (cf. fig. 6.7), there are remarkable disparities between experiment and simulation. Up to $7.5\,\mathrm{A}$, the experimental near-fields are much more inhomogeneous and asymmetric than in the simulation. That is, until $12\,\mathrm{A}$, when the situation reverses and the best diodes of the experiment display a more homogeneous near-field distribution.

In section 6.2.2, the influence of the lateral carrier density distribution on the broadening of the far-fields with current has been investigated (cf. fig. 6.10). In context of the PUI discussion, the simulation reveals a lateral carrier accumulation

at the edges of the active zone $x \approx \pm 50\,\mu\text{m}$ for BCA and reference diodes alike (cf. fig. 6.9). These accumulations rise with current (except at 7.5 A), are significantly larger for 2900 nm structures and only marginally larger for BCA than for reference structures. Additionally, lateral carrier density inhomogeneities outside the active zone $x > 50\,\mu\text{m}$ develop in the form of bulges, especially for the BCA2900 design. Up to roughly $x = \pm 70\,\mu\text{m}$, carrier densities are big enough to provide gain to higher-order lateral modes with wider divergence angles. Exemplary for the BCA2900 diodes it has been shown, that the LCA and lateral inhomogeneities are most probably the cause of the observed far-field broadening of up to 42 % in the simulation (20(9) % in the experiment) towards the highest current compared to the total broadening up to 10 A.

In section 6.2.3, the lateral beam parameter product $\text{BPP}_{\text{lat},95\,\%}$, which unites $w_{\text{NF},95\,\%}$ and $\Theta_{95\,\%}$ to a measure of focusability and beam quality, has been studied in dependence on current and temperature. Except for ref2900, all experimental $\text{BPP}_{\text{lat},95\,\%}$ curves exhibit a double-linear characteristic, with the two linear ranges being I_{th}+50 mA-3.5 A and 3.5-12 A (cf. fig. 6.11a); whereas ref2900 can be fitted remarkably well with a cubic-polynomial fit. The latter's beam quality is the worst of all designs, being driven by its large and widely spreading current, which creates an equally large gain distribution and waveguide. All others' standard deviations overlap such that no significant difference between the beam qualities can be measured. However, the extremely small SDs of the BCA2900 diodes (except at 10 A) indicate a reproducible beam quality, which can also be seen from the relatively low SDs of the mean active zone temperatures of the 2900 nm structures (cf. fig. 6.5c). Having taken into account the standard deviations, it has then been shown from the fits that ref700's $\text{BPP}_{\text{lat},95\,\%}$ tends to degrade the slowest ($S_{\text{BPP}} = 0.15(1)\,\text{mm}\,\text{mrad}\,\text{A}^{-1}$), while the BCA designs degrade equally fast ($S_{\text{BPP}} = 0.19(1)\,\text{mm}\,\text{mrad}\,\text{A}^{-1}$) and ref2900 the fastest ($S_{\text{BPP}} \geq 0.20(2)\,\text{mm}\,\text{mrad}\,\text{A}^{-1}$) with current. A subsequent study of the beam quality's temperature dependence (cf. fig. 6.12) exposes that, although BCA700's active zone heats up less with current, its $\text{BPP}_{\text{lat},95\,\%}$ degrades about 50 % faster at higher currents with rising active zone temperature ΔT_{az} than its reference (S_{th}=0.18(2) mm mrad K^{-1} vs. 0.12(2) mm mrad K^{-1}) and about equally quick as BCA2900 (0.16(1) mm mrad K^{-1}). The other designs do not differ significantly either in thermal slope S_{th} or in non-thermal ground-level BPP_0.

6.3. Influence of Strain on the Polarization

In this section, the influence of strain on the polarization properties will be investigated by means of the best diodes. Furthermore, mean characteristic 95 % parameters will be derived and analyzed in dependence on their polarization.

6.3.1. Degree of Polarization

External strain, i.e. strain that does not arise from the compressive strain via lattice-mismatching of the InGaAs quantum well to the waveguide and cladding layers, is induced by mechanical stress, which in turn stems from soldering and mounting processes (cf. section 3.1). Mechanical stress is naturally more pronounced near the device edges, as shown in similar publications [74, 75]. Since the internal (compressive) strain splits the light hole lh and heavy hole hh valence bands (cf. fig. 3.3a) by different amounts per strain unit, it changes the most probable transition to e-hh and by that to TE-polarized light. Local external tensile strain reduces the local compressive strain and by that the degree of TE-polarization, while increasing TM-emission. Another reason for TM emission is the induction of birefringence due to sheer stress on the semiconductor crystal [59, 76]. It causes a rotation of the polarization plane and as such of the TE modes into TM-direction. By these means, strain can be identified as TM-polarized emission of light near the device edges.

The polarization of three specimens per design (also for BCA700, formerly six) has been measured in dependence on the rotation angle ω of a polarizing beam splitter (PBS) by using the setup described in section 5.5. The degree of TE-polarization $\mathrm{DOP_{TE}}$ has then been calculated according to eq. (5.28), with an average standard error of the nonlinear fit of $\Delta_\omega = 3\,\%$ [59]. It is portrayed for the standard designs in fig. 6.13. The error bars result from averaging over values of the single specimens, where the wider error bars belong to the lasers with buried current apertures (full squares). In general, the BCA designs deviate stronger (up to 1.1 p.p.) than their references and the $700\,\mathrm{nm}$ structures deviate more than the $2900\,\mathrm{nm}$ ones. As such, all error bars overlap, with standard deviations increasing from ref2900, BCA2900, ref700 to BCA700 in ascending order. This leads to no significant $\mathrm{DOP_{TE}}$ differences between the models. Still, all lasers emit light with a $\mathrm{DOP_{TE}}$ being significantly higher than $97.5\,\%(\pm 3\,\%)$. Second, it is likely, that on average ref2900 has the highest $\mathrm{DOP_{TE}}$, because of its low SD of 0.2 p.p. at maximum $(7.5\,\mathrm{A})$; although the other designs shrink the gap to ref2900 at high currents.
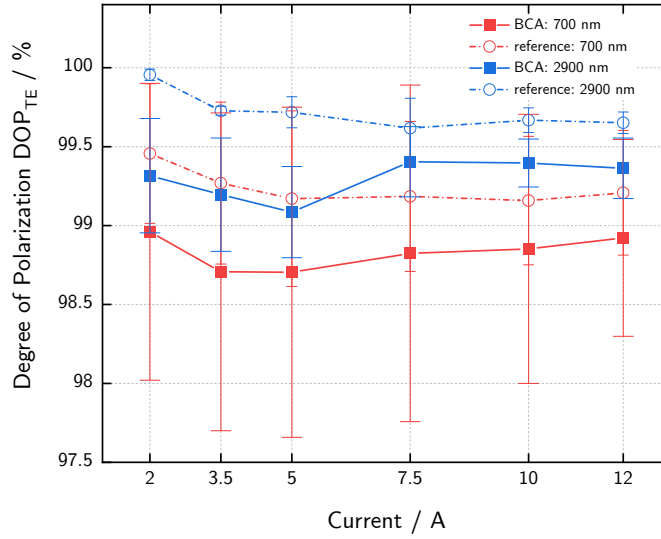
Figure 6.13.: Experimental degree of TE-polarization DOP$_{\text{TE}}$. The error bars are the standard deviations from averaging over all diode specimens (without standard error $\Delta_\omega = \pm 3\,\%$).

Albeit no significant differences in the degree of TE-polarization could be measured, it is sill reasonable to assume that the deep implantation of buried current apertures by the two-step-epitaxy introduces strain into the diodes. These strains might be further facilitated by the soldering of the diode onto the submount and subsequent into the CCP mount. This leads to the next subsection.

6.3.2. Polarization-Resolved Near- and Far-Field Distributions

In order to investigate the introduction of stress-induced strain into the diodes with more detail, polarization-resolved lateral near- and far-field distributions have been measured with the setup in fig. 5.6 at 2 A, 7.5 A and 12 A. The polarization could be selected by turning a polarized beam splitter (PBS) in front of the laser diode. By observing the image created by the adjustment camera, the intensity maximum and minimum could be identified and have been subsequently declared as TE- and TM-polarization plane, respectively. After measurement, the polarization-resolved 95 % NF widths and FF divergence angles are computed, and their lateral distributions centered with respect to the first momentum of the detector position and divergence angle, respectively; according to DIN EN ISO 11146-1:2005 [58]. But since TM-polarized light makes up less than 1 % of the unpolarized radiation, TM-signals are noisy, which might lead to an imprecise centering due to higher impacts of asymmetric distributions. This is important, because the rotation of

the PBS displaces the intensity's center laterally and vertically; while rotations by 0° and 90° are identical to 180° and 270°, respectively (as verified experimentally). This measurement issue might be solved by using a different type of polarizing beam splitter, which exceeds the possibilities of this thesis. Furthermore, an alternative manual centering method would orient the distributions towards similar or related features shared between the currents or polarizations. Nevertheless, such features couldn't be identified due to the varying inhomogeneous intensity distributions of the polarized near-fields with current. As such, minor differences of the polarization-resolved near- and far-field distributions in lateral positioning might occur, which demands caution when interpreting the presented data. For this reason, plots of the position-resolved degree of TE-polarization, i.e. $I_{TE}(x)/[I_{TE}(x)+I_{TM}(x)]$, which serve as a measure for the local amount of strain, will not be evaluated.

To avoid a necessary manipulation of presented data due to huge intensity differences between the polarization signals or losing the absolute intensity information via normalization, the linear power densities are calculated from the polarization-resolved intensity distributions for an easier comparison of the data:

$$\frac{\Delta P_{lin}(x)}{\Delta x} = \frac{I_{TE/TM}(x)}{\sum_x I_{TE/TM}(x) \cdot \Delta x} \cdot P(J_{TE/TM}) \cdot DOP_{TE/TM}(J_{TE/TM}).$$

Here, $I_{TE/TM}(x)$ denotes the intensity at the lateral position x with index step $\Delta x = 1\,\mu\text{m}$, and $P(J_{TE/TM})$ and $DOP_{TE/TM}(J_{TE/TM})$ the power and degree of TE- or TM-polarization at the operating current $J_{TE/TM}$, respectively. Figure 6.14 portrays the logarithmically scaled TE- and TM-resolved linear power density distributions of the "best" diodes (which are identical to the ones displayed in fig. 6.1; see introduction of chapter 6). TM curves are cut-off in the logarithmic plots, when the noise exceeds the TM-signal such that it becomes negative. Far-field distributions do not *directly* display influences of strain and will therefore be only shown in fig. 6.15, but not discussed.

Near-Fields

The TM-polarized near-fields of the BCA700 diode in fig. 6.14a possess small side lobes around the active zone's edges ($-50\,\mu\text{m}/7.5\,\text{A}/12\,\text{A}$) and outside the active zone ($-75\,\mu\text{m}/7.5\,\text{A}$). Such side lobes occur for ref700's TE- and TM-polarizations near $x = \pm 55\,\mu\text{m}$ at 12 A, too. They are also vaguely perceptible for both designs and polarizations at 2 A. When comparing the left-hand side of BCA700's TM curves with ref700's TM curves, it is apparent that the BCA700 diode exhibits a more asymmetrically distributed, but also reduced TM-signal – e.g. BCA700's TM-signal at 7.5 A reaches $1\,\text{mW}/\mu\text{m}$ only at $15\,\mu\text{m}$ as opposed to ref700 ($\gtrsim 1\,\text{mW}\,\mu\text{m}^{-1}$

(a) 700 nm

(b) 2900 nm
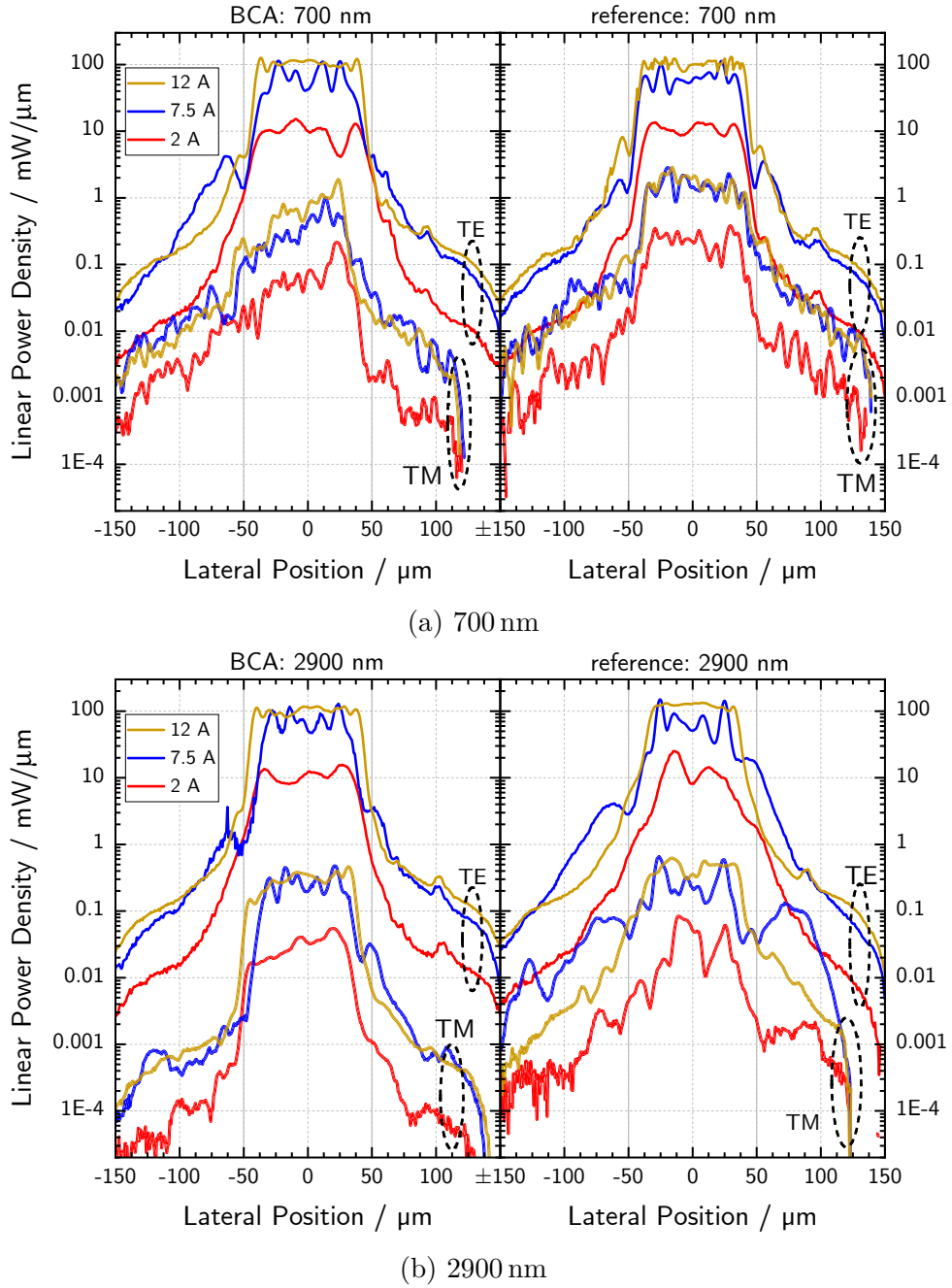
Figure 6.14.: Polarization-resolved linear power densities of the best diodes in logarithmic scale at 2 A (red), 7.5 A (blue) and 12 A (gold). In comparison with their references, BCA designs reduce the amount of TM-radiation, which is further decreased by employing a 2900 nm thick sub-contact layer.

for $|x| \lesssim 40\,\mu m$). However, the TM-polarized side lobes never exceed the TM-signal inside the active zone ($|x| \leq 50\,\mu m$) as observed in [74]. Additionally, some side lobes appear in the same vicinity for TM and TE alike, e.g. at $52\,\mu m/7.5\,A$ and $-53\,\mu m/12\,A$ for BCA700, and at $\pm54\,\mu m/12\,A$ for ref700. Since these side lobes occur at positions $|x| \lesssim 60\,\mu m$, they are still in the range of (positive) gain outside the active zone due to lateral carrier density inhomogeneities as investigated in context of the far-fields in section 6.2.2. Nevertheless, the findings indicate *no* introduction of mechanical stress into the best 700 nm diodes, although the implantation of buried current apertures might be responsible for the observed reduction in the TM-signal of the BCA700 design.

The polarized linear power densities of the best 2900 nm diodes are portrayed in fig. 6.14b. For BCA2900, only one noteworthy side lobe appears at $50\,\mu m/7.5\,A$ for both polarizations. Similar to before, this supports the existence of a lateral carrier density inhomogeneity as predicted by the simulation in fig. 6.9 at 7.5 A and 12 A. In case of the best ref2900 diode, TM as well as TE near-fields are less top-hat shaped (except for 12 A) in comparison with the other diodes, i.e. the intensity contrast between $|x| \leq 50\,\mu m$ and $|x| > 50\,\mu m$ is less pronounced. In particular at 7.5 A around $\pm70\,\mu m$, ref2900 shows the most intense and widest TM side lobe measured in relation to the TM signal inside the AZ. Besides, its TM radiation outside the active zone exceeds that of the BCA variant up to a factor of 100, e.g.at $7.5\,A/-75\,\mu m$. At first glance, this seems to contradict the high measured degree of TE-polarization. Yet, at second glance, ref2900 does also possess higher max. TE-intensities than BCA2900 ($2\,A/13\,\mu m$, $7.5\,A/\pm25\,\mu m$) as well as an about 50 % higher TE ground-level at $7.5\,A/x \leq -50\,\mu m$. In comparison to their references, both BCA diodes reduce the TM-intensity outside the active zone and partially also inside; while a comparison of BCA2900 and BCA700 reveals an overall weaker and less structured TM-signal for the former. Lastly, the the TM radiation decreases by up to more than 50 % from ref700 to ref2900, e.g. from max. $0.4\,mW/\mu m$ to max. $0.06\,mW/\mu m$ at 2 A. As such, a 2900 nm design can indeed significantly mitigate the TM radiation and thereby mounting-induced stress, while an additional buried current aperture multiplies the effect even further. Anyhow, a BCA's impact is rather low without deposition of a thick sub-contact layer.

The polarization-resolved far-fields are displayed in fig. 6.15. But since the *direct* influence of strain can only be seen in the near-fields (indirect influence on far-fields) and to keep the discussion to the point, these distributions will not be evaluated.
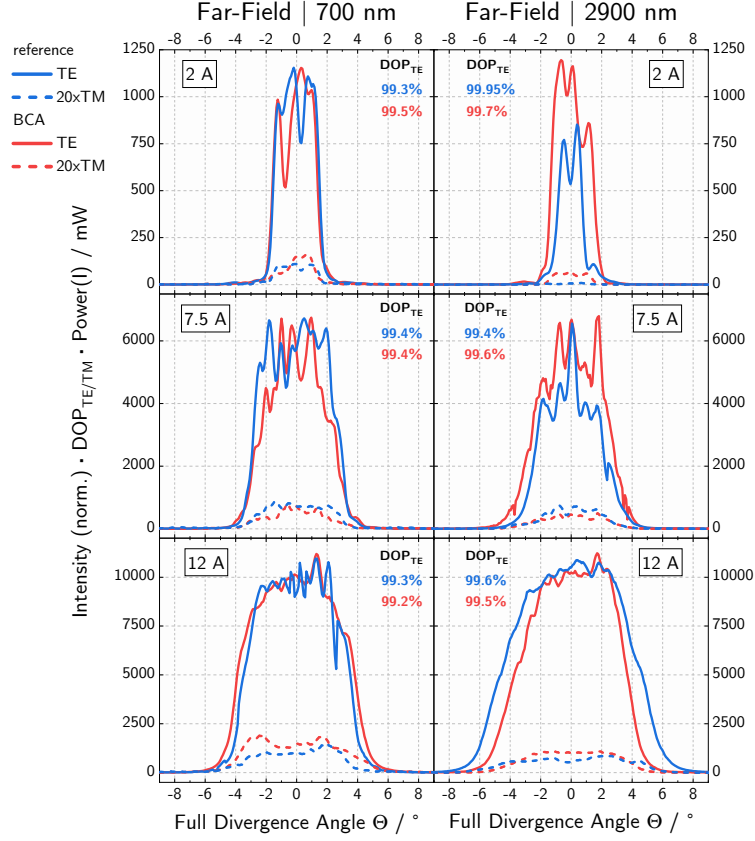
Figure 6.15.: Polarization-resolved (TE: solid; TM: dashed) far-field intensity distributions of the best 700 nm (left) and 2900 nm (right) diodes with (BCA, red) and without (reference, dark blue) buried current apertures. The intensities are scaled with their $DOP_{TE/TM}$ and power at the operating point I. Degrees of TE-polarization DOP_{TE} (SE: $\Delta_\omega = \pm 3\,\%$) are given in every graph. Absolute TM- and TE-intensities are not comparable and therefore TM is further scaled by a factor of 20.

Characteristic 95 % parameters

The characteristic 95 % near-field widths $w_{\mathrm{NF},95\%}$ and full divergence angles $\Theta_{95\%}$ are extracted from three polarization-resolved distributions per design. They are depicted in fig. 6.16 at currents 2 A, 7.5 A and 12 A. TM-polarized symbols are filled grey and their error bars have narrower cap widths than the TE-polarized curves, which are unfilled and colored as in the previous sections. In general, all diagrams are plagued with the large, overlapping error bars of the TM-parameters due to the very low $\mathrm{DOP_{TM}}$. The largest error bars are encountered at 7.5 A for both polarizations of the near-field in fig. 6.16a and the far-field in fig. 6.16b alike. Despite that, both figures share curves, which exhibit extraordinarily low standard deviations. These are all TE-polarized curves (except ref2900 at 7.5 A) and all TM-polarized curves of BCA2900. In fig. 6.16a, all TE near-fields (except ref2900) as well as TM-BCA2900 approximate a common width of 82 µm at max. current and progress comparably to the unpolarized state in fig. 6.4a. Here, the TE- and TM-polarized $w_{\mathrm{NF},95\%}$ curves of BCA2900 (solid blue lines) go along each other. All remaining near-field curves possess only insignificant offsets between their two polarizations.

For the far-fields in fig. 6.16b, a comparable picture as with the near-fields composes. The TE- and TM-polarized $\Theta_{95\%}$ curves run nearly parallel to each other per design, with constant but insignificant offsets due to the high standard deviations of the TM-polarization. Once more, both polarizations of BCA2900 rise parallel from 3° to 8.9°.

Finally, the lateral BPP is plotted over current in fig. 6.16c and over ΔT_{az} in fig. 6.16d. As expected, TM-$\mathrm{BPP_{lat,95\%}}$ are generally about 2-3 times worse than the TE-$\mathrm{BPP_{lat,95\%}}$. Thanks to the very low SD, BCA700's beam quality TE-$\mathrm{BPP_{lat,95\%}} = 2.97(6)$ mm mrad at 12 A dominates slightly over BCA2900 $(3.22(9)$ mm mrad$)$. A look at fig. 6.16d explains the situation: BCA700's active zone heats up less with current, such that it's 2.8 K colder at 12 A than BCA2900's active zone. Consequently, BCA2900 (maybe ref2900, too) is likely to have a better beam quality at the same ΔT_{az}, as is the case at 3.5 K (2 A) and 10 K (7.5 A). This implies a better temperature stability of both 2900 nm designs, while a BCA700 structure provides an improved TE-$\mathrm{BPP_{lat,95\%}}$ with current. Depending on the field of application's demands, one or the other design presents the better choice.

Apart from that, BCA2900 takes on a special role, again. There are neither significant differences between the TE- and TM-components of its $\mathrm{BPP_{lat,95\%}}$; nor between the TE-$\mathrm{BPP_{lat,95\%}}$ of BCA2900 and ref2900. Furthermore, as already stated, ref2900's TM-$\mathrm{BPP_{lat,95\%}}$ is about 2-3 times as bad as the one of BCA2900. By implication, this means that a BCA implantation into diodes with 2900 nm thick

(a) Polarized near-field.

(b) Polarized far-field.

(c) Polarized BPP$_{\text{lat},95\%}$ over I.

(d) Polarized BPP$_{\text{lat},95\%}$ over ΔT_{az}.
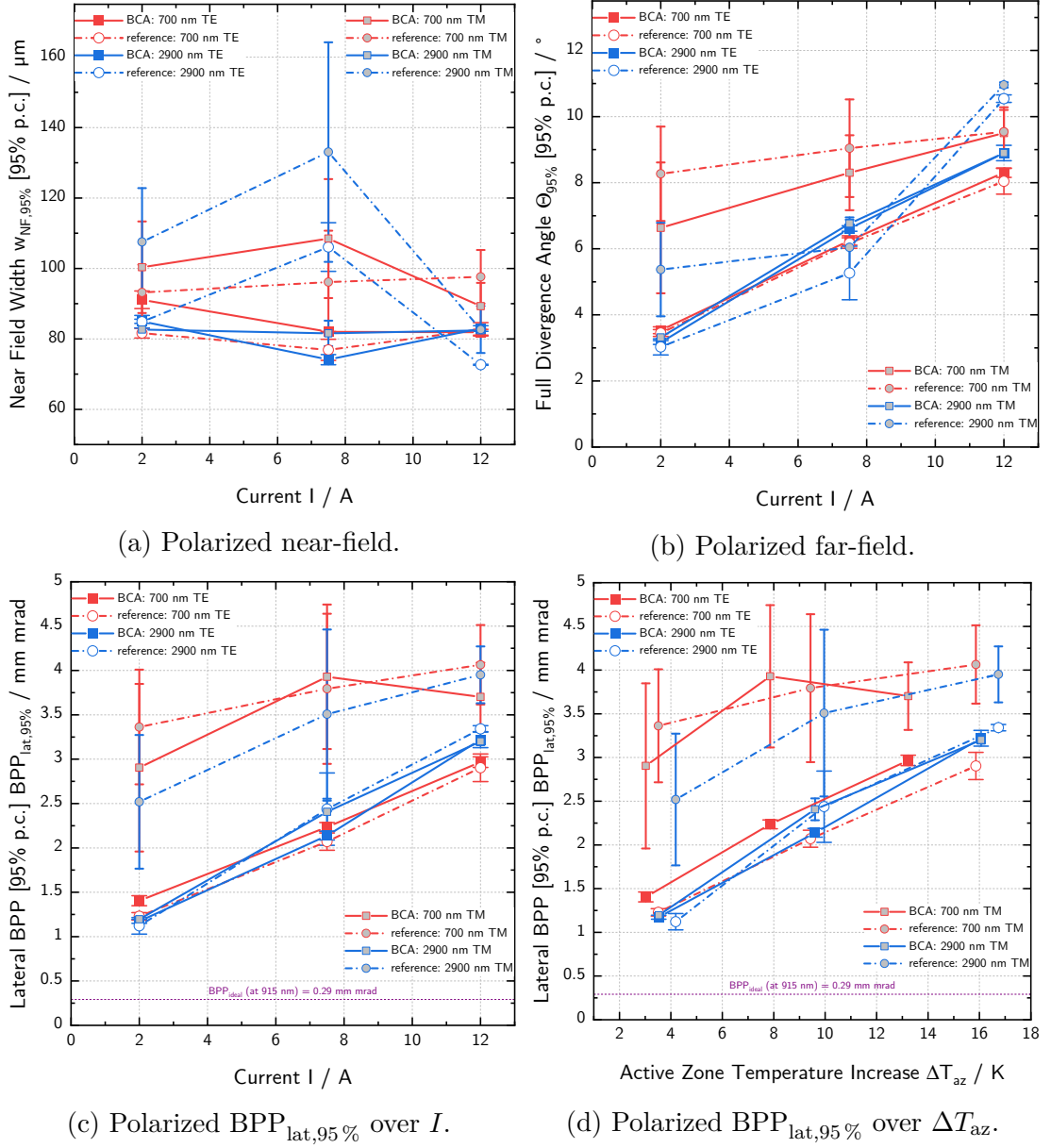
Figure 6.16.: Polarization-resolved 95 % near-field widths (left) and full divergence angles (right) of diodes with (BCA, squares, solid) and without (reference, circles, dashed) buried current aperture at 2 A, 7.5 A and 12 A. TE symbols are colored red (700 nm) or blue (2900 nm) and TM symbols grey. Error bars result from averaging over the specimens and are propagated by Gaussian's law. Thinner error bars with wider caps belong to TE-polarized values.

sub-contact layers significantly reduces the amount of emitted TM-radiation – as has been concluded in the former section from the best, but single diodes. However, regarding two out of three overlapping error bars of the $w_{NF,95\%}$ curve in fig. 6.16a, the formerly observed slight reduction of TM-radiation by the implantation of a BCA into a 700 nm diode must not be big or significant at all.

6.3.3. Section Summary

In section 6.3, the influence of externally stress-induced tensile strain on the polarization of the emitted light has been investigated. It has been found, that the measured DOP_{TE} data are less diversified for 2900 nm and reference structures than for 700 nm and BCA structures, respectively (cf. fig. 6.13). The smaller data diversifications are another indicator for an improved reproducibility of 2900 nm diodes over thinner variants – in particular for ref2900, which possesses a $DOP_{TE}>99.5\%(\pm3\%)$. Apart from that, the DOP_{TE}'s significances allow no further distinction of the designs. For this reason, polarization-resolved near-field distributions have been examined in section 6.3.2. An analysis of the linear power densities of the best diodes has revealed, that the BCA implantation does not cause the emergence of substantial TM-polarized side lobes near the edges. Thus, no hint could be found on *serious* local stress-induced strain (cf. fig. 6.14). Still, a 2900 nm sub-contact layer reduces the overall level of TM radiation of a 700 nm reference diode on average by about 50 %; while the incorporation of a BCA reduces the overall TM level by a further maximal 30 % inside the AZ and up to 100 times as much outside the AZ. In addition, the BCA produces a more homogeneous, top-hat shaped near-field for TE- and TM-polarizations alike. Yet, the lone use of a BCA in a 700 nm structure has a minor or even negligible effect on the total TM intensity. Finally, these findings could be validated through derivation of the characteristic 95 % parameters in section 6.3.2. Important to note is the mitigated temperature sensitivity of the 2900 nm designs. Even though these heat up more with current, they possess better mean TE-BPP$_{lat,95\%}$ up to $\Delta T_{az} = 10\,K$ (7.5 A) than the BCA700 design (cf. fig. 6.16d). In turn, BCA700 provides a slightly better beam quality per current at 12 A.

7. Conclusion

7.1. Summary

In this thesis, the electro-optical properties of gain-guided broad-area single quantum well diode lasers with deeply buried current apertures (BCA) are investigated. The technique bases on a two-step epitaxy process. After the first epitaxy, silicon ions are implanted into the p-doped cladding layers. The implantation defines the BCA and confines the lateral current flow close to the quantum well, reducing current spread. This allows for the deposition of a thick sub-contact layer to reduce mechanical stress. Four designs are studied: BCA diodes with 700 nm (BCA700) and 2900 nm (BCA2900) thick sub-contact layers, as well as related reference designs without BCA (ref700, ref2900). All measurements are compared with electro-optical and thermal simulations.

It has been shown, that the threshold current of BCA2900 diodes reduces significantly by 20 % compared to their references, being on par with both 700 nm designs. This is due to a mitigation of spreading current I_{spr} by 74 % as predicted by the simulation. Although I_{spr} is reduced by half as much (37 %) for BCA700, no similar threshold reduction as with BCA2900 is measured. Additionally, no link between mitigated current spread and series resistance is found. Beyond these observations, the BCA implantation does not *significantly* improve the electro-optical parameters slope, maximum output power and series resistance up to 12 A.

All measured near-fields widen with increasing current and narrow in the range 5-10 A. This is induced by the formation of a thermal waveguide at the design-specific critical current I_{crit}, that is about twice as strong in the longitudinal direction as in the lateral. Except for ref2900, all near-field widths stabilize at $I \geq 10$ A at 82 µm, which is 18 % lower than the targeted near-field width of 100 µm for fiber-coupling. With increasing current, all designs accumulate more carriers at the lateral active zone edges (LCA). These create a carrier-induced refractive index drop, that counteracts the thermal waveguide. At the same time, the LCA provides higher-order TE modes with gain. For the near-fields, this is recognizable as growing side lobes, which leads to the observed stabilization of the near-field widths. It is the main reason for the measured far-field broadening at high currents. The LCA

is much more pronounced for 2900 nm designs than for 700 nm, and barely also for BCA designs than for the references. There is no significant difference in beam quality between the designs, although ref700 *tends* to have the lowest beam quality degradation rate with current and active zone temperature rise.

In general, all measurement values of the beam caustics of 2900 nm and ref700 designs are less diversified than for 700 nm and BCA700, respectively; which holds also true for the experimental active zone temperatures of 2900 nm structures compared with 700 nm. This implies an instability of the 700 nm and BCA diode designs, being prone to, e.g. random variations of manufacturing parameters during the two-step epitaxy. Nevertheless, the diversification can be counteracted quite well by employing a 2900 nm sub-contact layer. This reduces the *overall* level of TM radiation by about 50 %, which is improved even further when incorporating a BCA. No serious influence of *local* stress is identified, although a BCA homogenizes both TE- and TM-polarized near-fields.

Lastly, several measurements haven't made it into the thesis, whose results shall be briefly outlined in the following. First, an elevated heat sink temperature of 50 °C has an insignificant less negative impact on the PUI parameters of BCA designs than on the references. Besides, most parameter values (R_s, w_{NF}, Θ, $\mathrm{BPP_{lat}}$) of 2900 nm structures at the two heat sink temperatures 25 °C and 50 °C lie closer to each other than the 700 nm values. This validates the impression of a higher heat stability of 2900 nm structures. Two exemplary PUI measurements of a mechanically mounted ref700 and a ref2900 diode in QCW mode (2 % duty cycle) lead to a catastrophic optical mirror damage (COMD) of ref700 at 16.5 A, while ref2900 survived even at 20 A, hinting higher COMD limits because of the thicker sub-contact layer. Accelerated lifetime step-stress-tests (1 A up per week) of 700 nm diodes demonstrate that three out of three oxygen-implanted BCA specimens fail up to 15 % (770 h) earlier than a single reference specimen (910 h). These results are confirmed with similar tests of the Si-implanted diodes from this thesis. Here, the best of three BCA700 diodes still degrades 11 % earlier than a single ref700 specimen (1060 h, 10 A), which actually survived the longest of this thesis' diodes; whereas the best BCA2900 diode reaches end-of-life only 2 % earlier than the best ref2900 (1010 h, 9-10 A). Most 700 nm designs degrade before the 2900 nm structures. Cathodoluminescence inspection revealed COMD as reason for all failures.

7.2. Outlook

Deeply buried current apertures harbor great potentials to improve all electro-optical parameters. First, future measurement campaigns need to investigate considerable higher specimen numbers to extinct any random manufacturing influences and overlapping standard deviations. Moreover, the BCA structures tend to lead their trumps at higher currents than 12 A. This affords a mutual increase of measured current ranges and diode stability, since BCA designs tend to degrade sooner in lifetime tests than their references. The coating of the front facet with a non-absorbing mirror has proven beneficial to increase the lifetime of silicon-implanted BCA diodes by up to 16 %.

All 700 nm and 2900 nm diodes present design-specific advantages and drawbacks. The former tend to be marginally superior in terms of heating and beam quality per current, output power and series resistance. Opposed to this are the more efficient performance and beam quality at higher temperatures, lower value diversification, overall reduced level of TM radiation, (possibly) higher COMD limits and longer lifetimes of 2900 nm diodes. All those advantages could potentially be combined with the employment of a medium-thick sub-contact layer. On top of that, growing LCA has shown to be detrimental to the quantum efficiency, the beam quality and development of the field distributions, although counteracting the thermal waveguide. Techniques such as a gradually varying lateral isolation-implantation profile might prove helpful in suppressing lateral carrier accumulation.

There are also major discrepancies between experiment and simulation, whether it's the electro-optical parameters or (in-)homogeneities of the field distributions. These can be tackled by studying the experimental current spread, comparing the results with the carrier density simulations. Two possibilities are described in [57, pp. 77–80]: first, the examination of the near-field distribution during amplified spontaneous emission right below the threshold; second, the measurement of the spontaneous emission above threshold with an optical fiber at a lateral angle of 45° to the front facet for the avoidance of stimulated emission. Beyond that, is has to be made sure that all relevant physical processes are simulated like thermal waveguiding due to large spreading currents. Additional design variants with varying resonator lengths would allow for the experimental determination of internal parameters for matching to the simulated ones.

A. Appendix

A.1. Derivation of the Carrier Transport and Drift Model

The mobile electron n and hole p densities in the conduction or valence bands as well as their fixed counterparts n_A in the acceptor or p_D in the donor levels build the electric field which in terms of electrostatic potential ϕ assembles to the Poisson equation:

$$-\nabla \cdot (\epsilon \nabla \phi) = e\left(p + p_D - n - n_A\right), \tag{A.1}$$

with $\epsilon = \epsilon_r \epsilon_0$ being the absolute permittivity. Local charge neutrality must be valid in every layer:

$$p + p_D = n + n_A, \tag{A.2}$$

with $n = n_0 + N$ and $p = p_0 + N$ being the sum of the equilibrium densities n_0, p_0 and an excess carrier density N in the active region (current sheet density divided by quantum well thickness). The flow of particles is expressed in continuity equations for the electron $\vec{j}_n$ and hole $\vec{j}_p$ current densities:

$$\nabla \cdot \vec{j}_n = +e\left(R + \partial_t n\right) \tag{A.3}$$

$$\nabla \cdot \vec{j}_p = -e\left(R + \partial_t p\right). \tag{A.4}$$

Using the electron and hole conductivities $\sigma_n = e\mu_n n$, $\sigma_p = e\mu_p p$, with their mobilities μ_n, μ_p, and the quasi-Fermi potentials φ_n, φ_p the current densities (for parabolic bands as for most semiconductors) compose to:

99

$$\vec{j}_n = +\sigma_n \nabla \varphi_n \qquad (A.5)$$

$$\vec{j}_p = -\sigma_p \nabla \varphi_p \qquad (A.6)$$

The electron and hole carrier densities n and p are connected to the effective densities of states (DOS) N_c and N_v for the conduction E_c and valence band edge energies E_v, respectively, as well as to the exponents of the Fermi function $f(E)$

$$\frac{n}{N_c} = F_{\frac{1}{2}} \left(\frac{e\phi - e\varphi_n - E_c}{k_B T} \right) \qquad (A.7)$$

$$\frac{p}{N_v} = F_{\frac{1}{2}} \left(\frac{-e\phi + e\varphi_p + E_v}{k_B T} \right) \qquad (A.8)$$

where $F_{\frac{1}{2}}(x)$ denotes the Fermi-Dirac integral of order $1/2$ which computes the equilibrium carrier concentration per unit volume in Fermi-Dirac statistics, as explained in this paper by Kim et al. [77]. Then, equations (A.5) and (A.6) can be split into terms for carrier drift and diffusion:

$$\vec{j}_n = n\mu_n \nabla (E_c - e\phi) + e D_n \nabla n \qquad (A.9)$$

$$\vec{j}_p = p\mu_p \nabla (E_v - e\phi) - e D_p \nabla p \qquad (A.10)$$

where

$$D_n = \mu_n \frac{k_B T}{e} \frac{n}{N_c} F_{\frac{1}{2}}^{-1\,\prime} \left(\frac{n}{N_c} \right) \qquad (A.11)$$

$$D_p = \mu_p \frac{k_B T}{e} \frac{p}{N_v} F_{\frac{1}{2}}^{-1\,\prime} \left(\frac{p}{N_v} \right) \qquad (A.12)$$

are the diffusion coefficients for electrons and holes utilizing the derivative of the inverse Fermi integral $F_{\frac{1}{2}}^{-1\,\prime}$. Because of its flatness $\nabla \varphi_n \approx 0$ when neglecting the small lateral voltage drop due to current spread of the n-layers compared to the p-layers [46], a constant electron quasi-Fermi potential can be assumed which is set to zero $\varphi_n \approx const = 0$. This means that the electron current $\vec{j}_n$ consists only of its vertical component $j_{n,y}$ which does not vary in vertical direction. Consequently,

the total current density $j(N)$ injected into the active region is controlled by the varying hole current flow $\vec{j}_p$ which will be derived in the following.

Under the assumption of negligible photoionization of impurities, thermal gradients and other effects [46], it is valid to assume only lateral carrier diffusion and drift in the thin quantum well (active zone), so the current's vertical portions can be averaged over. Paying attention to the approximations made ($\partial_z N \approx 0$, $\varphi_n \approx 0$), inserting D_n in eq. (A.9) leads to

$$\partial_x \left[\frac{E_c}{e} - \phi \right] = -\partial_x \left[\frac{k_B T}{e} F_{\frac{1}{2}}^{-1} \left(\frac{n}{N_c} \right) \right] \tag{A.13}$$

which transforms to the lateral hole current density $\vec{j}_{p_x}$ when considering the parallelism of the band edges ($\nabla E_c = \nabla E_v$) and inserting it into eq. (A.10):

$$\vec{j}_{p_x} = -\frac{k_B T}{e} \sigma_p \partial_x \left[F_{\frac{1}{2}}^{-1} \left(\frac{n}{N_c} \right) + F_{\frac{1}{2}}^{-1} \left(\frac{p}{N_v} \right) \right]. \tag{A.14}$$

Notice the vanishment of the Fermi-Dirac integral's derivation. The expression obtained can be simplified by evaluating $F_{\frac{1}{2}}^{-1}$ and introducing $D_{\text{eff}}(N) = \frac{\sigma_p}{e} \partial_N U_F(N)$, with the hole conductivity $\sigma_p = e\mu_p (p_0 + N)$ and Fermi voltage $U_F(N) = \varphi_p(N) - \varphi_n(N)$:

$$\vec{j}_{p_x} = \sigma_p \partial_x U_F \tag{A.15}$$
$$= -e D_{\text{eff}} \partial_x N. \tag{A.16}$$

Inserting this excess carrier density N-dependent formulation of the lateral hole current density $\vec{j}_{p_x}$ (the spreading current density) into its corresponding continuity equation eq. (A.4) produces

$$\partial_t N(r,t) = \partial_x \left[D_{\text{eff}} \partial_x N \right] - \frac{\partial_y j_{p_y}}{e} - R(N, \|E\|^2), \tag{A.17}$$

which is eq. (4.13) in section 4.2.

Bibliography

[1] Grand View Research. *Laser Cutting Machine Market Analysis By Technology (Solid State, Gas, Semiconductor), By Process (Fusion, Flame, Sublimation), By Application (Consumer Electronics Defense and Aerospace), and Segment Forecasts, 2018 - 2024.* Feb. 2017. URL: https://www.grandviewresearch.com/industry-analysis/laser-cutting-machine-market (visited on 05/20/2020).

[2] Gail Overton et al. *Annual Laser Market Review & Forecast 2019: What goes up...* Jan. 1, 2019. URL: https://www.laserfocusworld.com/articles/print/volume-55/issue-01/features/what-goes-up.html.

[3] P. Crump et al. „Efficient High-Power Laser Diodes". In: *IEEE Journal of Selected Topics in Quantum Electronics* 19.4 (July 2013), pp. 1501211–1501211. ISSN: 1558-4542. DOI: 10.1109/JSTQE.2013.2239961.

[4] Phillip Sprangle et al. *Beam Combining: High-power fiber-laser beams are combined incoherently.* July 21, 2008. URL: https://www.laserfocusworld.com/lasers-sources/article/16563778/beam-combining-highpower-fiberlaser-beams-are-combined-incoherently (visited on 05/20/2020).

[5] R. Paschotta. „Fiber Lasers Versus Bulk Lasers". In: *Encyclopedia of Laser Physics and Technology.* URL: https://www.rp-photonics.com/fiber_lasers_versus_bulk_lasers.html (visited on 05/20/2020).

[6] Thomas Schreiber, Andreas Tünnermann, and Andreas Thoss. *Fiber Lasers: High-power, single-mode fiber lasers advance.* Laser Focus World, June 11, 2017. URL: https://www.laserfocusworld.com/lasers-sources/article/16548197/fiber-lasers-highpower-singlemode-fiber-lasers-advance (visited on 05/20/2020).

[7] *Fiber lasers: The state of the art.* Apr. 1, 2012. URL: https://www.laserfocusworld.com/test-measurement/spectroscopy/article/16549567/fiber-lasers-fiber-lasers-the-state-of-the-art (visited on 05/20/2020).

[8] Sonja Unger et al. „Optical properties of ytterbium/aluminium doped silica glasses". In: *Opt. Mater. Express* 10.4 (Apr. 2020), pp. 907–925. DOI: 10.1364/OME.388350. URL: http://www.osapublishing.org/ome/abstract.cfm?URI=ome-10-4-907.

[9] Gulshad Nawaz Ahmad et al. „Experimental investigation on Ytterbium fiber laser butt welding of Inconel 625 and Duplex stainless steel 2205 thin sheets". In: *Optics & Laser Technology* 126 (2020), p. 106117.

[10] Y. Jeong et al. „Ytterbium-doped large-core fiber laser with 1.36 kW continuous-wave output power". In: *Opt. Express* 12.25 (Dec. 2004), pp. 6088–6092. DOI: 10.1364/OPEX.12.006088. URL: http://www.opticsexpress.org/abstract.cfm?URI=oe-12-25-6088.

[11] R. Paschotta. „Infrared Light". In: *Encyclopedia of Laser Physics and Technology*. URL: https://www.rp-photonics.com/infrared_light.html (visited on 05/20/2020).

[12] Rüdiger Paschotta et al. „Ytterbium-Doped Fiber Amplifiers". In: 33.7 (1997), pp. 1049–1056. ISSN: 00189197. DOI: 10.1109/3.594865.

[13] M. Hemenway et al. „Wavelength stabilized fiber-coupled diode laser modules for DPSS and fiber laser pumping". In: *High-Power Diode Laser Technology XVIII*. Ed. by Mark S. Zediker. Vol. 11262. International Society for Optics and Photonics. SPIE, 2020, pp. 101–109. DOI: 10.1117/12.2547539. URL: https://doi.org/10.1117/12.2547539.

[14] Sajib Chowdhury et al. „500 W Ytterbium Doped Monolithic Fiber Laser at 1 μm using Non-Wavelength Stabilized Laser Diodes". In: *2019 Workshop on Recent Advances in Photonics (WRAP)*. IEEE. 2019, pp. 1–3.

[15] Chris McIntosh et al. „High average power passively Q-switched Yb:YAG micro-laser". In: *Solid State Lasers XXIX: Technology and Devices*. Ed. by W. Andrew Clarkson and Ramesh K. Shori. Vol. 11259. International Society for Optics and Photonics. SPIE, 2020, pp. 138–144. DOI: 10.1117/12.2546693. URL: https://doi.org/10.1117/12.2546693.

[16] Matthew Peters et al. „High-power, high-efficiency laser diodes at JDSU". In: *High-Power Diode Laser Technology and Applications V* 6456 (2007), 64560G. DOI: 10.1117/12.701072.

[17] Anissa Zeghuzi et al. „Modeling of current spreading in high-power broad-area lasers and its impact on the lateral far field divergence". In: *Physics and Simulation of Optoelectronic Devices XXVI* 10526.February (2018), p. 52. ISSN: 1996756X. DOI: 10.1117/12.2289803. URL: https://www.spiedigitallibrary.org/conference-proceedings-of-spie/10526/2289803/Modeling-of-current-spreading-in-high-power-broad-area-lasers/10.1117/12.2289803.full.

[18] T. Kaul et al. „Suppressed power saturation due to optimized optical confinement in 9xx nm high-power diode lasers that use extreme double asymmetric vertical designs". In: *Semiconductor Science and Technology* 33.3 (2018). ISSN: 13616641. DOI: 10.1088/1361-6641/aaa221.

[19] Dominik Martin et al. „Current spreading suppression by O- and Si-implantation in high power broad area diode lasers". In: March (2019), p. 19. DOI: 10.1117/12.2509762.

[20] H. Wenzel et al. „Influence of current spreading on the transparency current density of quantum-well lasers". In: *Semiconductor Science and Technology* 15.6 (2000), pp. 557–560. ISSN: 02681242. DOI: 10.1088/0268-1242/15/6/312.

[21] P. Della Casa et al. „High-power broad-area buried-mesa lasers". In: *Semiconductor Science and Technology* 32.6 (2017), p. 65009. ISSN: 13616641. DOI: 10.1088/1361-6641/aa6e9b. URL: http://dx.doi.org/10.1088/1361-6641/aa6e9b.

[22] P. Della Casa et al. „High power broad-area lasers with buried implantation for current confinement". In: *Semiconductor Science and Technology* 34.10 (2019), p. 105005. ISSN: 13616641. DOI: 10.1088/1361-6641/ab39b8.

[23] Rudolf Gross and Achim Marx. *Festkörperphysik*. München: Oldenbourg Wissenschaftsverlag, 2012. ISBN: 9783486712940.

[24] Roland Diehl. *High-Power Diode Lasers*. Ed. by Roland Diehl. Vol. 78. Topics in Applied Physics. Berlin, Heidelberg: Springer Berlin Heidelberg, 2000. 416 pp. ISBN: 978-3-540-66693-6. DOI: 10.1007/3-540-47852-3. URL: http://link.springer.com/10.1007/3-540-47852-3.

[25] Peter W. Epperlein. *Semiconductor Laser Engineering, Reliability and Diagnostics*. 2013. ISBN: 9781119990338. DOI: 10.1002/9781118481882.

[26] Larry A. Coldren, Scott W. Corzine, and Milan L. Masanovic. *Diode Lasers and Photonic Integrated Circuits*. Vol. 3. September. 2012. ISBN: 9780470484128.

[27] Bahaa E. A. Saleh and Malvin Carl Teich. *Grundlagen der Photonik*. 2. Aufl. New York: John Wiley & Sons, 2008. ISBN: 978-3-527-40677-7.

[28] Marc Eichhorn. *Laser Physics - From Principles to Practical Work in the Lab*. Berlin Heidelberg: Springer Science & Business Media, 2014. ISBN: 978-3-319-05128-4.

[29] D. Sands. *Diode Lasers*. 1st ed. Boca Raton: CRC Press, 2004. ISBN: 978-1-420-05699-0. DOI: https://doi.org/10.1201/9781420056990.

[30]   K. H. Hasler et al. „Comparative theoretical and experimental studies of two designs of high-power diode lasers". In: *Semiconductor Science and Technology* 29.4 (2014), p. 045010. ISSN: 0268-1242. DOI: `10.1088/0268-1242/29/4/045010`.

[31]   Yuji Yamagata et al. „915nm high-power broad area laser diodes with ultra-small optical confinement based on Asymmetric Decoupled Confinement Heterostructure (ADCH)". In: vol. 9348. 2015, 9348 – 93480F –10. DOI: `10.1117/12.2078698`. URL: `https://doi.org/10.1117/12.2078698`.

[32]   B. S. Ryvkin and E. A. Avrutin. „Asymmetric, nonbroadened large optical cavity waveguide structures for high-power long-wavelength semiconductor lasers". In: *Journal of Applied Physics* 97.12 (2005). ISSN: 00218979. DOI: `10.1063/1.1928309`.

[33]   N. A. Pikhtin et al. „Internal optical loss in semiconductor lasers". In: *Semiconductors* 38.3 (2004). ISSN: 1063-7826. DOI: `10.1134/1.1682615`.

[34]   Kenneth A. Jackson, ed. *Materials Science and Technology - Processing of semiconductors*. In collab. with R. W. Cahn, P. Haasen, and E. J. Kramer. Vol. 16. Weinheim: Wiley-VCH, 1996. ISBN: 978-3-527-26813-9.

[35]   S.J. Pearton. „Ion implantation for isolation of III-V semiconductors". In: *Materials Science Reports* 4.6 (1990), pp. 313–363. ISSN: 0920-2307. DOI: `https://doi.org/10.1016/S0920-2307(05)80001-5`. URL: `http://www.sciencedirect.com/science/article/pii/S0920230705800015`.

[36]   *GaAs - Thermal properties*. URL: `http://www.ioffe.ru/SVA/NSM/Semicond/GaAs/thermal.html` (visited on 05/20/2020).

[37]   Xiaodong Du et al. „Lateral current spreading in stripe laser diodes". In: *2010 OSA-IEEE-COS Advances in Optoelectronics and Micro/Nano-Optics, AOM 2010* 3 (2010), pp. 1–4. DOI: `10.1109/AOM.2010.5713517`.

[38]   W. T. Tsang. „The effects of lateral current spreading, carrier out-diffusion, and optical mode losses on the threshold current density of GaAs-Al χGa1-χAs stripe-geometry DH lasers". In: *Journal of Applied Physics* 49.3 (1978), pp. 1031–1044. ISSN: 00218979. DOI: `10.1063/1.325040`.

[39]   Anissa Zeghuzi et al. „Time-Dependent Simulation of Thermal Lensing in High-Power Broad-Area Semiconductor Lasers". In: *IEEE Journal of Selected Topics in Quantum Electronics* 25.6 (2019), pp. 1–10. ISSN: 1077-260X. DOI: `10.1109/jstqe.2019.2925926`.

[40]   Anissa Zeghuzi et al. „Traveling Wave Analysis of Non-Thermal Far-Field Blooming in High-Power Broad-Area Lasers". In: *IEEE Journal of Quantum Electronics* 55.2 (2019). ISSN: 00189197. DOI: `10.1109/JQE.2019.2893352`.

[41] Hans Wenzel and Anissa Zeghuzi. „High-Power Lasers". In: *Handbook of Optoelectronic Device Modeling and Simulation. Lasers, Modulators, Photodetectors, Solar Cells, and Numerical Methods*. Ed. by Joachim Piprek. 1st ed. Vol. 2. Boca Raton: CRC Press, 2017, pp. 15–58. DOI: `10.4324/9781315152318`.

[42] Mindaugas Radziunas. *BALaser - A software tool for simulation of dynamics in Broad Area semiconductor Lasers*. URL: `https://www.wias-berlin.de/software/index.jsp?id=BALaser&lang=1#publications` (visited on 05/20/2020).

[43] Mindaugas Radziunas. „Simulations and analysis of beam shaping in spatially modulated broad area edge-emitting devices". In: *Conference Digest - IEEE International Semiconductor Laser Conference* 9134 (2014), pp. 19–20. ISSN: 08999406. DOI: `10.1109/ISLC.2014.142`.

[44] Hans Wenzel, Götz Erbert, and Peter M. Enders. „Improved Theory of the Refractive-Index Change in Quantum-Well Lasers". In: 5.3 (1999), pp. 637–642.

[45] H. Wenzel et al. „Theoretical and experimental investigations of the limits to the maximum output power of laser diodes". In: *New Journal of Physics* 12 (2010). ISSN: 13672630. DOI: `10.1088/1367-2630/12/8/085007`.

[46] W. B. Joyce. „Carrier transport in double-heterostructure active layers". In: *Journal of Applied Physics* 53.11 (1982), pp. 7235–7239. ISSN: 00218979. DOI: `10.1063/1.331621`.

[47] Jan Pomplun et al. „Thermo-optical simulation of high-power diode lasers". In: *Physics and Simulation of Optoelectronic Devices XX*. Ed. by Bernd Witzigmann et al. Vol. 8255. International Society for Optics and Photonics. SPIE, 2012, pp. 218–224. DOI: `10.1117/12.909330`. URL: `https://doi.org/10.1117/12.909330`.

[48] Toshihiko Makino. „Analytical formulas for the optical gain of quantum wells". In: *IEEE Journal of Quantum Electronics* 32.3 (1996), pp. 493–501. ISSN: 00189197. DOI: `10.1109/3.485401`.

[49] W. Shockley. „The Theory of p-n Junctions in Semiconductors and p-n Junction Transistors". In: *Bell System Technical Journal* (1949). ISSN: 15387305. DOI: `10.1002/j.1538-7305.1949.tb03645.x`.

[50] C. D. Lien, F. C.T. So, and M. A. Nicolet. „An Improved Forward I-V Method For Nonideal Schottky Diodes With High Series Resistance". In: *IEEE Transactions on Electron Devices* 31.10 (1984), pp. 1502–1503. ISSN: 15579646. DOI: `10.1109/T-ED.1984.21739`.

[51] D. P. Bour and A. Rosen. „Optimum cavity length for high conversion efficiency quantum well diode lasers". In: *Journal of Applied Physics* 66.7 (1989), pp. 2813–2818. ISSN: 00218979. DOI: 10.1063/1.344209.

[52] *Optical-grade Spectralon®Reflectance Material*. Labsphere Inc. 2019. URL: https://www.labsphere.com/labsphere-products-solutions/materials-coatings-2/coatings-materials/spectralon/ (visited on 05/20/2020).

[53] Y.P. Varshni. „Temperature dependence of the energy gap in semiconductors". In: *Physica* 34.1 (1967), pp. 149–154. ISSN: 0031-8914. DOI: https://doi.org/10.1016/0031-8914(67)90062-6. URL: http://www.sciencedirect.com/science/article/pii/0031891467900626.

[54] Sajal Paul, J. B. Roy, and P. K. Basu. „Empirical expressions for the alloy composition and temperature dependence of the band gap and intrinsic carrier density in $Ga_xIn_{1-x}As$". In: *Journal of Applied Physics* 69.2 (1991), pp. 827–829. DOI: 10.1063/1.348919. eprint: https://doi.org/10.1063/1.348919. URL: https://doi.org/10.1063/1.348919.

[55] *InGaAs - Temperature Dependences*. URL: http://www.ioffe.ru/SVA/NSM/Semicond/GaInAs/bandstr.html#Dependence%20Temperature (visited on 05/20/2020).

[56] R. Paschotta. „ABCD Matrix". In: *Encyclopedia of Laser Physics and Technology*. URL: https://www.rp-photonics.com/abcd_matrix.html (visited on 05/20/2020).

[57] Martin Winterfeldt. „Investigation of slow-axis beam quality degradation in high-power broad area diode lasers". Dissertation. Technische Universität Berlin, 2017.

[58] ENISO DIN. „11146-1 DIN EN ISO 11146-1: 2005-04: Laser und Laseranlagen-Prüfverfahren für Laserstrahlabmessungen, Divergenzwinkel und Beugungsmaßzahlen-Teil 1: Stigmatische und einfach astigmatische Strahlen". In: *Berlin: Beuth* (2005).

[59] M. Winterfeldt et al. „Experimental investigation of factors limiting slow axis beam quality in 9xx nm high power broad area diode lasers". In: *Journal of Applied Physics* 116.6 (2014), p. 063103. DOI: 10.1063/1.4892567. eprint: https://doi.org/10.1063/1.4892567. URL: https://doi.org/10.1063/1.4892567.

[60] Joint Committee for Guides in Metrology. *Evaluation of measurement data – Guide to the Expression of Uncertainty in Measurement (GUM)*. Sept. 2008. URL: https://www.bipm.org/en/publications/guides/gum.html.

[61] S. Rauch et al. „Impact of longitudinal refractive index change on the near-field width of high-power broad-area diode lasers". In: *Applied Physics Letters* 110.26 (2017). ISSN: 00036951. DOI: 10.1063/1.4990531.

[62] Peter M. Smowton and Peter Blood. „The differential efficiency of quantum-well lasers". In: *IEEE Journal on Selected Topics in Quantum Electronics* 3.2 (1997), pp. 491–498. ISSN: 1077260X. DOI: 10.1109/2944.605699.

[63] Henry Aldridge et al. „N-type Doping Strategies for InGaAs". In: *Materials Science in Semiconductor Processing* 62 (2017). Advanced doping methods in semiconductor devices and nanostructures, pp. 171–179. ISSN: 1369-8001. DOI: https://doi.org/10.1016/j.mssp.2016.12.017. URL: http://www.sciencedirect.com/science/article/pii/S1369800116306357.

[64] P. Crump et al. „Experimental and theoretical analysis of the dominant lateral waveguiding mechanism in 975 nm high power broad area diode lasers". In: *Semiconductor Science and Technology* 27.4 (2012), p. 045001. ISSN: 0268-1242. DOI: 10.1088/0268-1242/27/4/045001.

[65] Ortwin Hess, Stephan W. Koch, and Jerome V. Moloney. „Filamentation and Beam Propagation in Broad-Area Semiconductor Lasers". In: *IEEE Journal of Quantum Electronics* 31.1 (1995), pp. 35–43. ISSN: 15581713. DOI: 10.1109/3.341705.

[66] Joachim Piprek and Z. M. Simon Li. „On the importance of non-thermal far-field blooming in broad-area high-power laser diodes". In: *Applied Physics Letters* 102.22 (2013), pp. 4–7. ISSN: 00036951. DOI: 10.1063/1.4809835.

[67] M. Winterfeldt et al. „High Beam Quality in Broad Area Lasers via Suppression of Lateral Carrier Accumulation". In: *IEEE Photonics Technology Letters* 27.17 (Sept. 2015), pp. 1809–1812. ISSN: 1041-1135. DOI: 10.1109/LPT.2015.2443186.

[68] OriginLab Corporation. *Fitting with Errors and Weighting.* URL: https://www.originlab.com/doc/Origin-Help/FIt-with-Err-Weight (visited on 05/20/2020).

[69] OriginLab Corporation. *Why parameter's standard error remains the same when error bar largely changes?* URL: https://www.originlab.com/doc/Quick-Help/Chi-Se-Remain (visited on 05/20/2020).

[70] OriginLab Corporation. *Why is my Reduced Chi-Sqr value very different from 1?* URL: https://www.originlab.com/doc/Quick-Help/Bad-ReducedChiSqr (visited on 05/20/2020).

[71] OriginLab Corporation. *Theory of Nonlinear Curve Fitting.* URL: https://www.originlab.com/doc/Origin-Help/NLFit-Theory#Reduced_Chi-Sqr (visited on 05/20/2020).

[72] OriginLab Corporation. *Algorithms (Fit Linear with X Error)*. URL: https://www.originlab.com/doc/Origin-Help/Ref-Linear-XErr (visited on 05/20/2020).

[73] Derek York et al. „Unified equations for the slope, intercept, and standard errors of the best straight line“. In: *American Journal of Physics* 72.3 (2004), pp. 367–375. DOI: 10.1119/1.1632486. eprint: https://doi.org/10.1119/1.1632486. URL: https://doi.org/10.1119/1.1632486.

[74] Rintaro Morohashi et al. „High polarization purity operation of 99% in 9xx-nm broad stripe laser diodes“. In: *High-Power Diode Laser Technology XVI*. Ed. by Mark S. Zediker. Vol. 10514. International Society for Optics and Photonics. SPIE, 2018, pp. 53–58. DOI: 10.1117/12.2288157. URL: https://doi.org/10.1117/12.2288157.

[75] Moshe Levy, Yuri Berk, and Yoram Karni. „Effect of compressive and tensile strain on the performance of 808 nm QW High Power Laser diodes“. In: 61040 (2006). DOI: 10.1117/12.645815.

[76] Daniel T. Cassidy. „Rotation of principal axes and birefringence in III-V lasers owing to bonding strain“. In: *Appl. Opt.* 52.25 (Sept. 2013), pp. 6258–6265. DOI: 10.1364/AO.52.006258. URL: http://ao.osa.org/abstract.cfm?URI=ao-52-25-6258.

[77] Raseong Kim, Xufeng Wang, and Mark Lundstrom. *Notes on Fermi-Dirac Integrals*. 2008. arXiv: 0811.0116 [cond-mat.mes-hall].

List of Figures

List of Tables